UNIVERSITÀ DEGLI STUDI DELLA TUSCIA DI VITERBO

DIPARTIMENTO DI PER L'INNOVAZIONE NEI SITEMI BIOLOGICI, AGROALIMENTARI E FORESTALI

Corso di Dottorato di Ricerca in

SCIENZE AMBIENTALI - XXVIII Ciclo

STRUCTURAL ANALYSIS OF ENDOGENOUS BIOACTIVE PEPTIDES

(s.s.d CHIM/02)

Tesi di dottorato di:

Dott. Cristina Olivieri

Coordinatore del corso

Prof. Maurizio Petruccioli

Tutore

Prof. Fernando Porcelli

Co-tutore

Prof. Gianluigi Veglia

22 Giugno 2016

Hope lies in dreams,

in imagination and in the courage

of those who dare to make

dreams into reality

Jonas Salk

Acknowledgments

I would like to acknowledge many people for helping me to achieve this accomplishment, but first and foremost I want to especially thank both my advisors, Prof. Fernando Porcelli and Gianluigi Veglia, for their guidance as well as for their scientific enthusiasm and creativity. Their willingness to pursue new and difficult challenges has been a source of inspiration and motivation during my graduate career. I am thankful for their continuous support and for challenging me to grow and improve not only as a scientist, but as a person as well.

I want to extend a thank you to Dr. Francesco Buonocore and Prof. Giuseppe Scapigliati for the collaboration in Chionodracine projects

I also want to thank Dr. Maria Giordani who has always been a source of inspiration and sincere and trusted friend.

I would like to thank all the members of Veglia Lab, past and present, for their support and friendship through the period that I have spent there as a visiting PhD student. I want to thank, Dr. Manu V. Surahmanian, Geoffrey Li, Alysha A. Dicke, Sarah E.D. Nelson, Adak N. Karamafrooz, Erik K. Larsen and Caitlin Walker. I am honored to have had the opportunity to work with such great scientists. I would like to especially thank Dr. Jonggul Kim for the quality discussions that we had, for being an exceptional role model and friend.

Lastly I want to thank my family and friends for their love and support during this “journey”, especially my father, for supporting me in every single moment. He taught me to believe in myself and to not be afraid to dream. I love you dad.

To my family
that has always been by my side
in the good and bad times.

Contents

List of tables

List of figures

Chapter 1

Preface

1.1 Unconventional Protein

For over fifty years, Anfinsen's Principle has remained the driving force for understanding the relationship between protein structure and function [9, 10]. According to this principle, the primary sequence of the protein, derived from the translation information encoded in the mRNA, determines a singular unique structure for the protein. This unique fold is what governs the function of the protein. While there can be no doubt that protein structure and function are linked, numerous studies have demonstrated that almost 30% of the eukaryotic genome encodes for protein sequences that do not fold into a stable globular structure [11-13]. These proteins were initially classified as unconventional proteins and later as intrinsically disordered proteins (IDPs). These IDPs are biologically active in physiological conditions with no well-defined 3D structure[14, 15]. Intrinsic disorder in proteins is structurally very diverse. These can range from small disordered linkers to molten globule structure to complete absence of structure.

However what is the purpose for intrinsic disorder for function? Genomic analyses have found that IDPs are frequently involved in regulation, recognition, and signaling; where high-specificity and low affinity interactions with

multiple partners are fundamental prerequisites for function. Specificity is commonly achieved by recognition of a linear amino acid motif on the IDP or a general environmental change. Upon binding, often a subsequent disorder-to-order transition (coupled binding and folding) occurs, typically that of a α-helix, while others remain disordered [16-18]. The increasing interest in these proteins is due to their prominent roles in many pathophysiological cellular mechanisms. As a result, there has been a growing awareness that proteins with intrinsically disordered regions (IDR) or fully-disordered (IDPs) are biologically active and play important roles in both eukaryotic and prokaryotic cells [15, 19].

There are small endogenous peptides that interact with biological membranes and share many characteristics with other IDPs, but are not fully recognized as IDPs in the literature. These peptides, better known as membrane-active peptides, are unstructured in solution, but undergo a disorder-to-order transition upon interaction with phospholipid membranes [20]. However, these membrane-active peptides are not involved in signaling and transcriptional regulation. Membrane-active peptides can be divided in three groups: *i*, the amyloid peptides that are characterized by their ability to form stable-β-sheet-rich structures known as amyloid fibers present in Alzheimer disease [21]; *ii*, the cell-penetrating peptides that show the intrinsic capacity to translocate across biological membranes [22]; and *iii*, the antimicrobial peptides (AMPs), that belong to the ancient component of the eukaryotic innate immune system directed against the bacterial infections[23]. In the last twenty years, the research on the characterization of the structure and the biological function of these peptides

has shown their importance in biology and human health. In this work, I will argue that these classifications are arbitrary as membrane-associated peptides and IDPs fundamentally share the same mechanism, where disorder imparts function and activity is exhibited by the environment in which the protein is present in.

Chapter 2

Scope of the work

In my PhD work I have focused on elucidating the structure, mechanism and function of several peptides which are characteristic of IDPs. In the following PhD thesis I elucidated the antimicrobial activity of *Chionodracine* (CND), an antimicrobial peptide, isolated in the immune system of the gills of the Antarctic teleost *Chionodraco hamatus* [24]. I used steady-state fluorescence spectroscopy to characterize the membrane disrupting properties of the peptide in interaction with synthetic and natural membrane environments. Nuclear magnetic resonance (NMR) spectroscopy was used to solve the 3D structure in presence of dodecyl-phosphocholine (DPC) micelles. I demonstrated that CND can bind to membranes of different lipid compositions with a preference for membranes mimicking those of prokaryotic cells. CND also interacts with *Escherichia coli* BL21 (DE3) and *Psychrobacter sp.* TAD1 membranes and cause the lysis of the bacterial cells. Studies of fluorescence quenching demonstrated that, upon the binding, this peptide remains adsorbed at the lipid surface, only partially exposed to the aqueous environment. This behavior is also confirmed by the NMR structure where, the peptide assumes a classical amphipathic α-helix, with the hydrophobic residues on one side on the helix, and the hydrophilic on the other side [8].

Due to the interest of discovering of new AMPs with higher activity to be used as an antibiotic-substitute, I introduced rational mutations in CND to increase its antimicrobial activity. I reasoned from the NMR structure that CND with a stronger hydrophobic/hydrophilic interface would increase antimicrobial activity. I designed three different mutants, with increased net positive charge and hydrophobicity, and characterized their interaction with synthetic and natural membranes. As with wild-type CND, the characterization of the mutant's function, in the presence of different phospholipid membranes, was assessed using steady-state fluorescence spectroscopy experiments. These studies demonstrated that the mutations have increased antimicrobial properties of CND. The mutants showed a stronger ability to interact, bind and disrupt membranes of different lipid compositions that can be directly correlated to the number of positively charged amino acids present in the sequence. All of my work on CND, was carried out in collaboration with Professor Francesco Buonocore, Ph.D, from University of Tuscia (Department for Innovation in Biological, Agro-food and Forest systems, University of Tuscia, Viterbo, Italy) and Professor Gianluigi Veglia, Ph.D, from the University of Minnesota (Biochemistry, Molecular Biology and Biophysics and Chemistry Department, University of Minnesota – Twin Cities, Minneapolis, MN, United States of America).

In the second part of my PhD work I focused on the elucidation of the mechanism of inhibition of the catalytic subunit of cAMP-dependent protein kinase A (PKA-C), by the endogenous Protein Kinase Inhibitor peptide (PKI) [25]. PKI is a fully disordered 75 amino acid protein that regulates the activity

and the intracellular localization of PKA-C [26, 27]. To understand the molecular mechanism underlying recognition of PKA-C by PKI, I characterized the change in the conformational landscape that PKI undergoes upon binding to PKA-C (Apo to PKA-C bound). These studies were carried out using NMR spectroscopy, the only structural technique to provide atomic resolution detail on IDPs. Using chemical shift analysis and nuclear spin relaxation experiments, I demonstrated that PKI alone has minimal secondary structural elements with only two transient helixes. However, paramagnetic relaxation enhancement (PRE) experiments [28] show that PKI is not fully disordered, but has transient tertiary intramolecular interaction between the C- and N-terminus. When PKI is bound to the kinase, in the presence of the non-hydrolysable ATP mimic, β,γ-Imidoadenosine 5′-triphosphate (ATPγN), only the sequence that directly interacts with the catalytic subunit undergoes significant structural rearrangement while the majority of the peptide is still unfolded. By clarifying the mechanisms of inhibition and regulation of PKA-C, we will be able to provide new insights into enzymatic regulation at the cellular level.

Chapter 3

Introduction

3.1. Antimicrobial peptide

Due to the indiscriminate use of antibiotics, from agricultural and human health, the last thirty years we have observed an increase in the resistance of conventional antibiotics [23]. Antimicrobial peptides (AMPs) have emerged as a potential class of agents that may replace antibiotics, due to the inability of pathogenic organisms to develop resistance. The AMPs are a fundamental and ancestral component of the innate immune system of eukaryotic organisms against bacteria, protozoa, fungi, and virus infections. Although they have been identified in a wide range of tissues, they are prevalent in epithelial tissue where they represent a “first line of defense” against pathogen infections [23, 29-31].

AMPs have been described in prokaryotic cells since 1939, when substances isolated from *Bacillus brevis*, named gramicidin, showed antimicrobial activity both *in vivo* and *in vitro* against a wide range of Gram-positive bacteria [32, 33]. Nevertheless systematic studies on this class of membrane interacting peptides started only at the beginning of the 1980’s, when the primary structure of cepropin (AMP from insect) was published by Hans Boman and co-workers [34-36]. Since then, hundreds of AMPs have been characterized and, even though they show a widely diverse amino acid sequences, they share some pe-

culiar features. Typically, natural AMPs are composed of 12-60 amino acid residues, predominantly of positively charged and hydrophobic residues. Due to their considerable genetic variability, AMPs cannot be easily classified on the base of size or physico-chemical parameters. However they can be categorized on the base of their secondary structure in: β-sheet, α-helix, extended, and loop peptides [37]. Among this structural groups, α-helix and β-sheet are the more common [31, 38] and α-helical peptides are the most studied AMPs. The best known examples of α-helical AMPs are protegrin, magainin, cyclic indolicin and coiled inolicin [39]. Usually, in α-helical structures, the distance between two adjacent amino acid residues is around 0.15 nm and the angle between them with regard to the center id around 100 degree from the top view. β-sheet peptides are composed of at least two β-strands with disulfide-bonds between the strands [31]. However, most AMPs do not assume a defined secondary structure and they cannot be classified in this categories. Also, many α-helical peptides assume an active structure only when they interact with the membranes of target organism. For example, indolicin assume a globular and amphipathic conformation in aqueous solution, while it is wedge-shaped in presence of phospholipid bilayers [40]. Instead the majority of β-sheet peptides do not undergo to drastically conformational transition, but preserve their secondary structure even in absence of phospholipid membranes [37]. AMPs can also be classified according to their (*i*) biosynthetic pathways, (*ii*) mechanism of biological activity, and (*iii*) structural properties. AMPs can be *ribosomally-synthetized*, (this is typical-

ly of higher eukaryotes) or *non ribosomally-synthetized* (when produced by lower eukaryotes and prokaryotic organisms) [41]. On the base of their biological activity, AMPs are classified in antiviral, antifungal, anticancer, antiparasital, insecticidal, spermicidal, anti-HIV, and/ or with chemotactic nature [42, 43].

The most important features of all AMPs are their ability to selectively interact with microbial biological membranes and kill the pathogen. AMP's ability to distinguish between target and host cells depends largely on the differential membrane composition between the prokaryotic and eukaryotic membranes (**Figure 3.1**) [37, 44]. All biological membranes are a fluid mosaic composed of proteins and phospholipids [45]. By definition, the phospholipid bilayer is amphipathic with a hydrophobic surface and hydrophilic interior. Each organism has an asymmetric composition of the phospholipids in the bilayer. Eukaryotic membranes are rich in zwitterionic neutral phospholipids, like phosphatidylcholine (PC), phosphatidylethanolamine (PE), and sphingomyelin (SM) (**Figure 3.2**) [44]. Prokaryotic membranes are composed predominantly of negative charged phospholipids; phosphatidylglycerol (PG), cardiolipin (CL, that is a dimer of PG), and phosphatidylserine (PS).

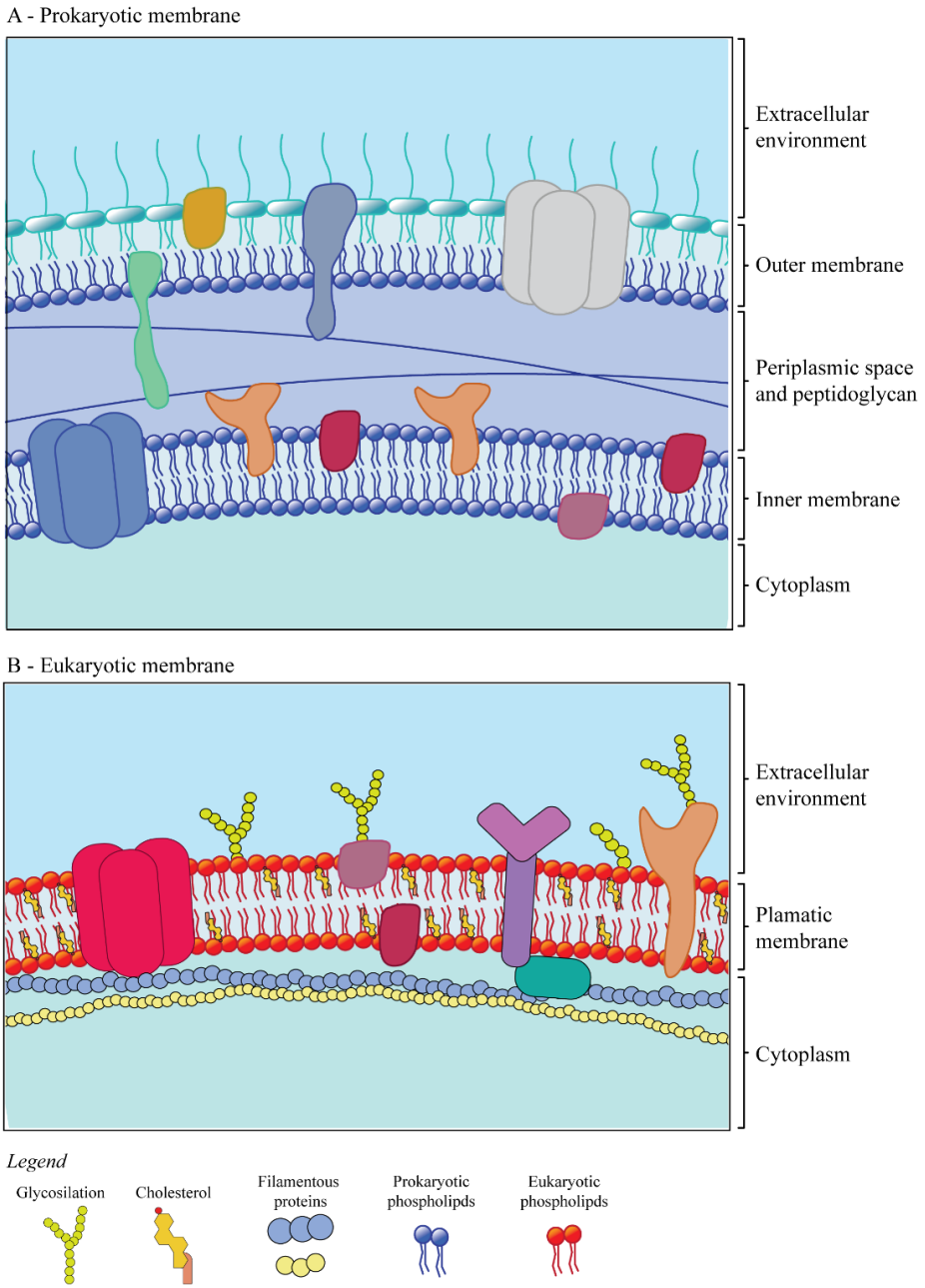

Figure 3.1. Schematic representation of biological membrane. (A) Gram-negative membrane schematization. The Gram-negative bacteria have two different membrane (outer and inner membrane) that differ on phospholipid and protein composition. The outer membrane contain the lipopolysaccharides (LPS) that contribute to the structural integrity of the membrane. (B) Model of eukaryotic membrane, composed by neutral phospholipids.

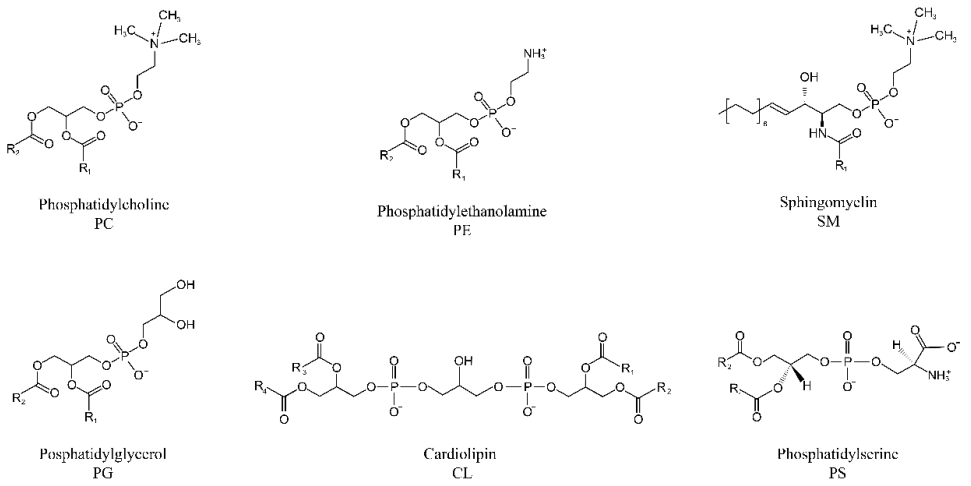

Figure 3.2.Principal phospholipids present in biological membrane.
In the top are reported the phospholipids typically compose the eukaryotic membrane, while in the bottom structure are phospholipid present almost exclusively in prokaryotic organism. The letter R indicate the different fatty acid chains that can be coordinate to the glycerophosphoric acid group.

From this prospective, it follows that the prokaryotic membranes are generally more electronegative than eukaryotic membranes, and the membrane itself can work as a pseudo-receptor for AMP recruitment [23, 46, 47]. Therefore, the interaction of the cationic AMPs with target cells does not require macromolecular recognition, but is largely due to the electrostatics [48, 49].

Many AMPs exhibit their killer-activity against the pathogens through the interaction and disruption of phospholipid membrane integrity [37, 50]. In this case, no matter the mechanism used to perturb the target membrane, all the proposed models start with an electrostatic interaction between the AMPs and the charged phospholipids of the membrane (*attraction* step) [50]. Upon the peptide/lipid interaction (*attachment* step) [51-54], the peptide undergoes a structural rearrangement (*folding-upon-binding* mechanism) that allows the insertion into the lipid bilayer (*insertion* step) [55-58]. These peptides induce structural

changes in the prokaryotic membrane through formation of pores (pore formation model) or solubilization of the membrane (carpet-like model) [2]. In both cases, the disruption of the membrane integrity causes the dissipation of the electrochemical gradients, necessary for cell survival, and the leakage of cytoplasmic metabolites. The most popular pore forming models are the *barrel-stave, toroidal,* and the *carpet-like* model (**Figure 3.2**), in which the AMPs oligomerize and form pores in the membrane [2, 43]. In the *barrel-stave* model, the pore is formed by peptides that aggregate to form a bundle of monomers aligned parallel to the membrane [59, 60]. In the *toroidal* model, binding of AMP on the membrane induces a curvature strain on the leaflets on the bilayer until the two sides of the bilayer fuse to form a peptide/lipid lined pore [59, 61, 62]. In the *carpet-like* model, AMPs accumulate on the surface of the membrane and, once an effective concentration threshold is reached, a micellization of the membrane is induced. This model is often called also a detergent-like model, for the similarity with the detergent mechanism of action [59, 62-64].

Parallel to the structural models, two thermodynamic models have been developed in the last two years to describe the mechanism of action [51, 52]. Both models, *graded* or *all-or-none* model, are based on the analysis of AMP capability to induce leakage of a fluorescence dye entrapped inside a phospholipid vesicle [51, 52, 65-67]. If the addition of AMP to the vesicle suspension induces the disruption of all the vesicles, highlighted by a massive release of fluorescence dye, the peptide acts according to the *grade model* [51, 52, 65, 68]. If on-

ly a fraction of the vesicles release the content and the other part do not lose any dye, the peptide perform a dye release according to *all-or-none* [69, 70].

The structural and binding characterization of AMPs in presence in native lipid environments is fundamental to understand underlying mechanism of their antimicrobial activity. Nuclear magnetic resonance spectroscopy (NMR) and X-ray crystallography are the most important techniques for the determination of atomic resolution structure of biomolecules [2, 43]. Unfortunately, it is nearly impossible to obtain high quality crystals of AMPs in a lipid environment, due to their small size and intrinsic flexibility. Fortunately NMR has been fruitful in determining high resolution atomic structures of AMPs in membrane-like environments [2, 43, 71]. This has primarily been achieved using solution-NMR techniques using micelles as membrane-like environments [72, 73]. However, solid state NMR spectroscopy, in particular using oriented solid state NMR (OSS-NMR) techniques, has emerged as a powerful tool to determine the structure of AMPs [74, 75]. Not only does OSS-NMR allow for atomic resolution structure determination in full native lipid environments, but also allows for the determination of the topology of AMPs along the membrane.

For the characterization of the binding and kinetic mechanism of AMP/membrane interaction, fluorescence spectroscopy is largely used. This sensitive spectroscopy allows the calculation of kinetic and thermodynamics parameters that describe the interaction of AMPs with natural or synthetic phospholipid bilayer [51, 52, 67, 68, 76, 77].

3.2. Intrinsically disordered protein

The classical Anfinsen's principle has stated the structure-function relationship in proteins for decades [9]. This paradigm of states that the primary sequence is defines the structure of the protein, and the fold determines its function. In the past 20 years, numerous studies have demonstrated that a large portion of the proteome is formed by proteins that are partial or fully unstructured in solution, nevertheless are functional [14, 18, 78-90]. Over the 30% of the human proteome is predicted to be composed by proteins that exhibit intrinsic disorder, including folded proteins with intrinsically disordered regions (IDRs) and entirely structure-less entities [83, 91]. From this prospective, it follows that "structured proteins" classify the proteins that do not possess IDRs, while proteins that are fully unstructured are called intrinsically disordered proteins (IDPs).

The ability of a protein to fold or not under physiological conditions is encoded in its amino acid sequence [14, 18, 81]. A bioinformatic study conducted over 275 natively folded and 91 natively unfolded proteins has demonstrated that is the combination between a low mean hydrophobicity and a high net charge the essential pre-requisite for the absence of a compact structure in proteins [81]. IDRs and IDPs lack in a bulky hydrophobic core that driving the folding events of globular proteins, but they are rich in charged a polar amino acids.

IDRs and IDPs are involved in numerous cell processes and, based on their mode of action, are grouped in six functional classes: (*i*) assemblers, (*ii*) chaperons, (*iii*) display site, (*iv*) effectors, (*v*) entropic chain, and (*vi*) scavengers [15, 92]. Eukaryotes and viruses use IDRs/IDPs essentially for mediating transient protein-protein interactions in signaling and regulation processes. Conversely, prokaryotes use disordered proteins mainly for larger lasting interaction involved in formation of complex between two or more partners [93]. IDPs were almost never involve in (a) catalysis, (b) biosynthesis, (c) metabolism, (d) transport processes [11, 16].

Currently, the important role that IDRs/IDPs play in the cell is globally recognized and, in light of this, new theories have been developed [3]. For example, proteins have been proposed to function within a conformational *continuum*, ranging from complete disordered to a fully structured [86] (**Figure 3.3**). In this model, that does not contemplate the presence of boundaries between the described states and the native proteins, IDRs/IDPs fluctuate stochastically between several different states (transiently sampling coil-like states, localized secondary structure, and more globular states). What determines the structural characteristic and the population of the individual states in the conformational ensemble is the nature of the amino acid sequence and their distribution. Hence, in the native unbound state, IDRs/IDPs exist as a dynamic ensemble of rapidly interconverting conformations [94-96].

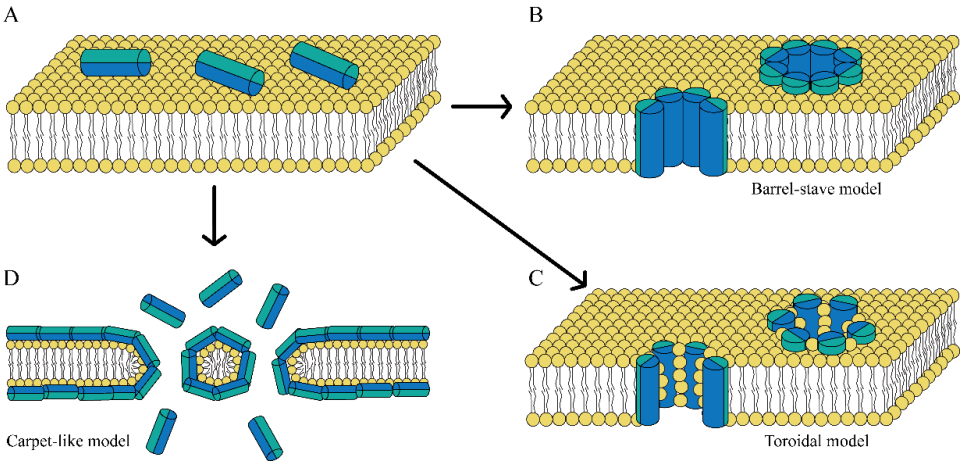

Figure 3.3. Proposed model for antimicrobial activity of AMP. The antimicrobial peptides pile up on the bilayer surface (A) until they reach a threshold concentration. Following an aggregation process, they disrupt the bilayer integrity through; a barrel-stave model (b), toroidal model (c), and carpet-like model (figure adapted from [1, 2]).

It was proposed the mechanism of IDR/IDP-mediating molecular interaction works using a combination of *conformational selection* and *induced folding*. These two models are not mutually exclusive. The dominant mechanism depends on the concentrations of the individual proteins (*conformational selection*) [97] and on the association rate constant (*induced folding*) [98]. Briefly, in the *conformational selection model*, the addition of binding partners can result in a shift of the population in the conformational ensemble of the IDP that is most favorable for the binding [99-104]. This mechanism was observed in protein-protein and protein-nucleic acids interaction [101]. On the other hand, the *induced folding model* asserts that the IDP undergoes a disorder-to-order transition upon association with the binding partner [100, 105-107]. Usually, disordered segments assume a well-defined 3D-structure upon the interaction with

the binding target. The IDPs retain a significant conformational freedom even when they are bound to the target [108].

To study the structure of partial or fully disordered proteins, a variety of experimental techniques are used including NMR, small-angle X-ray scattering (SAXS), and single-molecule fluorescence. SAXS is the elastic scattering of X-rays by biomolecules at small angles, reporting on the size and shape [109, 110]. Although straightforward with simple experimental conditions, SAXS is inherently a low resolution technique. Single-molecule (sm) techniques, like sm-fluorescence resonance energy transfer (smFRET), are able to minimize averaging over the heterogeneous ensembles of conformations in which IDPs naturally exit. smFRET can measure the dynamics and individual conformations of the unbound ensemble, intermediates during induce folding, and internal friction in the folding process of IDPs [111-113] in a time resolved manner. However, the spatial resolution is limited by the placement of the FRET probes. NMR has emerged as a powerful technique to study the conformational ensemble of IDPs since this is the only technique that can provide atomic resolution structural insights of IDPs [95, 114-116]. Application of NMR to the study of IDPs has shown the existence of transient secondary and tertiary structural elements that are invisible to other techniques and quantifies protein dynamics in IDPs along a wide range of timescales (ps to seconds). Correlating structural dynamics of IDPs to functional consequences remains an on-going challenge in understanding IDP function and mechanism (Appendix).

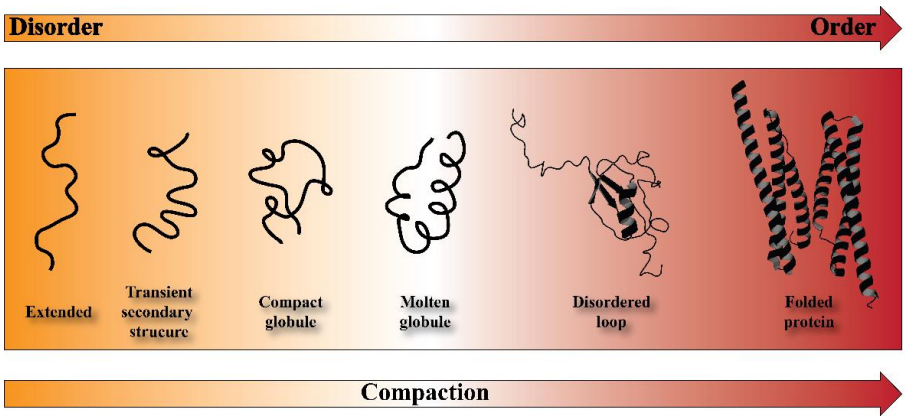

Figure 3.4 Schematic representation of the continuum model for protein structure. The protein are ranging from highly dynamic conformation (organ) to a well-defined folded proteins. SUMO-1 (PDB 2N1A) and dystrophin (PDB 3UMM) are chosen as a prototypes for disordered-loop and well-folded proteins, respectively. (Figure adapted from [3]).

3.3 Protein kinases

The phosphorylation of target proteins is one of the most common signaling pathway used by the cells to regulate fundamental intra-cellular processes like cellular cycle, metabolism and apoptosis [1]. Since 1955, when the importance of protein phosphorylation was first elucidate as a regulatory cell mechanism [2], numerous studies have demonstrated the crucial role that this protein modification plays in regulation processes of mammalian cells [3, 4]. The enzymes that perform and regulate phosphorylation inside the cells are the protein kinases. This enzymatic family is composed by over 500 members and accounts for approximately 2% of the entire mammalian genome (kinome – **Figure 3.5**) [5, 6], and 4% of the plant genome [7]. The canonical function of these enzymes is to transfer the γ-phosphate of adenosine triphosphate (ATP) to Ser/Thr/Tyr residues of the target substrates [2], causing the activation or deactivation of different signaling pathways [8-11]. Inside the cell, protein kinases play a crucial role as a molecular switches, and thus they are highly dynamics protein that can exist between several different conformational states [12]. Most of these enzymes are also phosphoproteins, and those phosphates are essential for both structure and protein function [3]. For instance, phosphorylation sites can be used as docking sites for other proteins or as an organizing points for a specific structure conformation [3]. The majority of protein kinases take part to signaling events through a dual-function: they not only catalyze the phosphoryl transfer but they can act as scaffolds to modulate, integrate, or compete in the signaling

cascade [3, 13]. Over a decade ago, a new classes of kinases with a non-canonical function was described by Manning and coworkers [14].

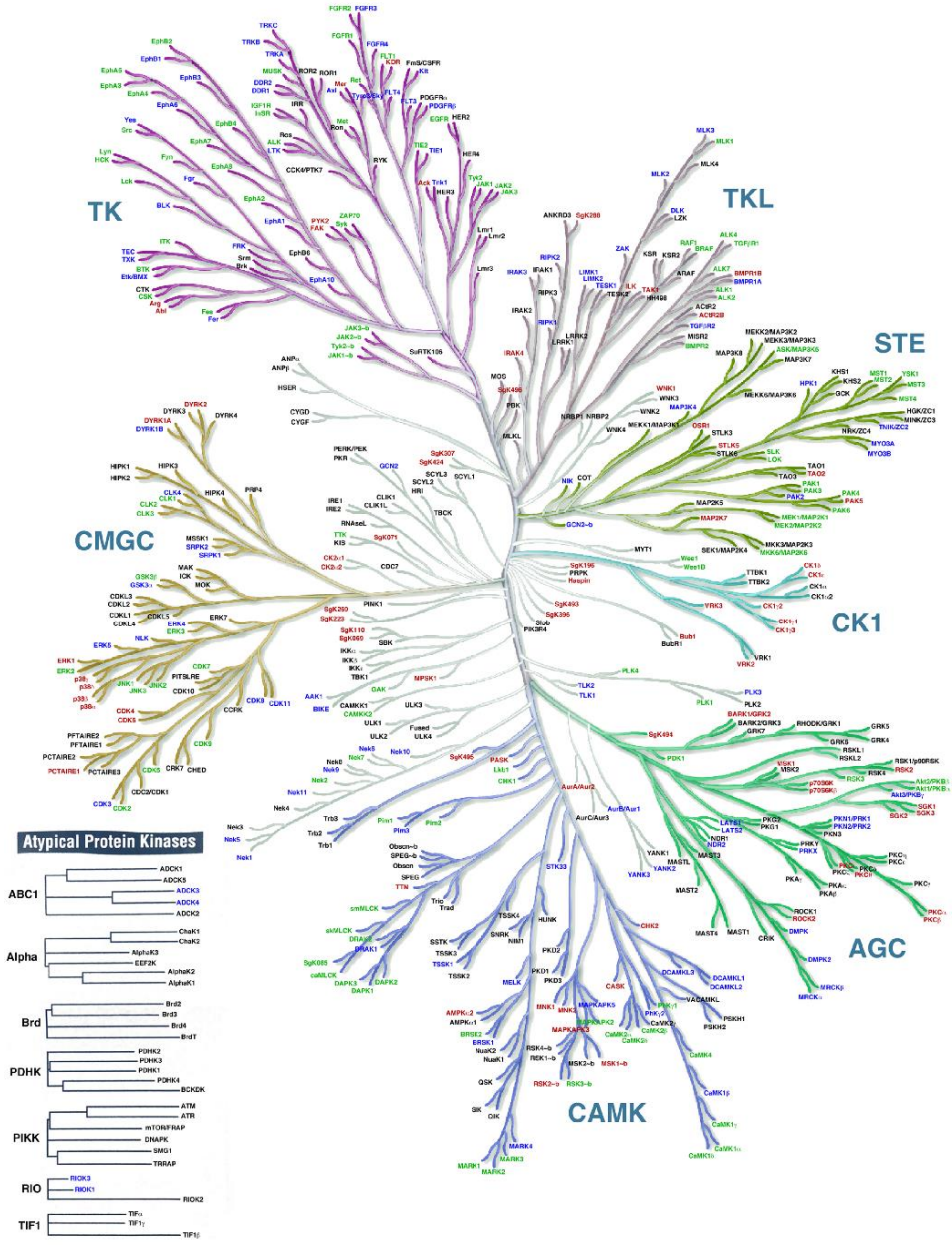

Figure 3.5 Human kinome. Classification of all the protein kinases present in the human genome (adapted from Manning et. al. [4]).

They discover that approximately 10% of kinome contained mutations in canonical amino acid motifs thought to be fundamental for the catalytic function.

These proteins, called pseudo-kinases, are partial or completely devoid of catalytic activity [15, 16], but they may have a more general essential non-catalytic role in signaling pathways, [16-18]. Conversely, a dead kinase is a protein that cannot neither perform the catalytic activity nor act as a scaffold for binding substrates and inhibitors [19]. Due to the crucial processes in which kinases take part, their activity is also finely tuned by cofactors and/or accessory proteins that coordinate the protein activation or deactivation over time and space [20]. Typically, protein kinase are thought to be maintained in a basal, inactive state and recruited to action transiently by extracellular stimuli [21].

3.3.1 cAMP-dependent protein kinase A

Within the large and diversified kinase families that compose the kinome [14, 22], cAMP-dependent protein kinase A (cAPK), known also as protein kinase A (PKA), is considered the prototype of the entire super-family [23-25]. Inside the cell, PKA exist as an inactive heterotetramer formed by two catalytic subunits (PKA-C) bound to a dimer of regularity (R) subunits (**Figure 3.6**). The cooperative binding of the cellular second messenger cyclic adenosine monophosphate (cAMP) to R subunits causes the disassembling of holoenzyme and the releasing of the active PKA-C [26]. PKA-C targets a diverse array of substrates, including protein localized in the cytoplasm, mitochondria, plasma membrane, sarcoplasmic reticulum membrane and nucleus [27], and it is involve in numerous cellular signaling cascades induce by β-adrenergic stimulations (**Figure 3.7**).

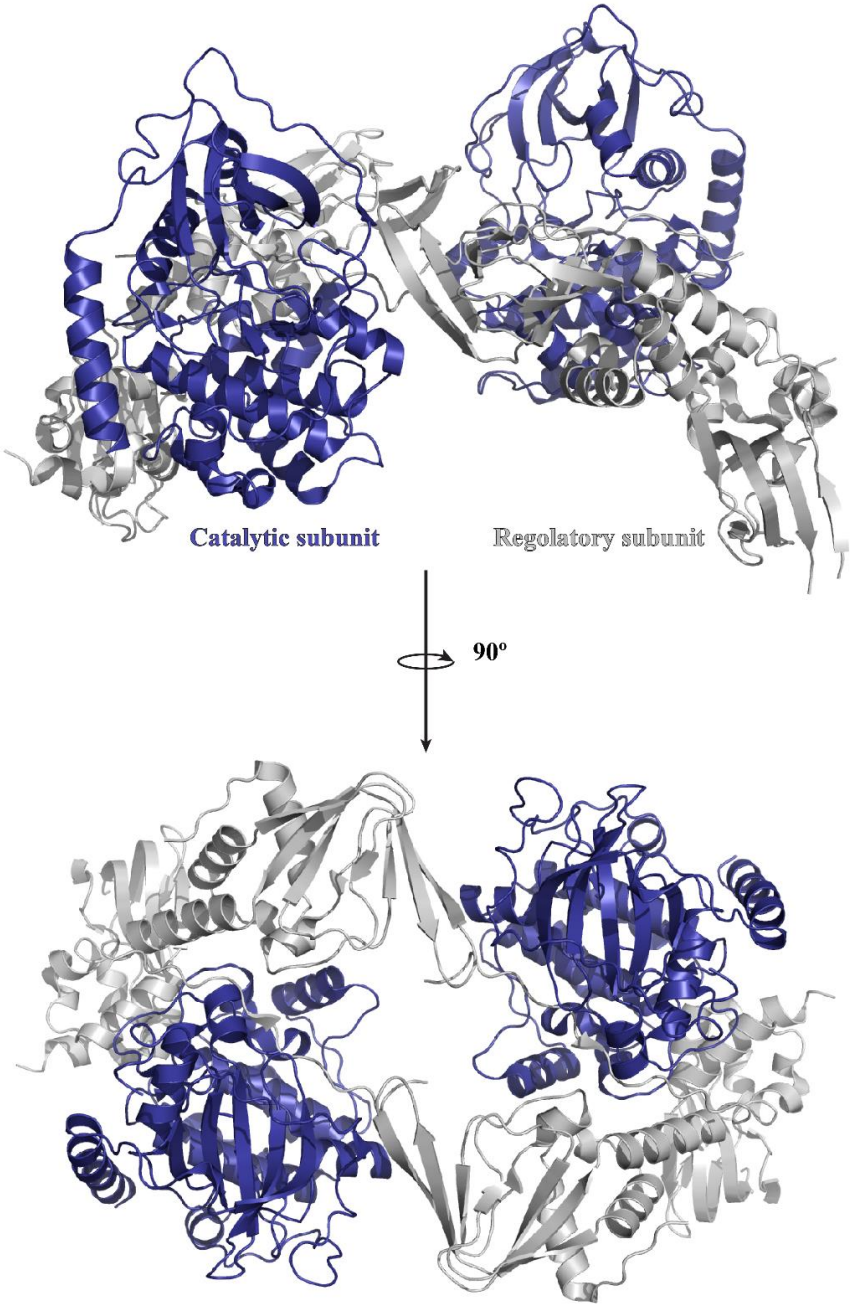

Figure 3.6 3D structure of cAMP-dependent protein kinase A. X-ray structure of protein kinase A holoenzyme formed by two catalytic subunits and the dimer of RIIβ regulatory subunits (PDB-3TNP, [5]).

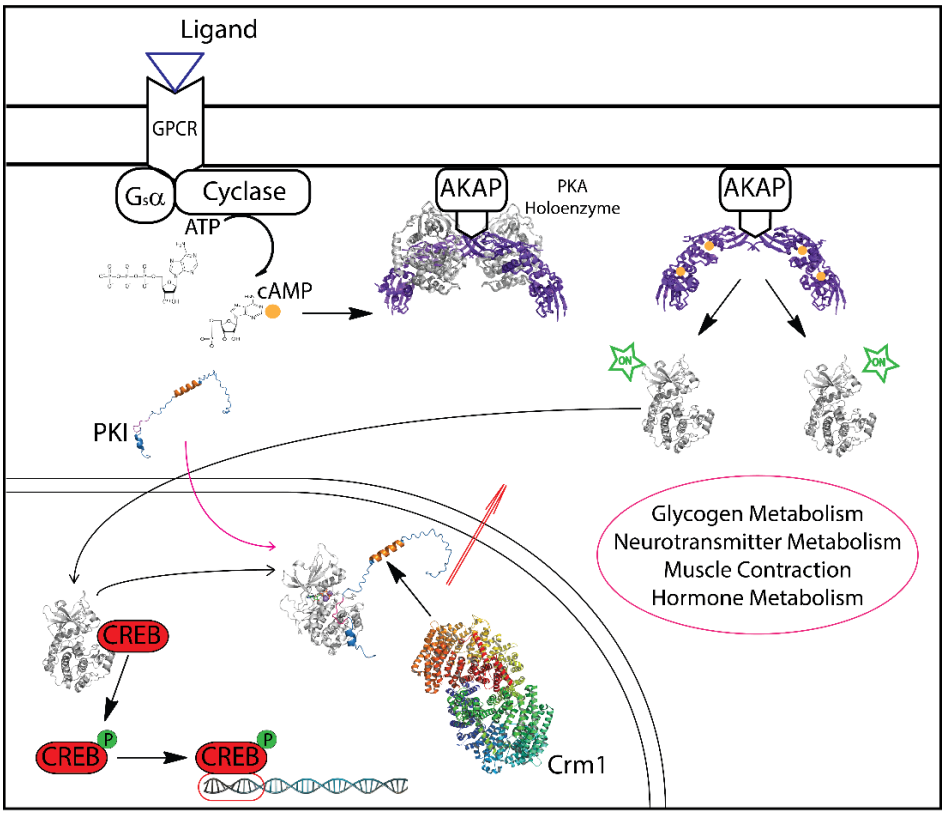

Figure 3.7 Intracellular signaling pathway of transcription factor activation. Signaling cascade for the activation of the cAMP-responsive element-binding protein (CREB). The binding of a ligand (in the specific case glucagon) to the G protein-coupled receptor (GPCR), causes the translocation of the α-subunit of the coupled G protein to the membrane-bound adenylyl cyclase, with the concomitant transformation of GTP from GDP. cAMP is produced and, through the binding to the regulatory subunit of the cAMP-dependent protein kinase A (PKA) (PDB-3TNP) holoenzyme, induces the release of the catalytic subunits (PKA-C). PKA-C is then translocate to the nucleus, where phosphorylates CREB, an IDP transcription factor. Inside the nucleus, the heat-stable protein kinase inhibitor regulates the activity of PKA-C and mediate the cytoplasmic translocation of the enzyme through the nuclear export receptor CRM1 (PDB-3GJX). The PKI:PKA-C, was modeled in the basis of the X-ray crystal structure 1ATP [6]. (adapted from [7]).

The first 3D structure of a protein kinase was the structure of PKA-C, solved in 1991 by Sunan Taylor and coworkers [28]. This pioneering work gave the possibility to map on a 3D structure the eleven conserved regions (I-XI) shared by all kinases, individuated through sequence aligning by Hanks and Hunter [5, 29]. Thank to that, it was possible understand that these residues not only are conserved, but are organized in secondary structure that are superimposable in all the member of the kinome (when the enzymes are in their catalytic active conformation) [30-33]. The catalytic subunit of PKA is a 40 kDa protein that folds in a bean-shape structure with two lobes: a small lobe formed by β-strands with only a short helical segment at the N-terminus, and a large lobe at C-terminus that is mostly helical [28] (**Figure 3.8**).

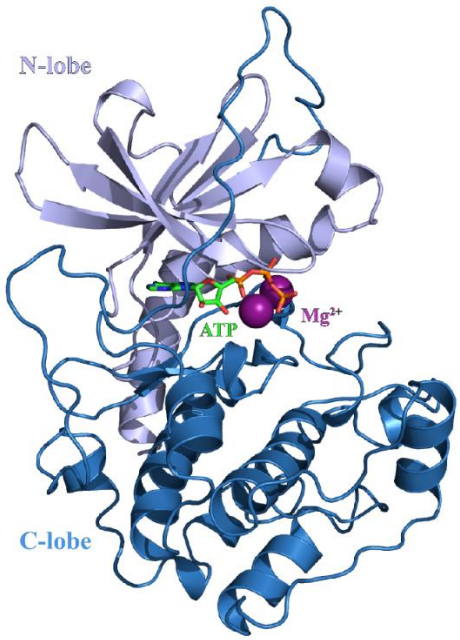

Figure 3.8 Crystal structure of the catalytic subunit of protein kinase A.
3D structure of PKA-C, in presence of Mg2+ ions and ATP (PDB-1ATP [6].

The small lobe is primary responsible of binding and positioning of ATP, while the large lobe provide a docking surface for substrates or inhibitor proteins. The active site cleft is positioned at the interface of the two lobes and harbor the nucleotide binging site. Through the coordination of two Mg^{+2} ions, the nucleotide is positioned several amino acids from various catalytic motif such as the DFG loop, glycine-rich loop, and catalytic loop [34]. The nucleotide's adenine ring completes the architecture of the catalytic spine (C spine), an array of hydrophobic residues that are involve in intramolecular allosteric signaling and activation [35]. The regulatory spine (R spine) instead is assembled upon phosphorylation of the activation loop [35, 36]. The PKA-C spine architecture was also observed in other members of the kinome, suggesting the relevant role that both the spines have in allosteric signaling [36] and regulation [37, 38].

The phosphoryl transfer catalyzed by PKA-C has been extremely studied [39, 40] and comprises three major steps: ligand (ATP and substrate) binding, chemical step (γ-phosphate transfer) and product release [20]. The fastest step is the chemical while the product release is the rate-determining step of the catalytic cycle [39]. During the catalysis the kinase undergoes to significant structural rearrangement and three major conformational states have been identifies by X-ray crystallography: open (apo form); intermediate (binary or nucleotide-bound form); and a close (ternary complex) [3]. It was hypothesized that ATP acts as an allosteric effector arranging the kinase for substrate binding [35, 41-43]. It was also observed that ATP binding shifts the conformational ensemble of the enzyme from the open to the intermediate state, and increases substrates

affinity through a K-type binding cooperativity [13, 19, 44-46]. The binding of substrate further shifts the ensemble toward the close form state [3].

Unlike the majority of the members of kinase family, whose activity is regulated by the transient addition of phosphate in the activation loop, PKA-C is assembled as a fully active enzyme and kept inactive by inhibitory proteins [3]. There are two principal classes of endogenous inhibitors that bind with high affinity and specificity PKA-C: the R subunit itself and the heat-stable protein kinase inhibitor (PKI)**.** Both proteins are structurally very dynamic with major regions of disorder, globular domains and/or well-defined secondary structures. In addition, both containing a substrate-mimicking sequence that dock inside the active site cleft preventing the bind of substrates **(Figure 3.9**) [3].

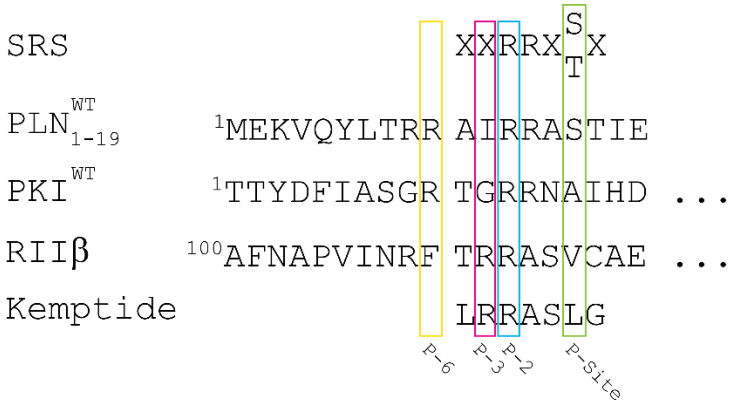

Figure 3.9 Consensus sequence for the PKA-C
Alignment of consensus sequences of natural PKA substrates, such as phospholamban (PLN) and kemptide, and inhibitor proteins.

3.3.1.1 Regulatory subunit

The regulatory subunits are modular, multifunctional and very stable proteins, and although there are different isoforms [47-52], all share a common domain organization (**Figure 3.10**).

There are identified two major classes of R subunit, RI and RII, which are functionally non-redundant and differ for the molecular weight, isoelectric points, amino acid sequence, auto-phosphorylation capacities, and antigenicity [53-56]. Each R-type presents two isoforms, α and β: (RIα, RIβ, RIIα and RIIβ), with RIα and RIIα expressed ubiquitously [49]. The R-β isoform is prominent expressed in brain [57], adipose tissues and in the liver [58]. Gene knockout experiments demonstrated that R subunit isoforms are not functionally interchangeable and the isoform diversity is critical biologically [58-62]. R subunits have a conserved domain structure composed by a dimerization /docking domain (D/D) at N-terminal, followed by two tandem cyclic-nucleotide binding domains (CNB) at the C-terminus, and a variable linker region between them. The linker region contains a substrate-like inhibitor sequence (IS), that docks to the active site cleft of C subunit, and multiple phosphorylation and ubiquitination sites [3, 53, 63, 64]. The D/D domain maintains the protomers as a dimer, and provides a docking surface for the A kinase anchoring proteins (AKAPs), that, in turn, anchor the holoenzyme to specific subcellular structure [65-70]. The CNB domains contains the high affinity cAMP binding site. In the presence of cAMP, each regulatory subunit binds two molecules of cAMP at separate allosteric binding sites and the holoenzyme dissociates into a regulatory subunit

dimer and two monomeric catalytic subunits [71-75]. The PKA-C activation, mediated by the second messenger cAMP, is a high cooperatively processes, that involves drastic structural rearranges in R, ending in the distinct localization release of the active C [3].

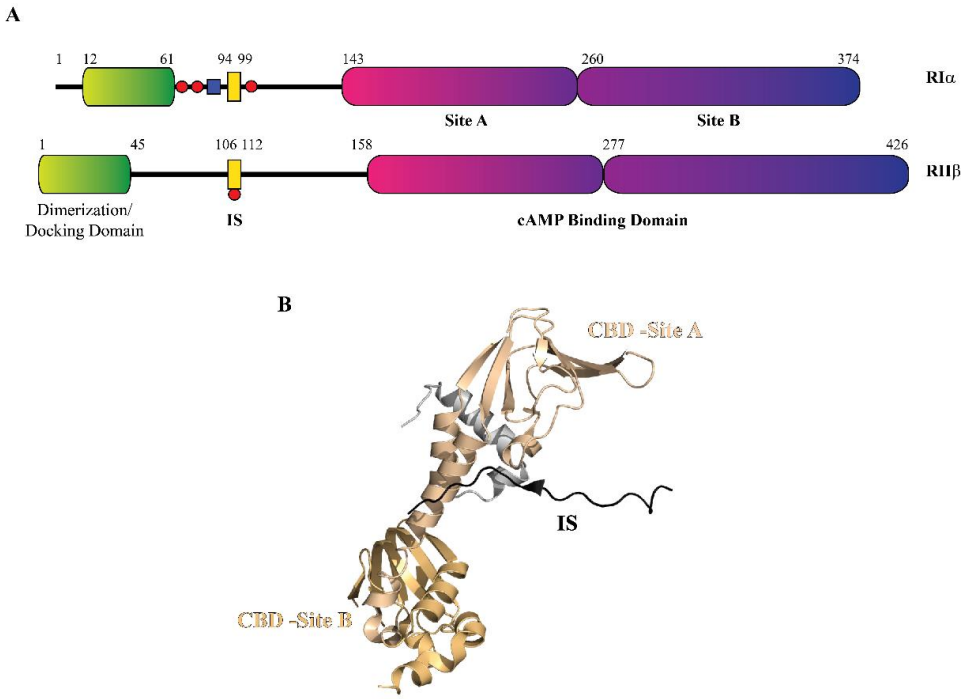

Figure 3.10 Organization of the regulatory subunits. (a) Schematic domain organization of RIα and RIIβ. Red circles indicate heterologous and auto-phosphorylation sites. (B) Domain organization on the structure of RIIβ (PDB-3TNP, [5]).

3.3.1.2 Protein kinase A inhibitor PKI

The heat-stable protein kinase A inhibitor, PKI, is a small peptide identified for the first time in 1962, as a contaminant substance that prevented the activation of phosphorylase kinase in skeletal muscle extracts [76-78]. Only few years later, Walsh and coworkers successfully purified the "substance" [79, 80] and demonstrated that selectively inhibits the activity of the free catalytic subunit of PKA, following cAMP mediated dissociation of the holoenzyme [81, 82]. PKI is a polypeptide (70-75 amino acids) that participated in the cellular regulation and localization of PKA-C. Like R subunit, PKI contains two functional domains: the inhibitory sequence and a PKA-C localization sequence (nuclear export signal) [3, 83].

The peptide is a potent competitive inhibitor of PKA-C [42, 84] and its binding activity are matched only by R subunits [85]. These two PKA-C endogenous inhibitors share the same recognition inhibitory sequence (pseudo-substrate sites) (**Figure 9**) however, PKI lacks a specific binding site for cAMP, so the PKI-mediated inhibition mechanism occurs specifically in the presence of cAMP [83]. The PKI pseudo-substrate sequence (PSS) is positioned near the N-terminus, within residues 15-22 (R_{15}TGRRNAI_{22}) [86, 87]. This sequence differ from a typical cAMP-dependent protein kinase substrate which contains Ser/Thr residues that can be phosphorylate by PKA-C (Arg–X–X–Arg–Arg–X–(Ser or Thr)–X) (**Figure 3.9**) [88]. In addition, the formation of high affinity complex with PKA-C, require the presence of both Mg^{2+} and ATP [42, 89]. ATP has a Km of 10 μM for catalysis but binds to C:PKI complex with a K_d of 60 nM,

while PKI alone has a K_d of 230 nM but, in presence of ATP, the Ki is about 0.2 nM [90, 91]. Studies of mutational and structure analysis have point out the importance of arginine residues (Arg-15, Arg-18, Arg-19) and isoleucine (Ile-22), that are required for the potent inhibition activity [28, 86, 87, 92, 93].

In addition to PSS, PKI contain a nuclear export sequence (NES), composed by several hydrophobic Leucine residues (37-46, LALKLAGLDI), that make the sequence one of the strongest nuclear export signals identified [94, 95]. Thanks to this sequence, PKI can enter inside the nucleus, bind PKA-C and translocate the enzyme in the cytoplasm [94, 96-98], where it can re-associate with R subunit to form the holoenzyme. Briefly, the catalytic subunit of PKA shuttles between the cytoplasm and the nucleus and phosphorylates proteins in both cellular compartments (**Figure 3.7**). The enzyme enters inside the nucleus by passive diffusion through pores in the nuclear membrane. Once inside PKA-C phosphorylates nuclear proteins, such as the transcription factor called cAMP-response element binding protein (CREB) [99, 100], that in turn acts as cAMP responsive element (CRE) promoters to activate gene transcription [99, 101-103]. The translocation of PKI:C complex is mediate by Chromosomal Maintenance 1 (CRM1), also known as Exportin1 [104, 105]. This 115 kDA protein is a nuclear protein export receptor that mediates the export of leucine-rich NES-bearing proteins through the nuclear pore complexes (NPCs) [106-110]. The cytoplasmic relocation of PKI happens only when the peptide is complexed with the kinase. As mentioned before, PKI is a fully disordered protein, and it is believed that only when PKI is bond to PKA-C, the NES become more

structured, and can binds CRM1 and mediate the nuclear-exportation of the enzyme [97, 111].

At present, three endogenous PKI isoforms (PKIα, PKIβ, PKIγ) have been identified in humans and mice that arise from three different genes. Each isoform is expressed in a variety of tissues throughout the body including skeletal muscle, testis, and heart [83]. Between the three isoforms, PKIα is the most widespread in the tissues and is also the most powerful inhibitor (Ki 0.22 nM) against PKA-C [112, 113]. This peptide is a fully disordered protein, composed by 75 amino acids. Crystallographic studies performed using a truncated version of peptide (PKIα5-24) containing the PSS [114], and NMR studies on full-length PKI [115] and on a peptide containing only NES sequence [116] have demonstrated the two functional domains assume a well-defined secondary structure upon binding with the respective binding partners. However, the other portions of the peptide remain highly dynamic, even upon the interaction with targets protein [3, 115].

PKIβ is a 70 amino acid peptide and share only 41% on amino acid identity with PKIα. Although the conserved residue between the two isoforms are located in both PSS and NES portions, PKIβ is significantly less potent inhibitor (Ki 7.1 nM) [112]. This significant discrepancy between the two peptide is attributed to the absence of a tyrosine residue (Try-7) and also to the presence of more unstructured portions [117].

PKIγ is the “youngest” within the three isoforms. It is composed by 75 residues and shares 35% homology sequence with PKIα [113]. As for PKIβ, the

conserved amino acids belong to PSS and NES portions and, as inhibitor (Ki 0.44 nM), is less effective than PKIα, but more than PKIβ. The unique feature of this peptide is the presence of a cysteine residue in position 13 [113].

PKI is a potent and selective endogenous inhibitor of the catalytic subunit of cAMP-dependent protein kinase A, that also is involved in the enzyme cellular localization. Initially, PKI was believed to be responsible for the regulation of basal activity of PKA-C [118], due to the fact the in certain tissues, such as rat heart and rabbit skeletal muscle, the peptide concentration would allow for the inhibition of approximately 20 % of total cellular PKA-C [119]. However, later studies revealed that tissue levels of PKI are probably much higher than those originally determinate [83]. Studies on PKIα knockout mice have highlighted that PKI play a role more crucial than a simply regulator of the basal level of the PKA-C activity [120]. The second physiological function of PKI is to regulate the nuclear activity of PKA-C and, therefore, regulate gene expression [121]. For example, studies conducted by Kawakami and Nakanishi, have demonstrated that PKIα is involved in brain morphogenesis and symmetrical left-right axis formation [122]. Several characteristics possessed by all the PKI members suggest that each isoform have a unique physiological functions that have not yet elucidate. For instance, the different isoforms exhibit a cell-type specific expression patterns in certain tissues, while the expression and intracellular distribution are developmentally, hormonally a cell-cycle regulated [83, 111, 123, 124].

Chapter 4

Structure and membrane interaction of the antimicrobial peptide Chionodracine

4.1. Chionodracine

Chionodracine (Cnd) is an anti-microbial peptide isolated from *Chionodraco hamatus*, an Antarctic teleost icefish [24]. Cnd is expressed predominantly in the gills and head kidney as an 80 amino acid precursor and cleaved into a mature 22 amino acid peptide (*FFGHLYRGITSVVKHVHGLLSG*). Sequence alignment suggests that Cnd belongs to the antimicrobial family of *Piscidin* (**Figure 4.1**) [117, 118]. This family is composed by antimicrobial peptide derived from fish with a high conserved histidine- and phenylalanine-rich N-terminus and a variable C-terminus [119]. The piscidin members (piscidin 1, 2, 3, and 4) displays a broad spectrum of antimicrobial activity against fish pathogens and, *in vitro*, display also anti-tumor activity against several cancer cell lines, such as HL60 [120], Hela, and 4T1 [121]. Previous studies on other piscidins, suggest that these peptides interact and disrupt the target membranes through the formation of pores [122].

The activity of Cnd was tested against various pathogens [24]. The peptide shows antimicrobial properties against *Psychrobacter* sp. TAD1 and TA144 (a natural icefish pathogens), and it is active toward Gram-positive (*Bacillus cere-*

us) ad Gram-negative (*Escherichia coli*) bacteria. No significant hemolytic activity toward human erythrocytes was showed by Cnd. Consequently, Cnd is a promising template to further develop small molecules with anti-microbial activity.

In this PhD thesis, we elucidate the membranolytic properties and structural characterization of Cnd using steady-state fluorescence spectroscopy and solution-state NMR. We found that Cnd is able to permeabilize membranes of bacterial organisms (*E. coli* and *Psychrobacter sp.*) and it has a high preference to interact with model negatively charged membranes, made by synthetic or natural phospholipids. The structure determined by solution-state NMR shows Cnd adopting a classic amphipathic helix, where the hydrophobic amino acids are embedded in the membrane while the positively charged residues lie along the membrane [8].

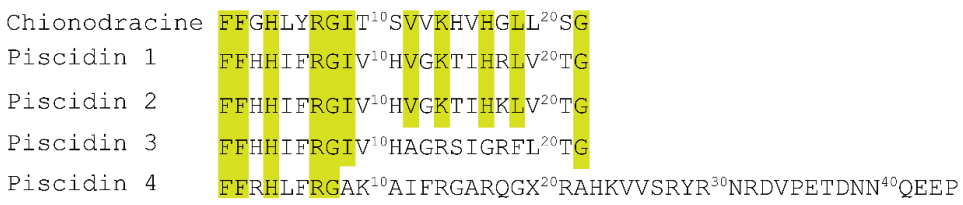

Figure 4.1. Sequence comparison inside the Piscidin family. The primary sequence of CND is aligned with the sequence of the other member of the family. The green boxes highlight the shared amino acids in the protein sequence. (Adapted [8]).

4.2 Material and Methods

4.2.1 Peptide synthesis

The Cnd peptide (*FFGHLYRGITSVVKHVHGLLSG*) was purchased from United Biosystems Inc., USA. The peptide concentration was estimated by light absorption at 280 nm (ε_{280} = 1490 M^{-1} cm^{-1}) before each sample preparation.

4.2.2 Phospholipid vesicle preparation

Large unilamellar vesicles (LUVs) with a diameter of 100 nm were chosen as membrane mimicking system (MMS) model. These vesicles were prepared by extrusion with an Avanti Polar mini-extruder through a polycarbonate membrane with 100 nm pore size (Avanti Polar Lipids Inc., USA). Briefly, appropriate amount of phospholipid powder of 1-palmitoyl-2-oleoyl-*sn*-glycero-3-phosphocoline (POPC or PC-100%); mixtures of POPC and 1-palmitoyl-2-oleoyl-*sn*-glycero-3-phosphoglycerol (POPG) in 70:30 molar ratio, and *E. coli* B (ATCC 11303) total phospholipid extract (Avanti Polar Lipids Inc.) [having a composition (wt/wt %) of PE (phosphatidyl-ethanolamine) 57.5%, PG 15.1%, CA (cardiolipin) 9.8% and unknown 17.6%.] was dissolved in chloroform in a heart-glass flask and dried using a rotary evaporator. The lipid film was, then, rehydrated with an appropriate buffer, incubated for about 2 hour, at 50 °C, in a water-bath, vortexed occasionally and subjected to 5 freezing-thawing cycles. The obtained multi-lamellar vesicle (MLVs) suspension was then extruded, more of 20 times, through a polycarbonate filter using Avanti Polar mini-extruder. Depending on the type of experiment performed, the rehydration buff-

er used was different. Briefly, in calcein leakage studies, the buffer was composed by 20 mM MOPS at pH 7.4 containing 0.8 mM EDTA, 70 mM NaCl, and 30 mM calcein. The excess of free calcein was eliminated from the calcein-loaded LUVs performing a size exclusion chromatography using a Sephadex G-50 package (Sigma-Aldrich). The calcein-encapsulated LUVs were eluted in the void volume of the mini-column, recovered and then resuspended in buffer with an appropriate osmolarity. For the other experiments, the rehydration buffer used is the analysis buffer itself. In both the preparations, the LUVs concentration was calculated by measuring the light scattering at 550 nm [123] . The PC-LUV (100%) is taken as a model of eukaryotic membranes while PC/PG (70:30)-LUV, is taken as a model of prokaryotic membrane. It was also used the total *E. coli* lipid extract whose phospholipid composition is not full characterized. They are all natural lipids, so we used them to monitoring the peptide behavior with natural phospholipids against synthetic.

4.2.3 Steady-state fluorescence experiments

A Perkin Elmer LS55 steady-state fluorescence spectrometer equipped with a thermostatic cell holder with magnetic stirrer was used for all the steady-state fluorescence studies. All the experiments were recorded at 25 °C and, to correct the polarization effects and to reduce the direct contributions from vesicle light scattering, some measurements were carried out with a cross-oriented configuration of polarizers ($Pol_{em}=0°$ and $Pol_{exc}=90°$) [77].

4.2.3.1 Outer membrane permeability assay

To study the permeabilization activity of Cnd, we used 1-aminonaphtalene-8-sulfonic acid (ANS) uptake assays [124]with *E. coli* BL21 (DE3) and *Psychrobacter* sp. TAD1 bacteria. An over-night culture of bacterial cells, inoculated into Luria-Bertani (LB) rich medium, was grown up to the mid-log phase. The cells were centrifuged and washed several times with buffer (10 mM Tris-HCl at pH 7.4, 150 mM NaCl and 0.8 mM EDTA) and then resuspended in the same buffer to achieve an OD_{600} of ~ 1.2. The fluorescent dye, ANS, was then added to a 1.0 mL of cell suspension and allowed to equilibrate. The cell suspension was then titrated with increasing amount of peptide, ranging from 1.0 to 15.0 μM, and, a fluorescence spectrum was recorded between 400 and 600 nm using an excitation wavelength of 360 nm and excitation/emission band-passes of 5.0. The disruption of the outer membrane was quantified by increasing in the fluorescence intensity and the blue shift of the spectra.

4.2.3.2 Partition studies

The interaction of Cnd with lipid vesicles was studied by monitoring the increase of the tyrosine (Try) fluorescence emission spectrum at λ_{em} = 320 nm upon excitation at λ_{exc} = 274 nm. These measurements were carried out with a cross-oriented configuration of polarizers. The emission spectra were recorded between 305 nm and 500 nm with excitation/emission bandwidths of 5.0 nm. Aliquots of LUVs rehydrated with the assay buffer (20 mM phosphate buffer at pH 7.4 with 150 mM NaCl and 0.8 mM EDTA) were added to a quartz cuvette

(12.5×12.5 mm) containing 1.0 μM or 10.0 μM of peptide. The peptide-lipid interaction was tested with LUVs of different composition [PC-100%, PC/PG (70:30) and *E. coli* Extract] and the lipid/peptide ratio tested ranged between 50 and 500. From each spectrum the background signal of both buffer and vesicles was subtracted. The molar partition coefficient (K_x) is defined, according to Wimley and White [76, 77, 125, 126], as:

$$K_x = \frac{([P]_{bilayer}/[L])}{([P]_{water}/[W])} \qquad [4.1]$$

where, $[P]_{bilayer}$ and $[P]_{water}$ are the bulk molar concentration of peptide in the bilayer and in the water, and [L] and [W] are the molar concentrations of lipid and water ([W] = 55.3 M), respectively. Considering that total concentration of peptide is the sum of the peptide in bilayer and in water, ($[P]_{tot} = [P]_{bilayer} + [P]_{water}$), the fraction of peptide, f_p, partitioned into the phospholipid vesicles, is:

$$f_p = \frac{K_x[L]}{[W] + K_x[L]} \qquad [4.2]$$

The valued of K_x were determined by the plot f_p vs $[L]$ using GraphPad Prism 6 software package (GraphPad Software Inc.). The experimental data were plotted according to the following equation:

$$\frac{I}{I_0} = 1 + (I_{max} - 1) f_p \qquad [4.3]$$

where I is the fluorescence intensity recorded for each titration point, I_0 is the fluorescence intensity of peptide in buffer; and I_{max} is the intensity after saturation of peptide-lipid binding. The molar partition coefficients for each lipid sys-

tems tested were evaluated at low peptide concentration (1.0 μM) in order to avoid the non-ideal behavior occurring at higher concertation [126].

4.2.3.3 Iodide quenching experiments

Iodide quenching of Tyr fluorescence was performed to evaluate the topology of the interaction between the Cnd with model membranes. These studies have been carried out in absence and presence of vesicles of different lipid composition [PC-100%; PC/PG (70:30), *E.coli*-LUVs], at a peptide/lipid molar ratio of 1:100, in presence of potassium iodide (KI). Aliquots of quencher stock solution (3.0 M) were added to the appropriate peptide concentration placed in a 1.0 mL cuvette. After each addition, a fluorescence spectrum was recorded. The excitation wavelength was set to 274 nm and the fluorescence spectra were recorded between 285 and 340 nm, with a band-passes of 5.0 nm and with a cross-oriented configuration of polarizers (Pol_{exc}=0° and Pol_{emi}=90°). All the spectra were corrected for dilution and for the absorption of fluorophores and quenchers. Data obtained were analyzed according to the Stern-Volmer equation for the collisional quenching (Appendix).

4.2.3.4 Calcein leakage studies

The kinetics of calcein leakage from lipid vesicles were followed by monitoring the increase of calcein fluorescence upon the addition of Cnd to the vesicle suspension. LUVs with different phospholipid composition [PC-100% and PC/PG (70:30)] were loaded with 30 mM of calcein, as previously described. The samples were prepared by adding serial concentrations of peptide, ranging

between 0.1-1.0 μM, to four different calcein encapsulated-LUVs concentration [from 12.5 to 100.0 μM]. The increase of calcein fluorescence was monitored at an emission wavelength of 520 nm, with an excitation wavelength of 490 nm, and excitation and emission band-passes of 2.5 nm, at temperature of 25 °C. The kinetic was followed for about 2000 s and the emission fluorescence of only LUVs was recorded for 5 min (baseline) before the peptide addition. Before each measurement, the integrity of the LUVs suspension was tested measuring the light scattering spectra between 540 nm and 560 nm, using an incident light of 550 nm [122]. The percentage of dye release was calculated as followed:

$$Dye \quad Leakage \quad (\%) = \frac{(F - F_0)}{(F_{Triton-X} - F_0)} * 100 \qquad [4.4]$$

where F is the fluorescence intensity upon addition of peptide, F_0 is the fluorescence before the addition of peptide and $F_{Triton\text{-}X}$ is the fluorescence upon the addiction of Triton X. To describe the kinetics of dye leakage from vesicles induced by peptide, the fluorescence traces were fitted with a double exponential equation [123]:

$$F_t = F_{eq} - a_1 e^{-k_1 t} - a_2 e^{-k2t} \qquad [4.5]$$

where F_t and F_{eq} are the fluorescence at time t and at $t \rightarrow \infty$ respectively, the constants a_1 and a_2 represent the fractions of the two kinetic components and k_1 and k_2 are the respective constants expressed in s^{-1}.

4.2.4 NMR spectroscopy study

4.2.4.1 Sample preparation and spectroscopy

The lyophilized peptide was dissolved, to a final concentration of ~1.5 mM, in aqueous solution (5% $^{2}H_2O$, 95% $^{1}H^{2}O$) congaing 300 mM of perdeuteraded DPC (Cambridge Isotope Laboratories) and 20 mM phosphate buffer at pH 6.5. 2D [^{1}H, ^{1}H] TOtal Correlation SpectroscopY (TOCSY) [127, 128] (50 and 70 ms mixing time) and 2D [^{1}H, ^{1}H] Nuclear Overhauser Enhancement SpectroscopY (NOESY) [129, 130] (70-300 ms mixing time) experiments were recorded in phase-sensitive mode using time-proportional phase incrementation (TPPI) for quadrature detection in the indirect dimension. The experiments were acquired with 64 scans (256 and 1024 complex data points in the t_1 and t_2 dimensions, respectively). The 90 °pulse width was 30 kHz, and the recycle delay of 1 s. The spectral widths were 5400 Hz t_1 and 7200 t_2 dimensions. The NMR experiments were acquired at 300 K on a Varian-Inova 600 MHz spectrometer provided by University of Minnesota NMR Center (University of Minnesota – Twin Cities, Minneapolis, MN, USA). [^{1}H, ^{13}C] Heteronuclear Single Quantum Coherence (HSQC) [131] and Heteronuclear Multiple Bond Correlation (HMBC) [132] experiments were acquired on a 900 MHz Ultra-shield Bruker Spectrometer, operating at 303 K. The ^{13}C experiments were carried out at natural abundance. The NMR data were processed using *NMRPipe* [133]and analyzed with *Sparky* [134] software packages. The spectra were assigned using the approach described by Wuthrich [135, 136].

4.2.4.2 Structure calculation

For the structural calculation the NOE cross-peaks from 150 and 300 ms mixing time 2D [^{1}H, ^{1}H]-NOESY experiments were used. The NOE volumes were calibrated using the average NOE volumes from resolved aromatic vicinal protons of Tyr-6, and classified as strong, medium, and weak, corresponding to distance restrains of 1.8-2.9, 1.8-4.5, and 1.8-5.0 Å, respectively. To obtain the dihedral constraints for residues 3 to 19, *TALOS* + software was used [137].

The Cnd conformers were calculated starting from an extended conformation of the peptide and minimized using a hybrid simulating annealing (SA) energy minimization protocol, supplied in *XPLOR-NIH* program [138]. About 100 conformers were generated randomly at an initial temperature of 5000 K with 6000 high temperature steps, 3000 cooling steps, and a step size of 5 fs. The final refinement stage of the structure ensemble was performed starting at an initial temperature of 500 K and using 30000 cooling steps, with a step size of 1 fs. Over the 70 obtained conforms, no one shows (*a*) NOE violations greater than 0.5 Å, (b) bond violations greater than 0.05 Å, and (c) bond angle violations greater than 4°. The 40 lowest energy conforms were further analyzed with Molprobity (nota), a structure validation program.

4.3 Results

4.3.1 Outer membrane permeability assay

To assess the ability of CND to damage the integrity of the bacterial membrane, the ANS fluorescence assay was performed, using as *Escherichia coli* BL21 (DE3) and *Psychrobacter* sp. TAD1 as model organisms (**Figure 4.2**). Due to the hydrophobic nature of ANS, when the bacterial outer membrane is intact, it is not able to pass through it, and the fluorescence is weak. If the membrane is damaged, the ANS can penetrate inside the cell, causing a drastic increase of the fluorescence emission spectrum associated with a blue shift. Upon the addition of the CND, it is observed an increase of the ANS fluorescence spectrum and a blue shift of the λ_{max} of emission. This indicate that CND is able to disrupt the integrity of the outer membrane of both the prokaryotic species tested (**Figure 4.2**), causing the relocation of ANS in the periplasmic space. The observed effect is dose-dependent and is significant even at low peptide concentrations.

4.3.2 Partitioning studies

To assess and quantify the interaction of CND with model membranes that mimic the phospholipid composition of the natural membranes, partition studies were performed. In particular, we recorded the fluorescence emission spectra of Tyr-6 upon addition of increasing amount of LUVs of different lipid compositions (F**igure 4.3 A and B**).

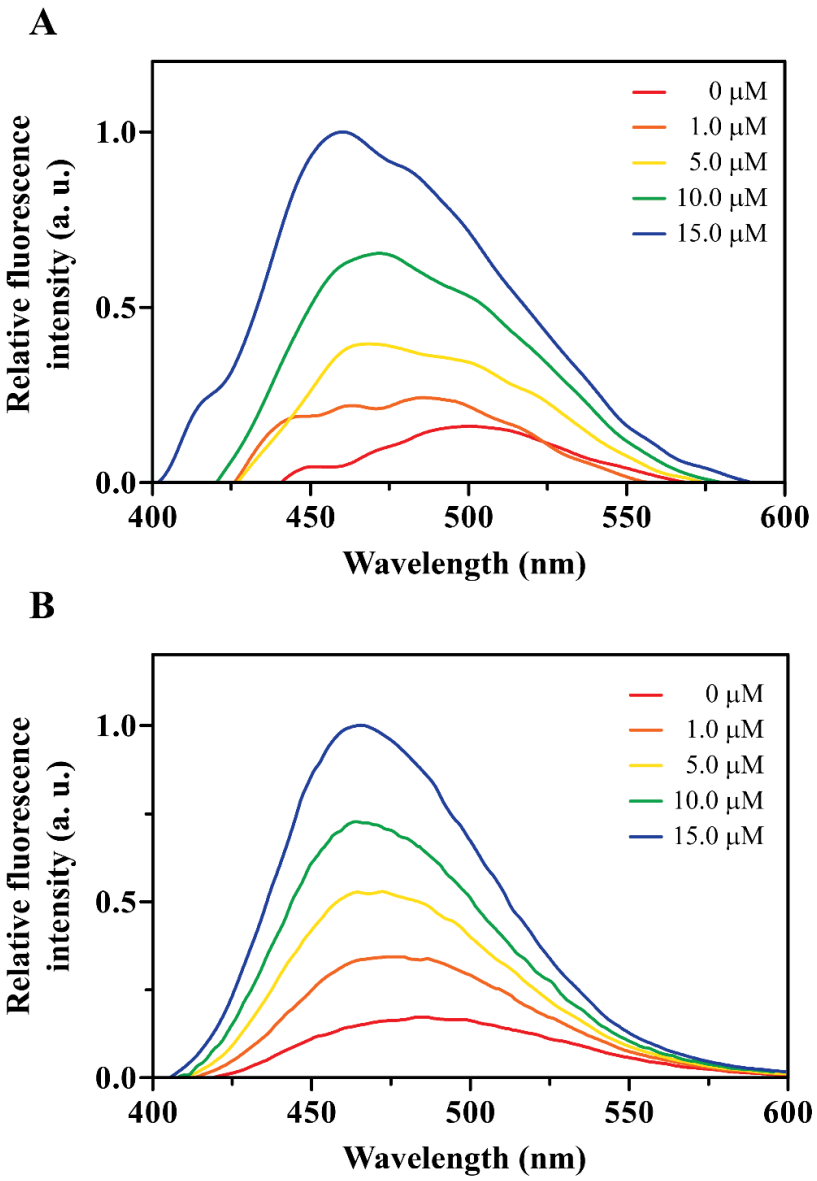

Figure 4.2. Outer membrane permeability assay. Permeabilization of the external membrane of the two Gram-negative bacteria, *E.coli* BL21 (DE3) (A) and *Psychrobacter* TAD1 (B).

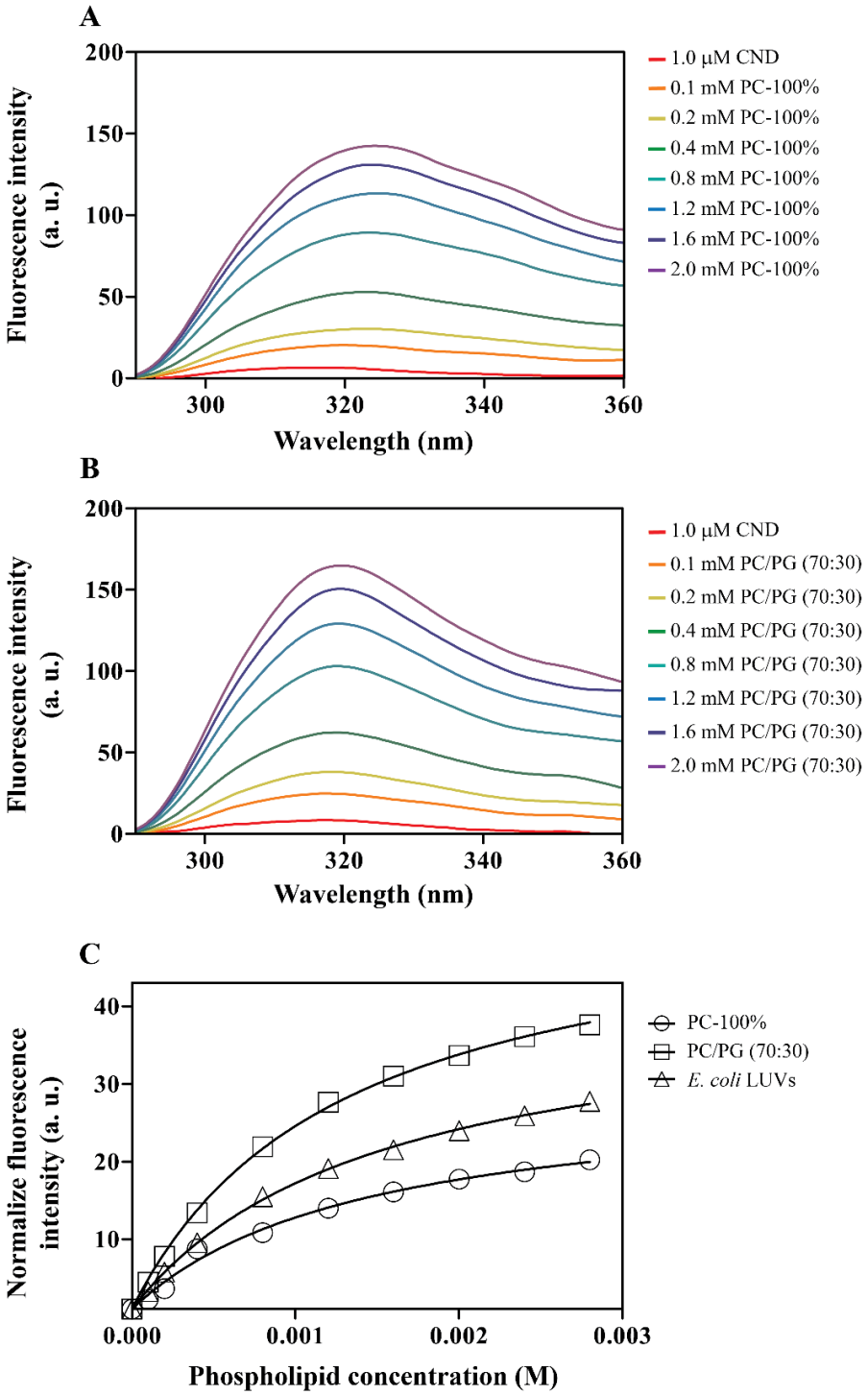

Figure 4.3. Partition experiments. Cnd fluorescence in absence and presence of increasing concentration of LUVs composed by (A) 100% of PC and (B) a mixture of PC/PG (70:30 molar ratio). In C is reported the binging isotherm for the peptide upon addition of increasing amount of vesicles. The CND concentration was 10.0 μM.

The addition of LUVs caused an increase of the emission intensity of the Tyr indicating that the chemical environment around the fluorescence probe changed, going from a less to a more hydrophobic environment. The increase of fluorescence is also depending on the amount of LUVs added. This dependency is also highlighted by the analysis of the binding isotherms derived from equation 4.3 (**Figure 4.3-C**). The mole fraction partitioning coefficients (K_x) calculated for the titration experiments ranging from 3×10^4 to 2×10^5 (**Table 4.1**).

Table 4.1 Partition parameters for CND calculated from the titration of the peptide with LUV of different phospholipid composition.

Peptide Concentration	Lipid composition	K_x	ΔG, (kJ/mol)
1.0 μM	PC-100%	$(3.43 \pm 0.26) \times 10^4$	-25.9
	PC/PG (70:30)	$(4.91 \pm 0.29) \times 10^4$	-26.7
	Total *E.coli* extract	$(1.83 \pm 0.08) \times 10^5$	-30.0

From these values, it was possible to calculate the Gibbs free energy $\Delta E = -RT \ln K_x$, where R and T are the gas constant and the absolute temperature of the system, respectively) for the water/bilayer partition (**Table 4.1**). High values of K_x are representative of the fact that the peptide, in presence of lipid bilayers, is preferentially partitioned on the surface of the bilayer. The K_x values observed for CND, suggest that the peptide interacts with the LUVs, and the Tyr is involve in this interaction. It is also noted that the K_x values and the ΔG values measured for POPC/POPG (70:30) LUVs are higher than the ones recorded for the other vesicle used. CND also showed a higher propensity to partition into *E.coli* extract lipid vesicles. This can be explained taking in con-

sideration the charge effects and also the "more native-friendly" phospholipid composition. Analogous results have been reported for indolicin [139].

4.3.3 Intrinsic fluorescence quenching experiments

Studies of quenching of the emission spectra of Tyr-6, using Iodide (I^-) as quencher, were performed to evaluate the degree of peptide exposure to the bulk solvent. The fluorescence spectra of CND in buffer decreased in a concentration-dependent manner upon addition of KI in the peptide solution in absence (**Figure 4.4-A**) or presence of LUVs (**Figure 4.4-B, C, D**). The Stern-Volmer plots for the quenching of Tyr are showed in (**Figure 4.5**). The curves are linear with the quencher concentrations, indicating the presence of dynamical quenching [140]. In **table 4.2** are reported the K_{SV} values obtained from the slopes of the curves. The higher value of K_{SV} (~ 10 M^{-1}) is obtained for CND in buffer, indicating that the fluorophore is easily accessible to the quencher. In presence of LUVs, the K_{SV} are 3-6 time smaller than in buffer only, suggesting a reduced accessibility of Tyr due to the partition into the interfacial region of the phospholipid bilayer.

Table 4.2 Stern-Volmer quenching constant (K_{SV}) and percentage of I^- quenching for CND in the presence of vesicles of different lipid composition. The peptide/lipid molar ratio was 1:100 in all the case.

	K_{SV} (M^{-1})	$1/K_{SV}$ (M)	Percentage of quenching
Aqueous buffer	10.4 ± 0.2	0.096	100
PC-100% LUVs	2.9 ± 01	0.340	28.4
PC/PG (70:30) LUVs	2.5 ± 01	0.408	23.6
Total *E.coli* extract LUVS	1.6 ± 0.2	0.625	15.4

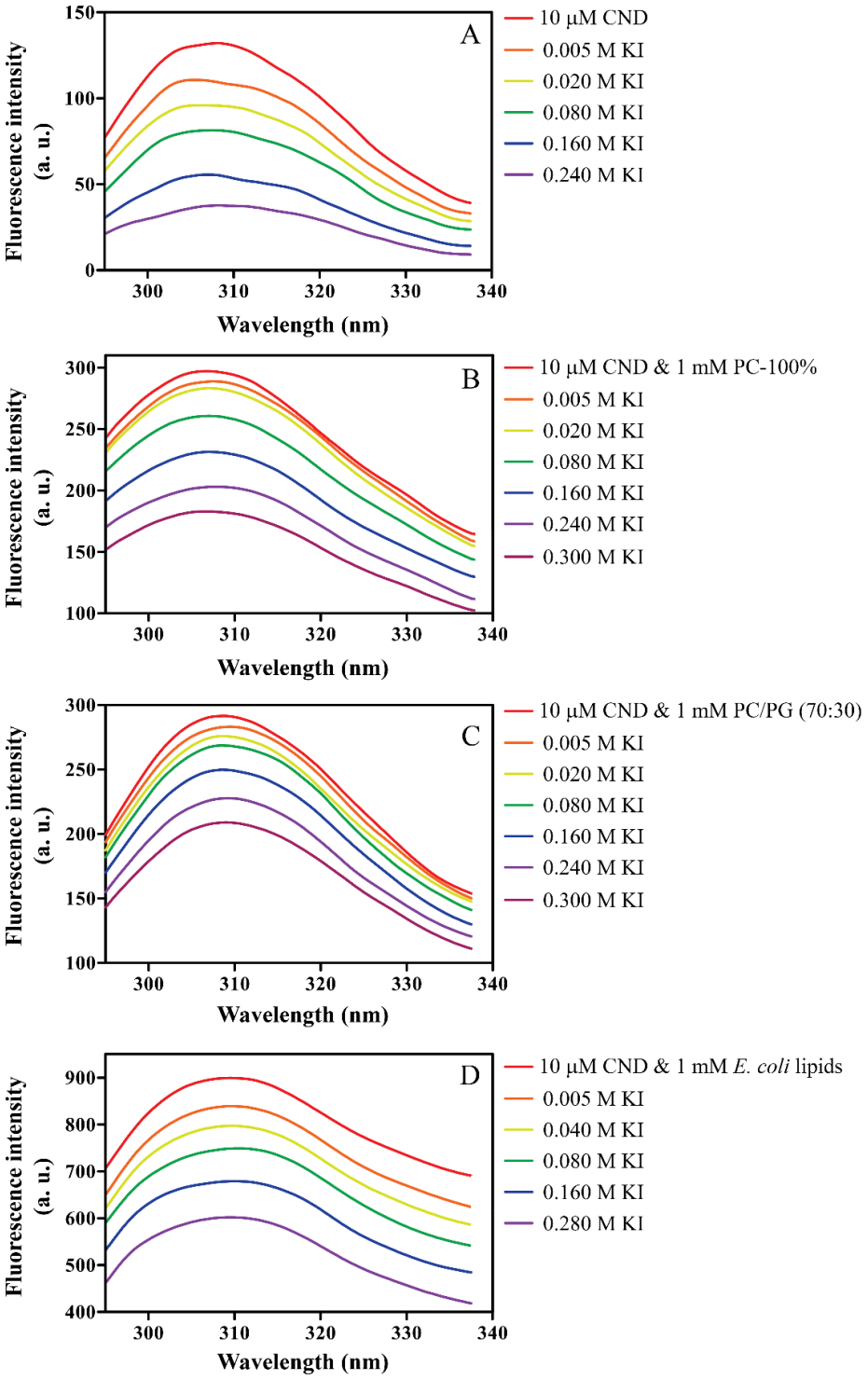

Figure 4.4. Iodide quenching experiments. Quenching of the intrinsic fluorescence of CND in absence (A) and in presence of phospholipid vesicles of different composition: (B) PC-100%, (C) PC/PG (70:30), and (D) *E. coli* total extract.

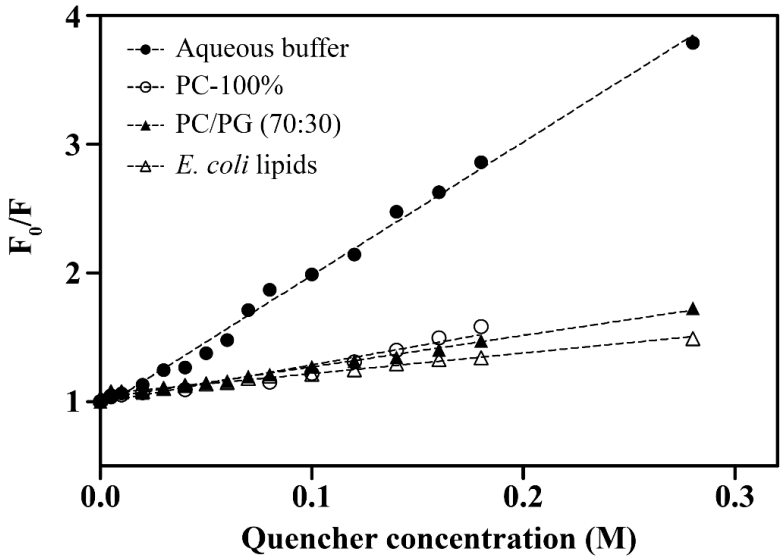

Figure 4.5. Stern-Volmer plots for the Tyr quenching of CND. The graph reports the plots for the intrinsic fluorescence quenching of the peptide in aqueous buffer and vesicles made from PC-100%, PC/PG (70:30) and *E. coli* lipid extract.

The quenching experiment, like the partitioning one, shows that the peptide interacts strongly with POPC/POPG and *E. coli* lipid extract LUVs than with POPC-100%. These evidences indicate not only that the N-terminal portion of CND (where Try is located) is deeply involves in the membrane binding process, but also that the peptide preferentially interact with charged membrane. During this interaction, the Tyr residue is thoroughly immerse in the phospholipid bilayer and not easily accessible to the quencher.

4.3.4 Calcein leakage studies

The membrane permeabilization ability of CND was studied monitoring the leakage of calcein from calcein-loaded vesicles upon addition of peptide. Calcein-loaded LUVs were prepared as previously reported. When calcein is entrapped inside the LUVs, due to its high concentration (30 mM), a self-quenching phenomenon is establish and the fluorescence is very weak [123, 141]. Upon the addition of CND, we observed a gradual increase of calcein fluorescence, suggesting that the peptide interact with the lipid bilayers, causing the disruption of the membrane integrity (**Figure 4.6**). In fact, the release of calcein in the external compartment is resulting in a calcein dilution, dequenching, and increase of fluorescence intensity [123]. To confirm that the release of calcein observed was due to the peptide/vesicle interaction and not to the self-LUV leakage, the integrity of the vesicle was tested through light scattering. In **table 4.3** are reported the relative leakage capabilities of CND, at different peptide/lipid molar ratio, and in presence of LUVs of different composition.

Table 4.3 Relative leakage capabilities of CND, ad different peptide/lipid molar ratio, in presence of LUVs of different lipid composition.

Peptide/lipid (molar ratio)	**Relative leakage**		
	PC-100%	**PC/PG (70:30)**	***E. coli* total lipid extract**
1/25	63%	100%	18%
1/50	26%	90%	13%
1/100	11%	60%	9%

We observed that dose-response of CND-induce calcein release is more effective in presence of negatively charged membrane, especially at low peptide/lipid molar ratio. The low value of calcein leakage obtained for total lipid extract from *E. coli* was reported even by Vogel et al. for tryptophan rich cathelicidin antimicrobial peptides [139]. They attributed the low value to the complexity of the *E. coli* extract (17 % of the phospholipid composition is still unknown) that make the vesicle less probe to disruption.

The calcein fluorescence profile was also examined using a method developed by Tatulian and coworkers [123]. While kinetics and level of calcein release were dependent upon the type and the concentration of the peptide and the lipid composition of vesicle membrane, all kinetic curves can be fitted with a double exponential character (**Figure 4.6**). In **table 4.4** are reported the kinetic parameter calculated from this fitting. All kinetic curve obtained in the calcein efflux studies demonstrated a double exponential character, regardless the lipid composition of LUVs assessed. In contrast the kinetics and the level of calcein release are dependent to the lipid composition and the concentration of peptide. Calcein release efflux performed by CND in presence of charge lipid on the surface of LUVs is usually more effective and quicker than the calcein release form LUVs that mimic the eukaryotic membrane.

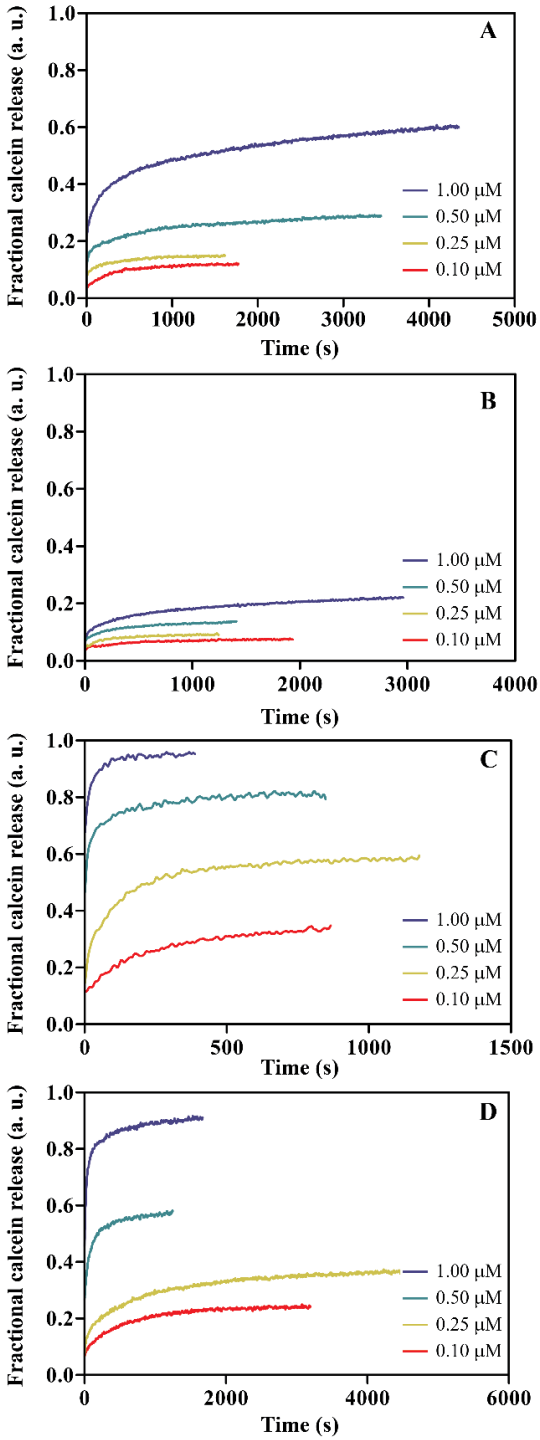

Figure 4.6. Kinetic of calcein leakage from LUVs after addition of CND. From 01 µM through 10 µM. The curve are experimental data normalized by Triton-X. In panel A and B are reported the calcein release kinetic recoded for 25 µM and 50 µM of PC-100% LUVs, respectively. Panels C and D are the kinetic of calcein efflux for 25 µM and 50 µM of PC/PG (70:30) LUVs.

Table 4.4 Kinetic parameters for calcein release from LUVs of different lipid composition upon addition of increasing amount of CND. The parameters derived from the data fitting with the equation 4.5.

25 μM LUVs concentration

[P] (μM)	F_{eq}		a_1		a_2		k_1 (s^{-1})		k_2 (s^{-1})	
	PC	PC/ PG	PC	PC/ PG	PC	PC/ PG	PC	PC/ PG	PC	PC/ PG
0.10	0.125	0.379	0.036	0.145	0.053	0.127	0.00110	0.00147	0.0051	0.0086
0.25	0.150	0.586	0.049	0.174	0.024	0.225	0.00225	0.00354	0.0226	0.0156
0.50	0.336	0.813	0.113	0.143	0.076	0.225	0.00026	0.00512	0.0036	0.0815
1.00	0.641	0.950	0.239	0.148	0.167	0.165	0.00041	0.01894	0.0061	0.1151

50 μM LUVs concentration

[P] (μM)	F_{eq}		a_1		a_2		k_1 (s^{-1})		k_2 (s^{-1})	
	PC	PC/ PG	PC	PC/ PG	PC	PC/ PG	PC	PC/ PG	PC	PC/ PG
0.10	0.092	0.242	0.026	0.139	0.023	0.032	0.000275	0.001436	0.0036	0.0108
0.25	0.097	0.368	0.023	0.178	0.030	0.086	0.001250	0.00079	0.0100	0.0071
0.50	0.145	0.578	0.041	0.107	0.032	0.207	0.001064	0.00240	0.0097	0.0168
1.00	0.245	0.910	0.101	0.150	0.055	0.361	0.00048	0.00213	0.0056	0.0348

4.3.5 Chionodracine structure determination

For the structure determination of CND, the peptide was reconstituted in DPC micelles. Performing 2D [^{1}H-^{1}H]-TOCSY and 2D [^{1}H-^{1}H]-NOESY spectra, we obtained sequence specific resonance assignments. Due to the slow tumbling of the peptide in micelle, it was not possible calculate the *J* coupling constants [63, 142-144]. The complete spin system assignment was achieve using the NOESY-walk method [136] (**Figure 4.7**), and a total of 240 NOEs were as-

signed (**Figure 4.8 A**). From the analysis of the natural abundance ^{13}C-edited HSQC, it was possible to assign $C\alpha$ and $C\beta$ of each amino acid spin system. The NMR chemical shift values estimated were used to calculate the secondary structure propensity [145, 146]and the dihedral angles using Talos+ [137]. In **figure 4.8-B** is reported the random coil index derived order parameter S^2 (RCI-S^2) [146], that is used to predict protein flexibility. RCI-S^2 values less than 0.5 indicate dynamic residues. The calculation of the structure was performed using Xplor-NIH program. The conformers obtained confirm the prediction according to which, the peptide assume an amphipathic α-helical conformation between residues 5 through 20 (**Figure 4.9**).

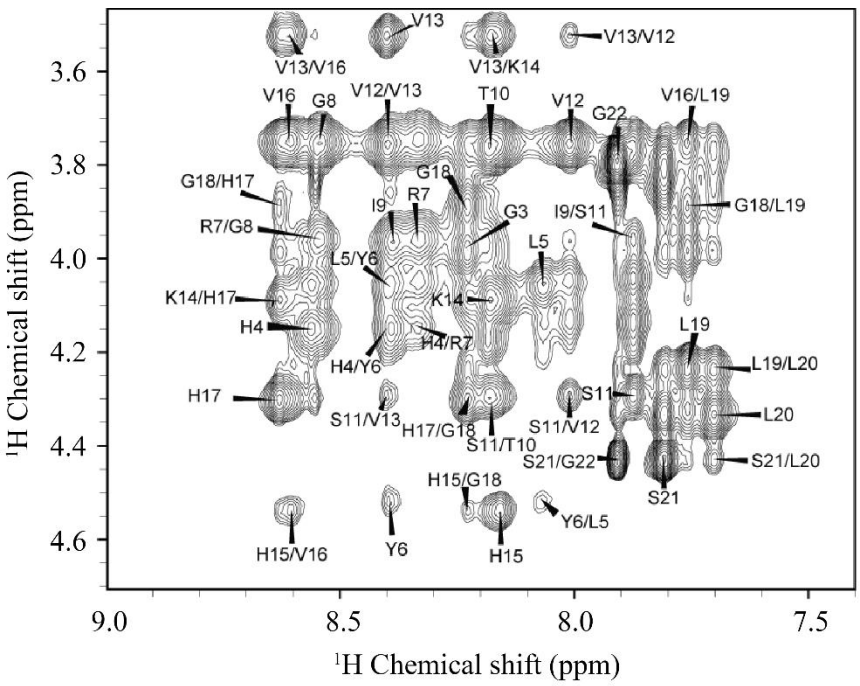

Figure 4.7. Fingerprint region of CDN extracted from the 2D [1H-1H] NOESY experiment at 300 ms mixing time. The peptide was reconstituted in DPC micelles. The spectrum was used to solve the 3D-structure of CND.

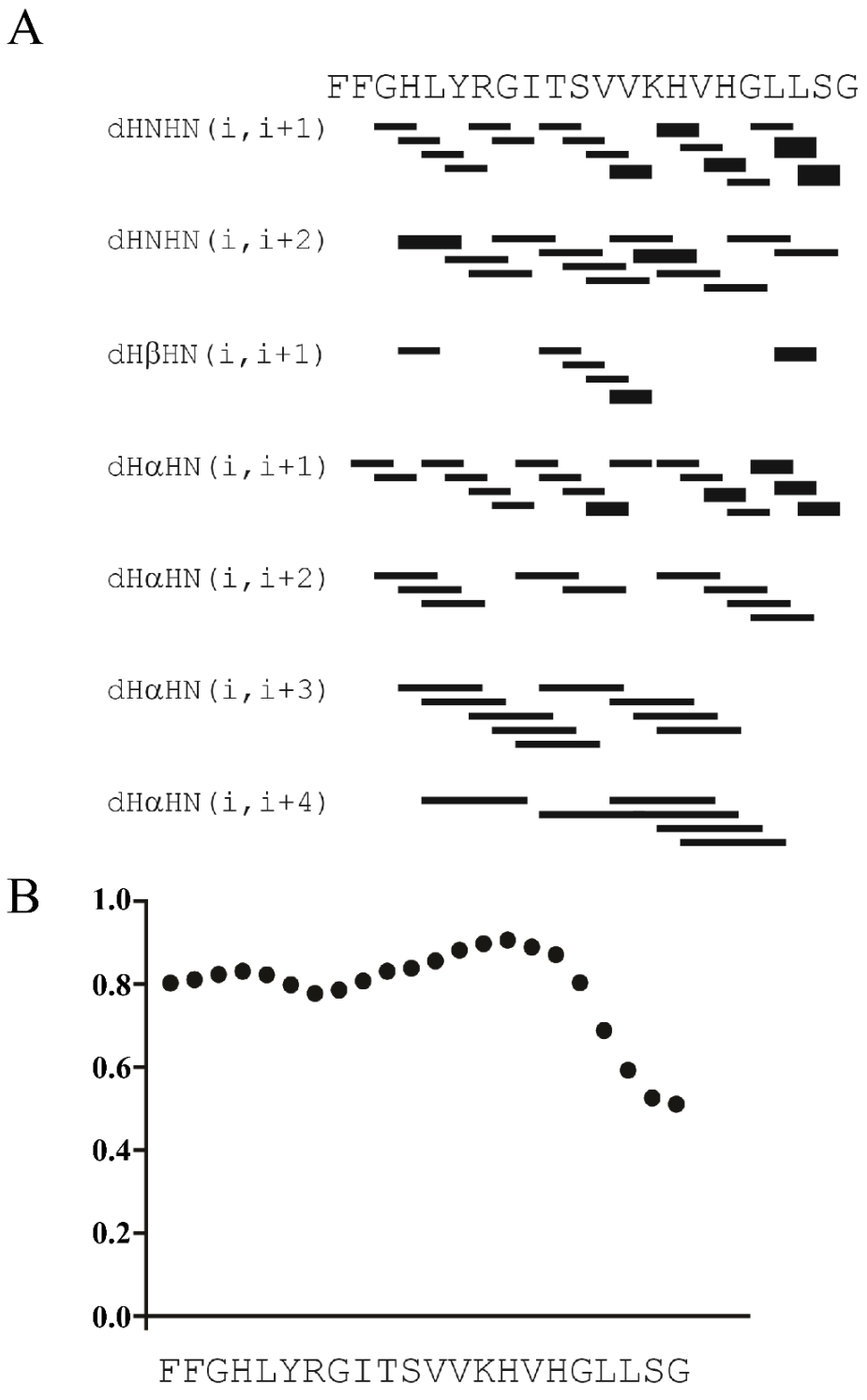

Figure 4.8. Summary of structural parameters. Backbone NOEs pattern for CDP in DPC micelles. The thick line correspond to strong NOE, while the thinner line represent medium and weak NOEs (A). In panel B is reported the predicted order parameter RCI-S^2.

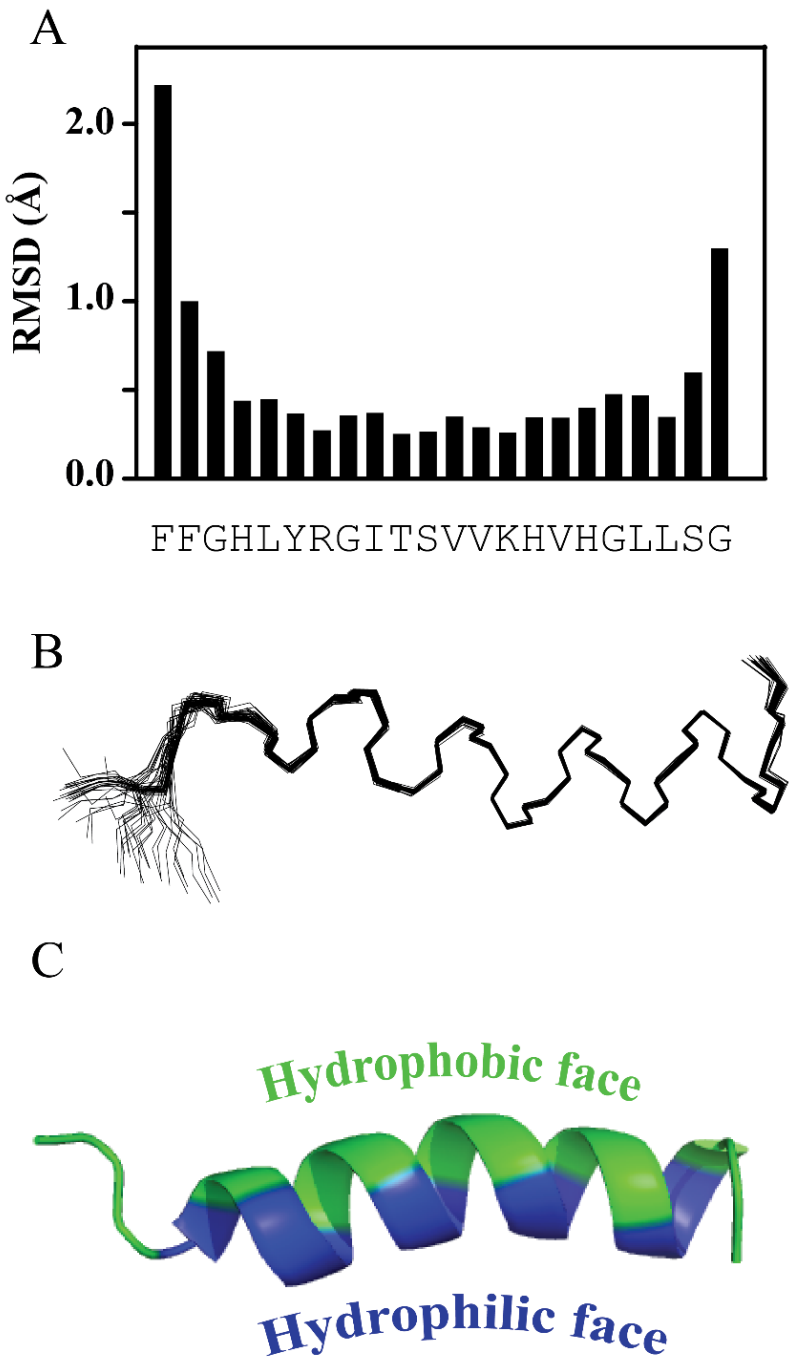

Figure 4.9. NMR structure model of CND. (A) Histogram of backbone RMSD vs residues for the final 40 conformers. (B) Conformational ensemble showing the convergence of the structures for heavy atoms of the backbone. (C) Representative structure=re of CND in DPC micelle. The peptide assume a conical amphipathic α-helix, with the repartition of the hydrophobic residues on one side on f the helix (blue), and the hydrophilic in the other side (green).

4.4 Discussion and conclusion

Over the last three decades, the extensive use of traditional antibiotics has resulted in the development of new strains of bacteria that are resistant to almost all the available antibiotics [38, 147]. AMPs have been identified as an alternative to traditional antibiotic agents due to their ability to kill pathogens. Most of the AMPs discovered during the last 65 years, have a broad spectrum activity against the major pathogenic organisms. In particular, AMPs derived from fish are attracting attention, because they are active at high salt concentration and in a wide range of temperature [119].

We identify and characterized an antimicrobial peptide, *Chionodracine*, isolated from the gills of the Antarctic teleost fish, *Chionodraco hamatus* [24]. This peptide showed to be able to interact and perturb the stability of biological membrane and synthetic phospholipid bilayers, preferring the bilayer that mimic the lipid composition of prokaryotic organisms. CND showed to have a strongest affinity and disruption activity toward charged membranes [8]. The presence of anionic phospholipid, not only lower the Gibbs partition energy by about 4 kJ/mol (**Table 4.1**) but increase the rate of calcein release compared to the zwitterionic lipid system. The ability of CND to disrupt the membrane integrity was evidenced by both calcein leakage study and outer membrane permeability assay. The studies demonstrated that CND interact with phospholipid membrane in a dose-response manner, based on both peptide-to lipid molar ratio and membrane lipid composition. In presence of LUVs, CND is partitioned

in the lipid surface with the N-terminus deeply involves in peptide/lipid interaction [8]. This observation was highlighted by both fluorescence quenching and the NMR studies. In fact, in n presence of LUVs, the estimated Stern-Volmer constants for the collisional quenching (K_{SV}) are 3-6 fold smaller than the one calculated for the peptide in solution. This means that the Tyr is less accessible to the quencher when lipids are present. The Tyr residues is located at position 6, in the N-terminal portion of the peptide, surrounded by other aromatic residues. The presence of highly concentrate aromatic residues at N-terminus suggests that this part can acts as an anchor for the peptide in the lipid bilayer (nota), while the C-terminus is less involved. This evidence is further confirmed by the NMR structure obtained in DPC micelles. Like other members of the piscidin family [72, 148, 149], CND undergo a disorder-to-order transition into a well-structured amphipathic α-helix upon the interaction with lipid bilayer. This 3D conformation is a well-known membrane-binding motif in which the hydrophilic and the hydrophobic sites are involve in the interaction with membrane [150, 151]. In this structure, there is a repartition of the amino acid residues on the two side of the helix. The resulting structure is a polarized helix with the charged amino acids on the hydrophilic portion, and the hydrophobic residues in the other [72]. The NMR 3D-structure showed CND interacts with the phospholipid membrane in way that the non-polar face is in contact with the hydrophobic portion of the membrane while the polar residues are oriented toward the solvent/peptide interface.in this way, the positive charged residues interact with the head group of the phospholipid [8].

Accordingly to what we has been reporting so far, CND is emerged as a possible candidate as antibiotic agent due to its antimicrobial and almost no hemolytic activity against eukaryotic cell (data not reported).

Chapter 5

Characterization of membrane interaction abilities of Chionodracine mutant using fluorescence spectroscopy

5.1 Chionodracine mutants

In the last 30 years, there has been an increase in the number of photogenic organisms that have developed antibiotic resistance [23, 29-31]. As a consequence, there is growing interest in discovery and development of antimicrobial peptides for clinical application. However, most of natural AMPs do not appear to be highly optimized for antimicrobial activity. Nature seems to have preferred creating multiple modestly active peptides, with concomitant immunomodulatory and synergic activities, over super specialized AMPs[152]. Therefore, there is increasing interest in using existing AMPs as templates for optimized activity and selectivity for anti-microbial activity.

In the previous chapter we elucidated the antimicrobial activity and solved the NMR 3D-structure of *Chionodracine*, an AMP isolated from the immune system of the Antarctic teleost *Chionodraco hamatus* [24]. From these studies, CND emerged as a promising AMP due to its ability to interact and disrupt the integrity of natural and synthetic charged membranes, even at low concentration. In solution, CND is unstructured and undergoes a disorder-to-order transition, assuming an amphipathic α-helical 3D-conformation in presence of a

phospholipid bilayer [8]. Based on this structure, three different mutants were designed using CND as a template to try to improve the antimicrobial activity of the peptide (**Figure 5.1; Table 5.1**). The mutations were designed to increase the positive charge and hydrophobic moment of CND, so to promote peptide affinity for the negatively charged membrane. In particular, the mutant called KS-CND, serine 11 and 22 were replaced with lysine (Lys). In a second mutant, KH-CND, histidine 4, 15 and 17 were replaced with Lys and, in the third mutant, all the histidine and serine residues were replaced by Lys (**Figure 5.1; Table 5.1**). Additionally, all the mutants have also a tryptophan (Trp) residue in position 1 instead of a phenylalanine to facilitate the use of steady-state fluorescence studies. This chapter reports the characterization of the activity and binding features of CND mutants performed using steady-state fluorescence spectroscopy studies. We found that the mutations have increased the antimicrobial properties of the peptides, but also their ability to interact with phospholipid bilayer, making them more powerful and promising antimicrobial peptide than CND.

TABLE 5.1. Sequences and physical-chemical characteristics of CND and its design mutants. Most of the values reported were obtained using ExPASy-Prot Param Tool and Helical wheel project (Raphael Zidovetzki PhD, UCR). In red are highlighted the mutated residues.

Peptide name	Sequence	Net charge at pH 7.0	pI	Hydrophobic moment (μ_H)
CND	FFGHLYRGITSVVKHVHGLLSG	+ 2.3	9.99	5.86
KS-CND	WFGHLYRGITKVVKHVHGLLKG	+ 4.3	10.46	7.49
KH-CND	WFGKLYRGITSVVKKVKGLLSG	+ 5.0	20.58	6.19
KHS-CND	WFGKLYRGITKVVKKVKGLLKG	+ 7.0	10.75	7.51

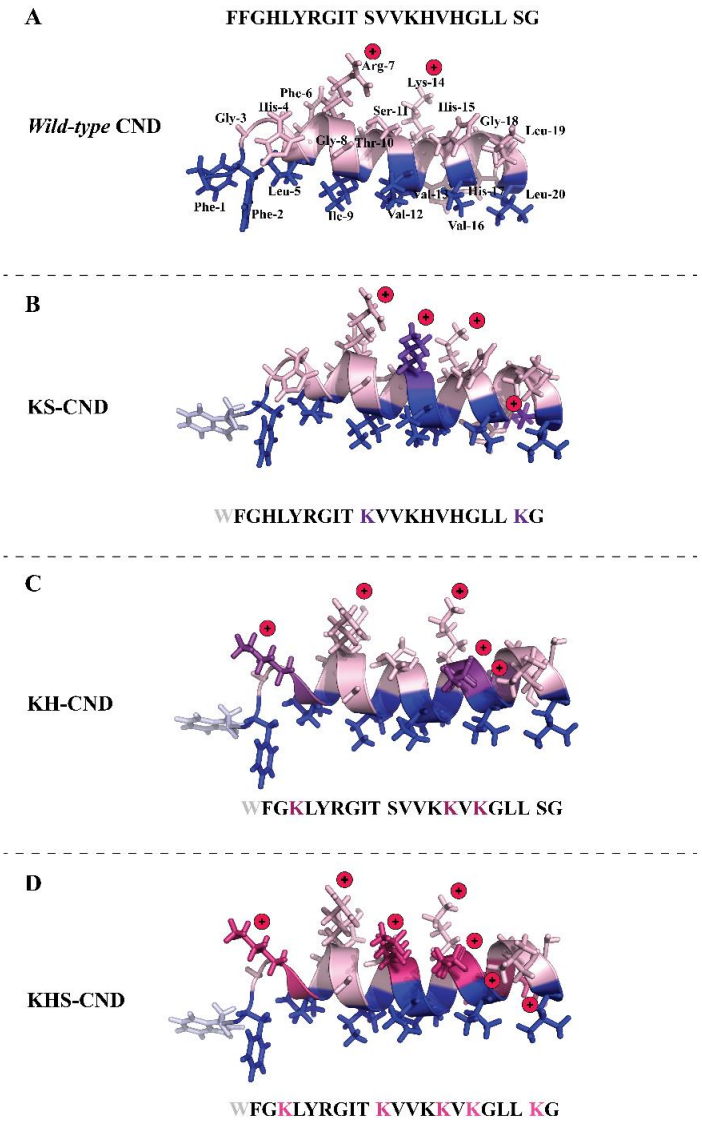

Figure 5.1 CND and its derived mutants. (A) CND in amphipathic α-helical conformation (structure obtained as describe in chapter 4).In the panels B, C, and D are showed the sequence and the structure of CND mutants modeled by Pymol software. In blue is presented the hydrophobic side of the helix, while in pink is presented the hydrophilic portion. The red dots are indicating the positive charged amino acids present in the sequence.

5.2 Material and Methods

5.2.1 Peptide synthesis

All the CND mutants (< 95%) were purchased from United Biosystems Inc., USA. Peptide concentrations were estimated by UV/Vis absorption at 280 nm (ε_{280} = 6990 M^{-1} cm^{-1}).

5.2.2 Phospholipid vesicle preparation

LUVs with a diameter of 100 nm were chosen as membrane mimicking system model. These vesicles were prepared as reported in 4.2.2

5.2.3 Steady-state fluorescence experiments

The characterization of CND mutants' behavior in presence of different phospholipid membranes was assessed using steady-state fluorescence spectroscopy experiments. All the experiments were performed using a Perkin Elmer LS55 steady-state fluorescence spectrometer equipped with a thermostatic cell holder with a magnetic stirrer operating at 25°C. A cross-oriented configuration of the polarizers was used to correct the polarization effects and to reduce the direct contributions from vesicle light scattering [68].

5.2.3.1 Outer membrane permeability assay

The ability of the peptides to interact with natural membrane was assessed performing the outer membrane permeability assay on *E. coli* BL21 (DE3), as previously describe (Chapter 4.2.3.1, [8]). Briefly, an LB over-night culture of *E. coli* BL21 (DE3) was grown to a mid-log phase, harvested and resuspended in a buffer of 10 mM Tris-HCl, 150 mM NaCl, 0.8 mM EDTA at pH 7.4, to a

final OD_{600} of ~1.2. ANS (5 µM) was then added to 1.0 mL of cell suspension and allowed to equilibrate at room temperature. Increasing amount of peptide, ranging from 1.0 µM to 15.0 µM, was added to the cell suspension and a fluorescence spectrum was recorded between 400 and 600 nm using an excitation wavelength of 360 nm and excitation/emission band-passes of 5.0. To reduce the fluorescence scattering contribution of cells, each spectra was recorded using a cross-oriented configuration of polarizers (Pol_{em}=0° and Pol_{exc}=90°). The percentage of uptake was calculated according to the following equation:

$$\%\ ANS\ Uptake = \frac{F_{obs} - F_0}{F_0} \times 100 \qquad 5.1]$$

where F_{obs} and F_0 are the observed fluorescence at the given concentration of peptide and the fluorescence in absence of the peptide, respectively.

5.2.3.2 Partition studies

The partition of CND mutants into phospholipid bilayer was studied by monitoring the increase of the Trp fluorescence emission spectrum upon the addition of LUVs. The Trp fluorescence spectrum was recorded between 305 nm and 500 nm, upon excitation at λ_{exc} = 295 nm, with an excitation/emission bandwidth of 5.0 nm. These measurements were carried out with a cross-oriented configuration of polarizers (Pol_{em}=0° and Pol_{exc}=90°). Increasing amount of LUVs of different lipid composition was added to 1.0 µM of peptide in 20 mM phosphate buffer at pH 7.4 with 150 mM NaCl and 0.8 mM EDTA. The peptide-lipid interaction was tested with LUVs of different composition [PC-100%, PC/PG (70:30) and *E. coli* extract] with the lipid/peptide ratio tested

ranged between 50 and 500. The background from both buffer and vesicles was subtracted from each spectrum. The experiments for each CND mutants were repeated in quadruplicate for each LUVs tested. Molar partition coefficients K_x and the fraction of peptide partitioned into the lipid bilayer, f_p, were calculate according to equation 4.1 and 4.2.

5.2.3.3 Iodide quenching experiments

To evaluate the CND mutant interaction with the membrane and the topology of this interaction, studies of fluorescence quenching of Try were performed [153, 154]. These studies were been carried out in absence and presence of vesicles of different lipid composition [PC-100%; PC/PG (70:30), *E.coli*-LUVS], at a peptide/lipid molar ratio of 1:100, ad using potassium iodide (KI) as a quencher. Aliquots of KI stock solution (3.0 M) were added to the appropriate peptide concentration placed in a 1.0 mL quartz cuvette, and the fluorescence spectrum was recorded. The excitation wavelength was set to 295 nm and the florescence spectra were recorded between 305 and 455 nm with a bandpass of 5.0 nm. As in the partition experiments, a cross-oriented configuration of polarizers (Pol_{exc}=0° and Pol_{emi}=90°) was used [9]. All the spectra were corrected for dilution and for the absorption of fluorophores and quenchers. Data obtained were analyzed according to the Stern-Volmer equation as described in Appendix 2.1.

5.2.3.4 Calcein leakage studies

To better understand the ability of CND mutants to perturb the bacterial membrane, the kinetics of calcein release from vesicles of different lipid composition was performed. In this case, the ability of each mutants to induce the calcein leakage from different LUVs [PC-100% and PC/PG (70:30)], loaded with 30 mM of calcein, was assessed using calcein fluorescence. The samples were prepared by adding serial concentrations of peptide, ranging from 0.1-1.0 μM, to four different calcein encapsulated-LUVs concentration [from 12.5 to 100.0 μM]. The increase of calcein fluorescence was monitored at an emission wavelength of 520 nm, an excitation wavelength of 490 nm, with excitation and emission band-passes of 2.5 nm, at a temperature of 25 °C. The kinetics of release was followed for about 2000 s and, before the peptide addition the emission fluorescence of only LUVs was recorded for 5 min (baseline). The normalization of the recorded fluorescence intensity was obtained by the addition of Triton-X detergent that dissolves all the intact vesicles releasing all the encapsulated dyes. Before each measurement, light scattering spectra between 540 nm and 560 nm, using an incident light of 550 nm, were measured to estimate the integrity of vesicles [123]. The[155] percentage of dye release was calculated using equation 4.4. The kinetic description of the dye-release mechanism induced by the peptides was achieve by fitting the data with equation 4.5.

5.3 Results

5.3.1 Outer membrane permeability assay

The outer membrane permeability assay was used to test the CND mutant ability to perturb and disrupt the integrity of *E. coli* BL21 (DE3), which was used as a bacterial cell prototype. ANS is hydrophobic and is able to cross the cell membrane. When ANS is constrained outside the cell, it gives a weak fluorescence signal caused by the high polarity of water. If the outer membrane of bacterial is disrupted by the peptide, then ANS can pass through the bacterial outer membrane and change its chemical environment. This is reflected by an increase of fluorescence and in a blue-shift of the λ_{max} of emission [124] (**Figure 5.2 A-C**). All the peptides, both the wild-type and the mutants, have been shown the capability to perturb the integrity of *E. coli* outer membrane, causing the relocation of ANS to the periplasmic space. As previously observed for wild-type peptide (Chap. 4.3.1), CND mutants have a perturbation that is dose-dependent and is detectable even at low peptide concentrations. **Figure 5.2-D** reports the ANS uptake as a function of peptide concentration. This plot shows that KSH-CND and KH-CND are perform faster membrane permeabilization compared to wild-type CND (WT-CND) and KS-CND. It is important to notice that the outer membrane permeability assay is not a quantitative test, so it cannot establish which mutant has better affinity and disruption activity with respect to bacterial membranes. To answer this question, other experiments need

to be done, like antibacterial activity assays, fluorescence dye leakage, and partitioning studies.

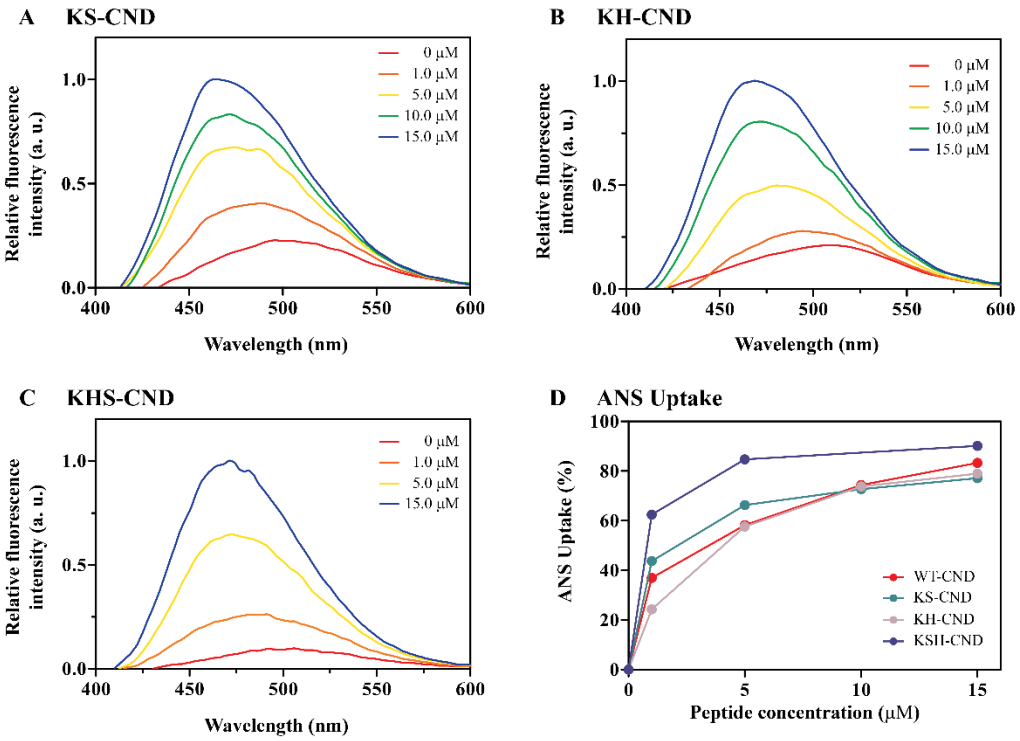

Figure 5.2.Outer membrane permeability assay. Permeabilization of the external membrane of *E.coli* BL21 (DE3) by the three CND mutants (A-C).In panel D is reported the ANS Uptake for the wild-type peptide and the mutants.

5.3.2 Partitioning studies

The quantification and identification of CND mutants' interaction with model membrane was investigated by intrinsic fluorescence partition studies. Briefly, the change of the emission spectrum of the engineered Trp-1 was monitored before and after the addition of LUVs of different lipid composition (**Figure 5.3**) to measure the affinity between the AMP and membrane bilayer. The change in intensity was recorded and fitted to equation 4.3. The binding isotherms (**Figure 5.4**), obtained from the titration of the peptides with increasing amount of LUVs, were used to calculate the mole fraction partition coefficient, K_x, and the Gibbs free energy (ΔG) associated to the partitioning event (**Table 5.2**). The calculated values of K_x shows that both the wild-type and the mutants have a higher propensity to interact with LUVs made by a mixture of neutral and negatively charged phospholipids [PC/PG (70/30)], but the mutants also showed an increased interaction with PC-100% (nuclear head groups) vesicles. Interestingly, the estimated K_x of wild-type CND for *E. coli* membrane extract is higher than the ones calculated for the mutants. This effect can be addressed to the higher complexity of the vesicles made by natural phospholipids, where the lipid composition is not completely characterized. Overall, the obtained results suggest that both the bilayer composition and the peptide charge are important in the partitioning events that occur between membrane bilayer and AMPs.

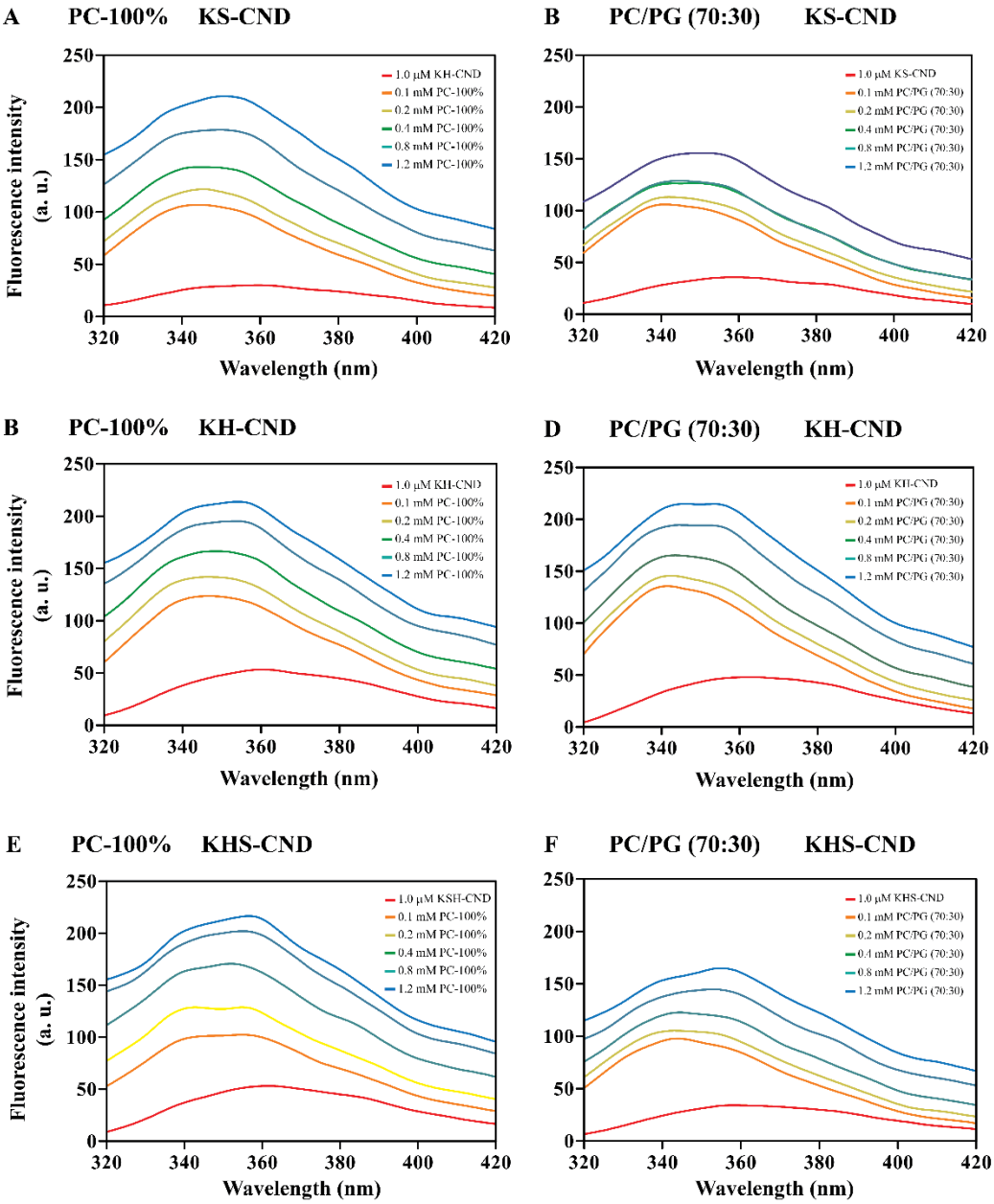

Figure 5.3. Partition experiments. Emission spectra of CND mutants recorded in presence of increasing concentration of (A-C-E) 100% of PC and (B-D-F) a mixture of PC/PG (70:30 molar ratio) LUVs. The I_{max} of each spectra was used to calculate the K_x, according to equation 4.3. The spectra were recorded at 25 °C using 1.0 μM of peptide.

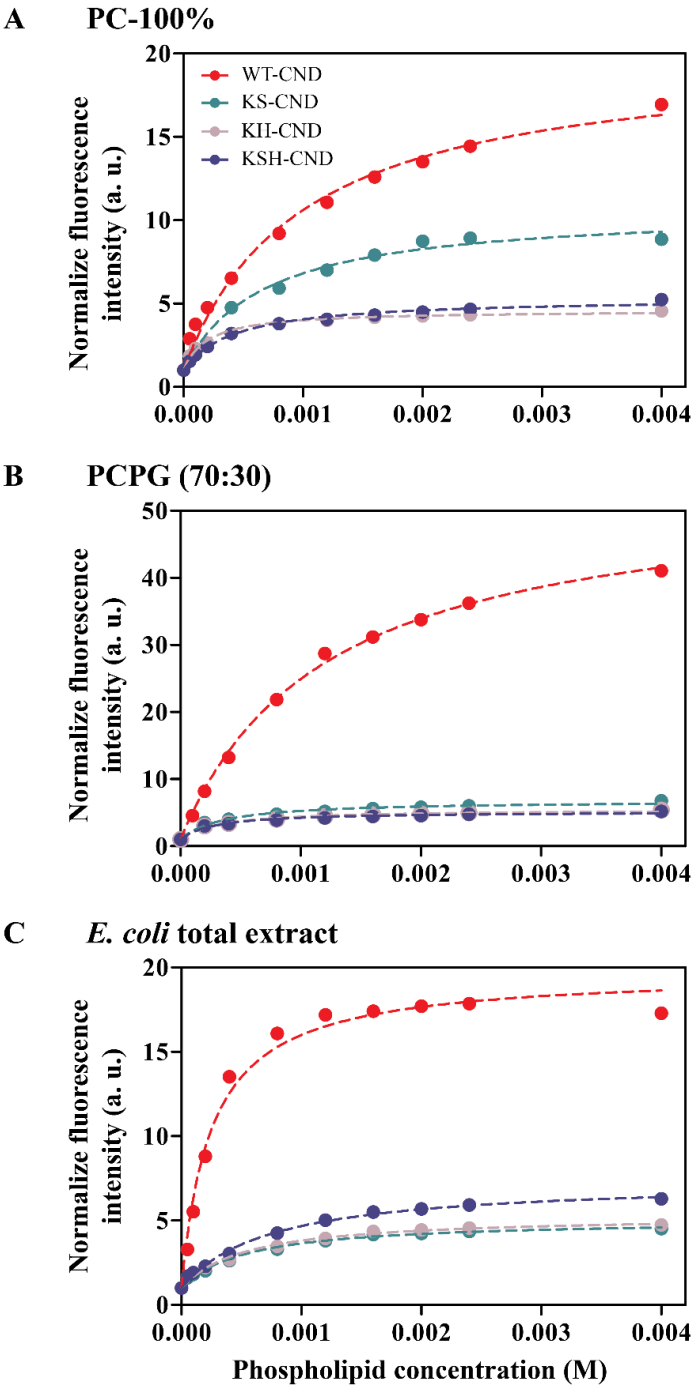

Figure 5.4. Binding isotherms for CND and its mutants interacting with lipid bilayer vesicles. The fluorescence intensity of the Try/Trp residue was measured as LUVs were titrated into the sample. Before registered the spectrum, the system was allowed to equilibrate at least for 10 minutes

Table 5.2. Partition parameters for CND and its mutants calculated from the titration of the peptides (1.0 μM) with LUVs of different phospholipid composition.

Peptide Concentration	Lipid composition	K_x ($\times 10^4$)	ΔG, (kJ/mol)
CND	PC-100%	3.43 ± 0.26	-25.9
	PC/PG (70:30)	4.91 ± 0.29	-26.7
	E.coli total extract	18.32 ± 0.08	-30.0
KS-CND	PC-100%	8.27 ± 0.77	-28.0
	PC/PG (70:30)	23.25 ± 0.66	-30.6
	E.coli total extract	10.22 ± 0.98	28.6
KH-CND	PC-100%	27.62 ± 0.71	-31.0
	PC/PG (70:30)	20.42 ± 0.87	-30.3
	E.coli total extract	10.34 ± 0.31	-28.6
KHS-CND	PC-100%	15.32 ± 0.81	-29.6
	PC/PG (70:30)	16.51 ± 0.97	-29.7
	E.coli total extract	7.46 ± 0.90	-27.8

5.3.3 Intrinsic fluorescence quenching experiments

Studies of Trp fluorescence quenching was used to investigate the topology of the CND mutants on LUV surface. As observed for the wild-type CND, in solution the engineered Trp is accessible to the quencher and a decrease of the fluorescence emission spectra is observed with respect to increased quencher (spectra not reported). In presence of phospholipid membrane, the quenching phenomenon is still observed, but the effect is less prominent when compared to the quenching in solution. This result indicates that the fluorophore (Trp-1 in CND) has a different accessibility of the quencher when LUVs are present. **Figure 5.5 and 5.6** reports the Trp quenching profiles and the Stern-Volmer plots for the three mutants in presence of the three different lipid compositions of tested vesicles. In all the mutants linearity in the Stern-Volmer plots is observed, suggesting that CND is in presence of collisional quenching. The smaller K_{SV} values obtained for the peptides in presence of LUVs is a further indication of the interaction between peptides and lipid surface (**Table 5.3**). In the presence of membrane, Trp-1 is less accessible to the quencher because the N-terminal portion is strongly involves in this binding process to the lipid bilayer, as observed for the wild-type. Also, for both the mutants and wild-type CND, lower values of K_{SV} were calculated in presence of PC/PG (70:30) and *E. coli* total lipid extract LUVs. These results suggest that the presence of negatively charged phospholipid on the LUV surface increases the inaccessibility to the quencher, hence increases the partition of the peptides onto the lipid bilayer with respect to solution.

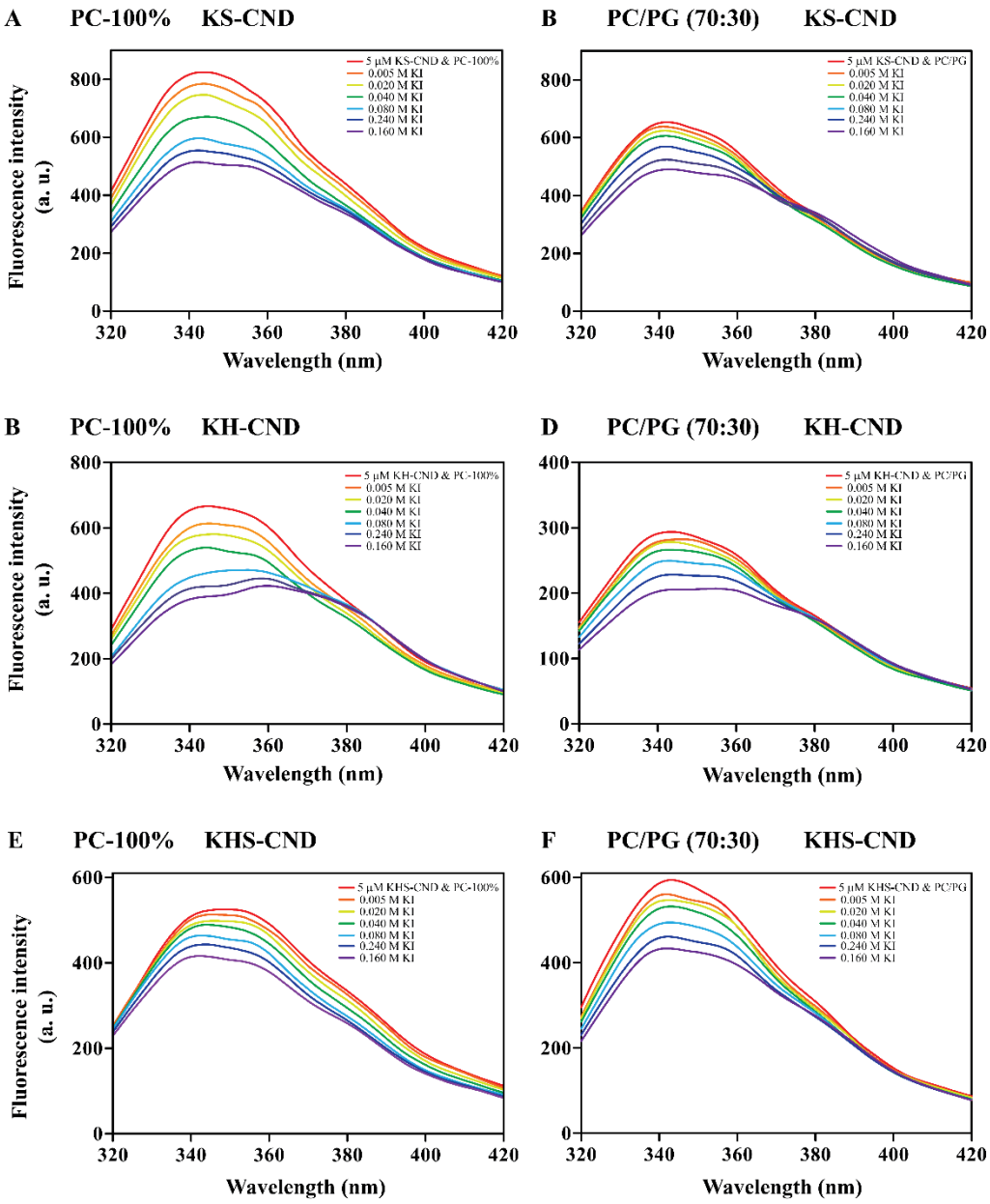

Figure 5.7. CND mutants cause efficient calcein release from vesicles. Kinetics of calcein release from 25 μM PC-100% (A-C-E) and PC/PG (70:30) (B-D-F) LUVs, upon the addition of increasing amount of mutants. The LUVs were loaded with 30 mM of calcein. All the experiments were performed at 25 °C. Each curve is normalized by Triton-X.

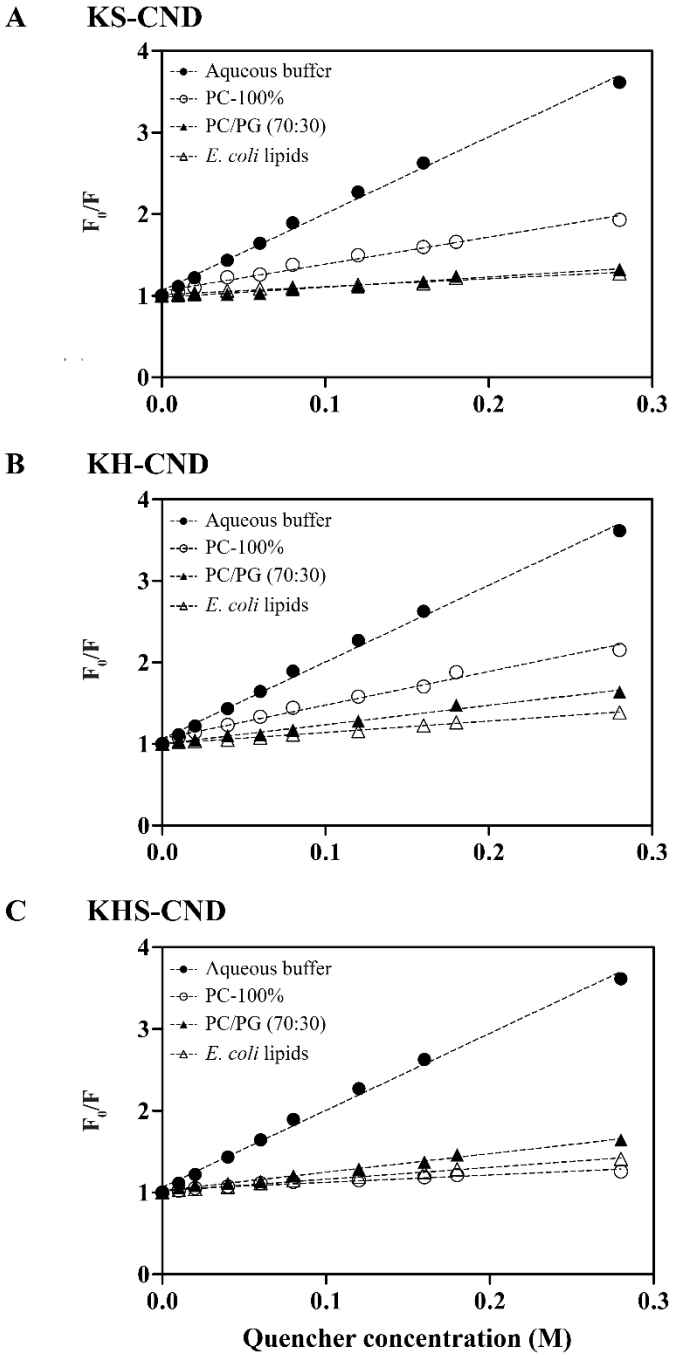

Figure 5.6. Stern-Volmer plots for the quenching of Trp residue of CND by Iodide. For each mutants, the quenching experiments were performed in buffer and in presence of 0.5 mM of PC-100%, PC/PC (70:30) and *E. coli* total extract LUVs. The final concentration of peptides was 5 90–M.

Table 5.3. Stern-Volmer quenching constant (K_{SV}) and percentage of I^- quenching for CND and the derived mutants, in the presence of vesicles of different lipid composition. The peptide/lipid molar ratio was 1:100 in all the case.

Peptide Concentration	Lipid composition	K_{SV} (M^{-1})	$1/K_{SV}$ (M)	Percentage of quenching
CND	Aqueous buffer	10.4 ± 0.2	0.10	100.0
	PC-100%	2.9 ± 01	0.34	28.4
	PC/PG (70:30)	2.5 ± 01	0.41	23.6
	E.coli total extract	1.6 ± 0.2	0.63	15.4
KS-CND	Aqueous buffer	10.2 ± 0.3	0.01	100.0
	PC-100%	3.3 ± 0.2	0.30	32.6
	PC/PG (70:30)	2.0 ± 0.1	0.50	22.1
	E.coli total extract	1.0 ± 0.1	1.00	12.8
KH-CND	Aqueous buffer	10.8 ± 0.4	0.09	100.0
	PC-100%	4.0 ± 0.2	0.25	42.4
	PC/PG (70:30)	2.3 ± 0.1	0.43	24.1
	E.coli total extract	1.4 ± 0.1	0.71	12.6
KHS-CND	Aqueous buffer	12.3 ± 0.2	0.10	100.0
	PC-100%	1.5 ± 0.1	0.68	14.8
	PC/PG (70:30)	2.1 ± 0.1	0.48	17.9
	E.coli total extract	1.4 ± 0.1	0.71	14.8

5.3.4 Calcein leakage studies

The calcein efflux from loaded-LUVs was used to assess the membrane permeabilization ability of CND mutants. **Figure 5.7** reports the fluorescence profile of the calcein release from 25 μM of LUVs, made of 100% PC and a mixture of PC/PG (70:30 molar ratio) lipids after increasing addition of peptide. The percentage of calcein release was calculated using equation 4.4 and the values are reported in **Table 5.4.** The calcein efflux profiles were also analyzed using a method developed by Tatulian and coworkers [123] that allows the calculation of the kinetics parameters (**Table 5.5**). The data shows that all the CND mutants have the capability to interact and disrupt different model membranes, causing the release of dye. However, all the mutants, compared to wild-type CND, were able to induce calcein release from tested LUVs in a more effective manner, especially with negatively charged membranes. In fact, higher relative leakage capabilities were recorded with PC/PG (70:30) LUVs, at low peptid/lipid molar ratio for all mutants. These results give a further confirms of the importance of the presence of both negatively charge phospholipid on the membrane surface and the positive charged amino acid in the peptide sequence. The presence of charged lipids also influences the kinetics of calcein release. Usually, the kinetic parameters of calcein efflux recorded for PC/PG LUVs are indicative of a process that occurs faster than when performed in PC-100% LUVs.

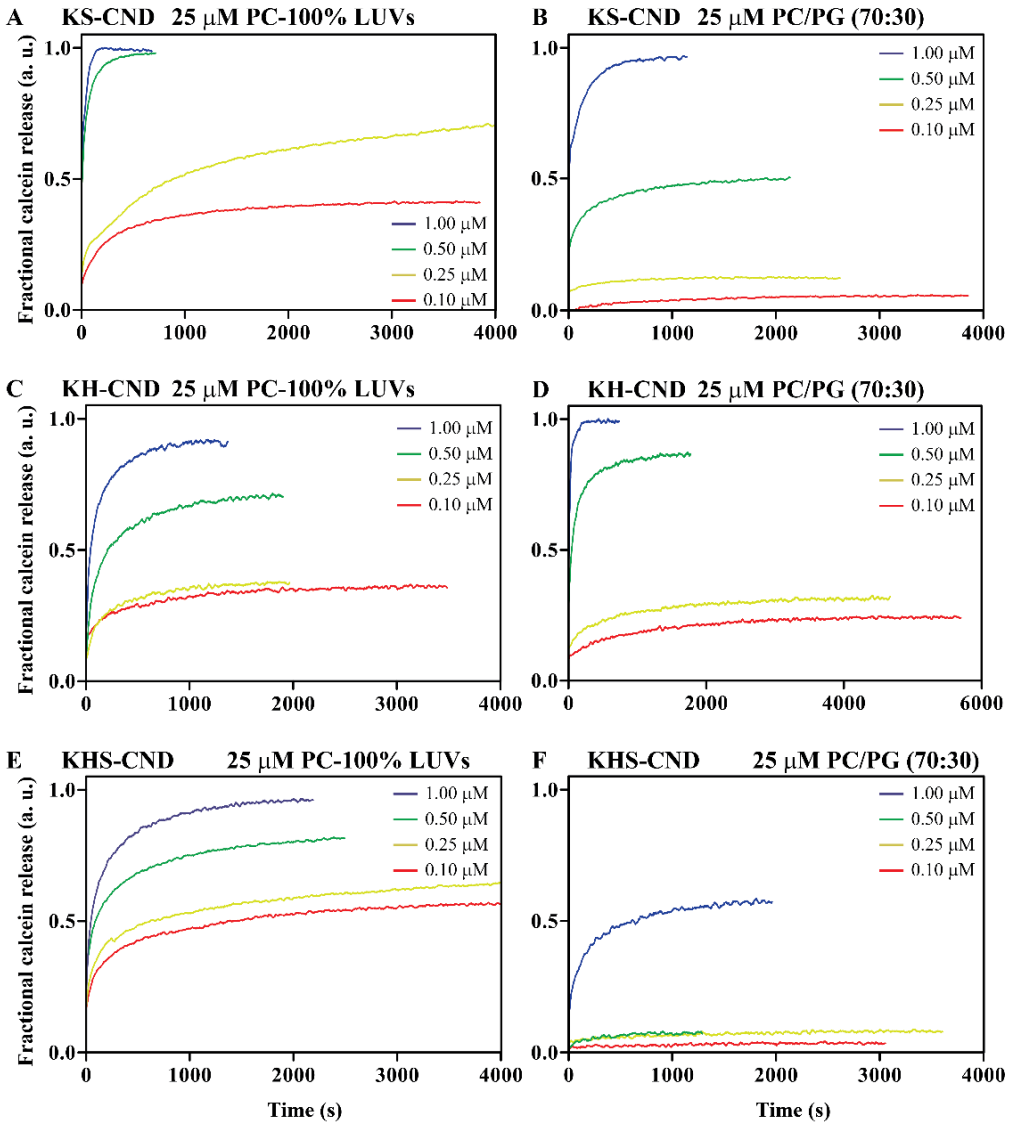

Figure 5.7. CND mutants cause efficient calcein release from vesicles. Kinetics of calcein release from 25 μM PC-100% (A-C-E) and PC/PG (70:30) (B-D-F) LUVs, upon the addition of increasing amount of mutants. The LUVs were loaded with 30 mM of calcein. All the experiments were performed at 25 °C. Each curve is normalized by Triton-X.

TABLE 5.4 Relative leakage capabilities of CND and its mutant in presence of LUVs of different lipid composition and at different peptide/lipid molar ratio.

Peptide/lipid (molar ratio)	PC-100%				PC/PG (70;30)			
	CND	KS-CND	KH-CND	KHS-CND	CND	KS-CND	KH-CND	KHS-CND
1/12.5	99.4	99.5	99.9	99.6	99.5	99.99	100.0	98.1
1/25	63.0	99.1	95.5	96.2	95.2	94.1	99.3	90.8
1/50	23.0	97.6	86.2	86.1	85.6	37.2	63.9	28.6
1/100	16.7	88.8	63.0	76.1	50.7	16.0	23.0	

TABLE 5.5 Kinetic parameters for calcein release from 25 μM LUVs of different lipid composition upon addition of increasing amount of CND mutants. The parameters derived from the data fitting showed in figure 5.7.

KS-CND

[P]	F_{eq}		a_1		a_2		k_1 (s^{-1})		k_2 (s^{-1})	
(μM)	PC	PC/PG	PC	PC/PG	PC	PC/PG	PC	PC/PG	PC	PC/PG
0.10	0.414	0.161	0.165	0.099	0.151	0.024	0.00107	0.00039	0.0064	0.0321
0.25	0.931	0.125	0.667	0.046	0.081	0.010	0.00160	0.00261	0.0018	0.0195
0.50	0.976	0.506	0.281	0154	0.285	0.125	0.00820	0.00160	0.0367	0.0124
1.00	0.995	0.961	0.437	0388	0.023	0.146	0.02223	0.00604	0.0223	0.1510

KH-CND

[P]	F_{eq}		a_1		a_2		k_1 (s^{-1})		k_2 (s^{-1})	
(μM)	PC	PC/PG	PC	PC/PG	PC	PC/PG	PC	PC/PG	PC	PC/PG
0.10	0.495	0.246	0.223	0.124	0.192	0.037	0.00106	0.00071	0.0061	0.0053
0.25	0.860	0.318	0.245	0.124	0.409	0.071	0.00228	0.00078	0.0113	0.0057
0.50	0.991	0.867	0.176	0.212	0.151	0.393	0.02369	0.00242	0.0892	0.0160
1.00	0.914	0.993	0.370	0.170	0.390	0.556	0.00385	0.01200	0.0305	0.0571

KHS-CND

[P]	F_{eq}		a_1		a_2		k_1 (s^{-1})		k_2 (s^{-1})	
(μM)	PC	PC/PG	PC	PC/PG	PC	PC/PG	PC	PC/PG	PC	PC/PG
0.10	0.578		0.221		0.178		0.00074		0.0092	
0.25	0.667	0.309	0.238	0.180	0.221	0.072	0.00056	0.00096	0.0086	0.0094
0.50	0.820	0.915	0.283	0.190	0.241	0.362	0.00140	0.00457	0.0133	0.0308
1.00	0.962	0.995	0350	0.699	0.368	0.208	0.00204	0.00783	0.0182	0.1041

5.4 Discussion and conclusion

In the last few decades, the extensive use of antibiotics has caused the increase of pathogenic resistance against conventional antibiotics [23]. Currently research is focused on the discovery or development of new chemical or natural agents that can act as antibiotics substitutes. AMPs are a principal candidate for new anti-microbial discovery [156]. AMPs are a component of the innate immune system of eukaryotic organisms and also produced by fungi and bacteria, as a protection against pathogen infections [23, 29]. In eukaryotic organisms, different AMPs are produced, stored inside the secondary granules of granulocyte and macrophage cells, and released when a bacterial infection is present [157]. In this way, a localized release of different AMPs, that work synergically to kill the bacterial pathogen, act as modulators of the innate immune system response [44]. In most instances, natural AMPs do not appear to be highly optimized for direct antimicrobial activity [158], even if neutrophils, monocytes and macrophages of various mammalian species contain among the most potent antimicrobial peptides known (defensins) [159, 160]. This lack of activity and specificity of natural AMPs may be overcome by designing new antimicrobial peptides with enhanced activity and interaction against pathogens. Three different approaches have been used to design AMP mutants. The traditional approach consists of designing of mutant sequences using a natural AMP sequence as a template. Usually the mutations are designed to increase the positive charge and the hydrophobicity of the new sequence. This approach is based

on experimental evidence that the presence of positively charged and hydrophobic amino acids is an essential characteristic that nearly every natural AMP shows. Alternately, the mutant can be designed taking in consideration previous studies of molecular modeling based on free energy perturbations, molecular dynamic simulations, and thermodynamic calculations of the interaction of the AMPs with lipid bilayers. Unfortunately, this method is limited because of variation in computational models (ref). In the last few years, another approach, based on virtual screen studies, was also use to create *de novo* AMP sequences. This method relies on the use of informatics and mathematic algorithms to estimate or predict the desired biological activity from the primary amino acid sequence alone. This is a useful alternative to the traditional method that requires, sometime, exhaustive synthesis and testing of the mutants [156].

In the immune system of the gills of the Antarctic teleost *Chionodraco hamatus*, an antimicrobial peptide called *Chionodracine* was isolated (ref Buonocore). Preliminary characterization showed that the peptide belongs to the piscidin family of AMPs (**Figure 4.1**). This antimicrobial peptide was active against non-pathological strains of human bacterial pathogens. Further investigations, performed using fluorescence and NMR spectroscopy, pointed out the ability of the peptide to interact and disrupt the integrity of biological and synthetic negatively charged membrane. These studies qualified CND as a promising AMP. Using the traditional approach of mutant design, three different peptides were designed to improve the membrane interaction and perturbation ability of wild-type CND (**Table 5.1**). Several mutations were inserted in the prima-

ry sequence to obtain three distinct mutants in which, both the net positive charge and the hydrophobicity were increased (KS-CND and KHS-CND), or only the net positive charge was increased (KH-CND). Characterization of antimicrobial activity of CND mutants was achieved using antimicrobial activity assays (data not reported) and steady-state fluorescence spectroscopy. In particular, CND mutants demonstrated the ability to permeabilize the outer membrane of bacterial cells (*E. coli*), causing the relocation of ANS, a fluorescence dye, from the external environment to the periplasmic space. As observed for WT-CND, the perturbation effects performed by the mutants were detectable even at low peptide concentration (**Figure 5.2**). However, the permeabilization process occurs faster for the mutants, suggesting that the increased positive charge helps peptide/lipid interaction (**Figure 5.2-D**). Calcein release from loaded-LUVs of different lipid composition was used to further investigate the permeabilization ability. These studies showed that CND mutants were able to induce calcein release from tested LUVs, but they were more effective against negatively charged LUVs (even at low peptide/lipid molar ratio) (**Figure 5.7; Table 5.4**). The kinetic parameters derived from the experimental curves (**Table 5.5**) revealed that the calcein release from the PC/PG (negatively charged) vesicles occurred faster than with the PC-100% LUVs (neutral). Furthermore, the mutants induced more rapid calcein release from tested LUVs as compared to WT-CND. Evidence that increased net positive charge improves the perturbation and binding ability of CND was also confirmed by fluorescence partition studies, which was used to investigate the interaction between the mutants and synthetic phos-

pholipid bilayer that mimicked the lipid composition of eukaryotic (PC-100%) and prokaryotic (PC/PG and *E.coli* total lipid extract) membranes (**Figure 5.3**). The mutants, as showed also for wild-type, interacted strongly with LUVs that contained negatively charge phospholipids (**Figure 5.4**). In presence of phospholipid bilayers, the mutant peptides strongly partitioned onto the membrane surface. In this process of membrane association, the N-terminal region of CND (where the intrinsic fluorescence probe is located, Trp-1) is deeply involved with the interaction with phospholipids. The experiments of Trp fluorescence quenching performed on the mutants, using iodide (I^-) as a quencher, showed that, in presence LUVs, the Trp residue of all the peptides are not easily inaccessible to I^- (K_{SV} value is almost equal to 1) (**Figure 5-6; Table 5.3**) in the presence of phospholipid bilayers. The important role of the N-terminus of CND sequence was previously demonstrated both with quenching experiment and solving the NMR structure of the wild-type peptide. The data obtained for CND mutants confirmed that this portion is deeply involved in the peptide/lipid interaction.

All the studies performed on CND mutants demonstrated that the mutations have not only increased the antimicrobial properties of the peptides, but also their ability to interact with phospholipid bilayer. We have demonstrated that rational design of existing AMP constructs by modifying the net positive charge and moment of hydrophobicity we can engineer improved activity. Future studies of CND will probe what the limits of chemical biological engineering of the sequence can yield in terms of anti-microbial activity. We anticipate that a mix-

ture of optimal charge and hydrophobicity, combined with techniques to promote the α-helical conformation which interacts with the membrane, will yield a template that will eventually be clinically relevant.

Chapter 6

Conformational landscape of protein kinase A inhibitor PKI studied by NMR Spectroscopy

The cAMP-dependent protein kinase A (cAPK or PKA) is a ubiquitous phosphoryl transferase that participates in numerous cellular signaling pathway [161-165]. Inside the cell, the activity and localization of PKA-C are finely regulated by endogenous inhibitor proteins, such as the regulatory subunits (R) and the heat-stable protein kinase A inhibitor (PKI) [26, 161, 166, 167]. Both these proteins are structurally very dynamic with major regions of disorder, globular domains and/or well-defined secondary structures (**Figure 3.6**). While R subunits are primarily responsible for regulation and localization of PKA-C in cytoplasm through interaction with A kinase anchoring protein (AKAPs) [26, 168], PKI plays a key role in the nuclear regulation and cytoplasmic translocation of the enzyme [169-172]. Even if R subunit and PKI share some features, like the high affinity inhibitory sequence for PKA-C, they are functionally different and non-redundant.

PKI is a fully unfolded polypeptide and, like other IDPs, does not assume a well-defined 3D structure in solution [173]. Two distinct functional elements can be identified in the PKI sequence: the PKA-C pseudo-substrate recognition sequence (PSS) at the N-terminus (residues 15-22); and a leucine-rich nuclear

export sequence (NES) (residue 37-46) (**Figure 6.1**). The first is responsible for its inhibitory activity, while the NES mediate the translocation of PKI:PKA-C complex from the nucleus to the cytoplasm, through CRM1-Ran/RasGTPase nuclear export complex [171, 174]. There are several X-ray structures of the PKA holoenzyme, that have elucidated the interaction between R and C subunits [175-177], but there is no structural model of the interaction between PKA-C and the full-length of PKI. Numerous studies, which have investigated both the both the kinetics and structural rearrangements of PKA-C upon binding to PKI, have used the truncated forms of PKI [26, 178], such as PKI_{5-24} [179] or PKI_{5-22}[180]. These "short-forms" contain the PSS sequence so they can still bind and inhibit PKA-C, but with similar affinity with the full length protein [181-183]. Hauer and coworkers have analyzed the structure of full-length PKI using 2D NMR spectroscopy [173]. According to this work, PKI contains two regions characteristic of α-helices. The first ordered region is localized within residues 1-13, at the N-terminus and the second well-defined secondary structure extends between residues 35 to 47, and overlaps with the NES. The remainder of the protein appears relatively unstructured in solution [173]. The authors reported to have encountered several problems toward full structure determination, such as several overlapping of proton resonances and lack of medium- and long- range NOEs [114, 116, 184]. This was partially compensated by solving the 3D structure of the two functionally separate PKI fragments [173].

To understand the molecular mechanism underlying recognition of PKA-C by PKI, we characterized the change in the conformational landscape of PKIα

[178, 185-187] upon binding PKA-C (Apo to PKA-C bound). These studies were carried out using solution NMR spectroscopy, the only structural technique to provide atomic resolution detail on IDPs. Chemical shift analysis and nuclear spin relaxation experiments on PKI alone demonstrate that PKI has minimal secondary structural elements with only two transient helices, at the N-terminus and in the NES region, as previously reported by Haeur *et al.* [173]. Paramagnetic relaxation enhancement (PRE) experiments shows that PKI is not fully disordered in solution, but has transient intramolecular interaction between the C- and N-terminus. When a ternary complex between PKA-C, PKI and a non-hydrolysable ATP mimic (ATPγN) is formed, only the portion of the peptide that directly interacts with the PKA-C undergoes significant structural rearrangement, while the majority of the peptide is still unfolded. However chemical shift analysis and nuclear spin relaxation studies indicate that binding to PKA-C confers allosteric changes toward the NES region, suggestive of an increased propensity of α-helical character. These studies elucidate the structural and allosteric basis of full-length PKI, but also represent the basis for further investigation on the structural role of the PKA-C:PKI interaction with respect toward regulation and nuclear export.

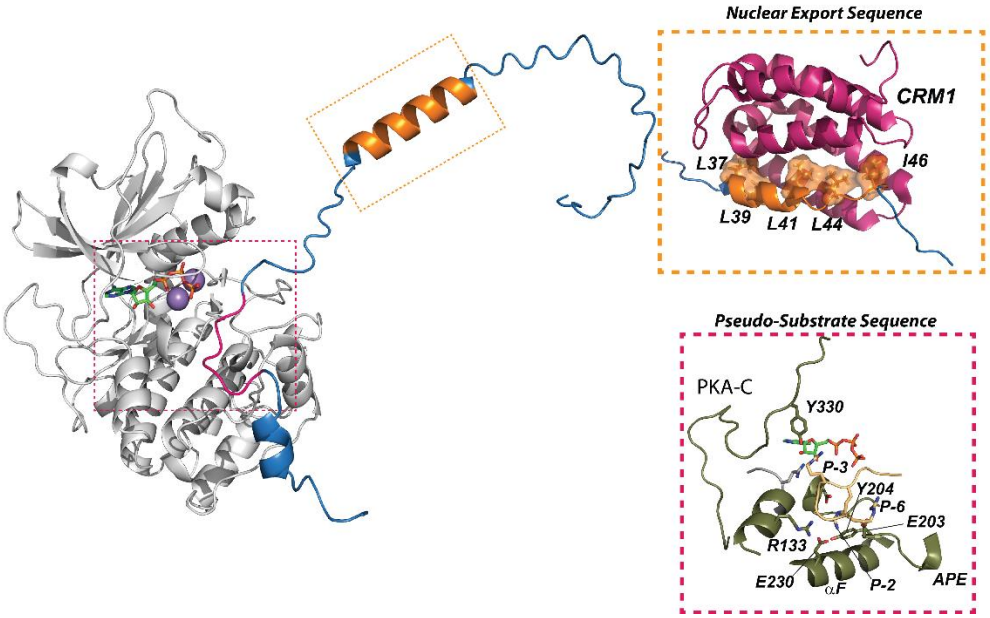

Figure 6.1. Simulated structure of the full-length PKI bound to PKA-C. Full-length PKI sequence is docked in the structure of PKA-C (PDB-1ATP). In the two boxes are reported the crystal of truncated PKI peptides bound to CRM1 (top, PDB-3GJX) PDB ant to PKA-C (bottom, PDB-1ATP), respectively.

6.1 Materials and methods

6.1.1 Sample preparation

6.1.1.1 Expression and purification of recombinant PKA-C

Recombinant catalytic subunit of PKA-C was expressed in *E. coli* BL21 (DE3) cells as previously described by Masterson *et al.* [188, 189] at 24°C in M9 minimal medium. The purification was performed using the His6-RIIa(R213K) subunit as described previously[190]. A subsequent second purification step was performed using a HiTrap SP cation exchange column to separate out the three isoforms of PKA-C that differ in their phosphorylation profiles[191]. A linear gradient from 0 to 1 M KCl was used to separate out the PKA-C isoforms. After the purification, a final concentration of 10 mM DTT, 10 mM $MgCl_2$, and 1.0 mM NaN_3 was added to the solution containing the protein and stored at 4 °C. Expression of PKA-C was performed using shaker flasks, with the exception of ^2H labeled protein, where a bench fermenter (2.0 L) was used. The most abundant isoform of PKA-C, corresponding to phosphorylation at S338, T197, and S10 residues (isoform II) [181], was used for all experiments. The purity was assessed using SDS-PAGE electrophoresis and the final purity was >97%. The kinase activity was tested with a gel-shift assay from Promega (Fitchburg, Wisconsin) and quantified using A_{280} = 52,060 M^{-1} cm^{-1}.

6.1.1.2 Expression and purification of recombinant PKIα

Recombinant full-length PKIα (PKI) was expressed in *E. coli* BL21 (DE3) cells at 30 °C and the purification was performed as previously reported [192]. The *E. coli* cells were re-suspended in lysis buffer (20 mM MOPS at pH 7.0) and the cells were disrupted using French press. The cellular suspension was then centrifuged at 20000 rpm for 30 min. The supernatant was heated for 5 minutes at 95 ˚C and centrifuged at 20000 rpm for 30 min. The resultant supernatant was dialyzed overnight in 20 mM TrisHCl at pH 7.0. A second purification step was performed using a HiTrap Q HP anionic exchange column using a linear gradient from 0 to 1M of NaCl in 20 mM TrisHCl (at pH 7.0). The final purification was performed using C18 Vydac HPLC column. The purified peptide was concentrated, lyophilized, and stored at room temperature under a desiccator. Uniformly labed ^{15}N, 15/13C and ^{2}H/^{13}C/^{15}N PKI was expressed in M9 media and purified identically. The final product was accessed using SDS-PAGE with a final purity of >97%. The molecular weight and the quantity of the peptide were verified by amino acid analysis (Protein chemistry laboratory at Texas A&M University, TX, USA). All cysteine mutants of PKIα (V3C, S28C, and S59C) were produced using the QuikChange Site-Directed Mutagenesis Kit (Agilent Technologies) and purified identically to that of the wild-type PKIα.

6.1.2 NMR experiments

6.1.2.1 Sample preparation

Samples for the free form of PKIα were performed using uniformly ^{15}N and $^{15}N/^{13}C$ labeled protein expressed in M9 media. The final concentration of samples for NMR experiments was 0.5-0.8 mM in 20 mM KH_2PO_4, 90 mM KCl, 10 mM DTT, 10 mM $MgCl_2$, 1 mM NaN_3 at pH 6.5. Samples for the assignment of the PKIα in complex with PKA-C were performed using uniformly $^{2}H/^{13}C/^{15}N$ labeled PKIα and uniformly $^{2}H/^{15}N$ PKA-C. The ternary complex between PKI and PKA-C was formed in 20 mM KH_2PO_4, 90 mM KCl, 12 mM of ATPγN (in the specific case AMP-PNP), 10 mM DTT, 10 mM $MgCl_2$, 1 mM NaN_3 at pH 6.5. A molar ratio of 1:1.2 (PKI:PKA-C) to saturate the complex with a concentration of 0.25 mM of PKIα. All experiments were performed at 27°C.

6.1.2.2 Assignment of PKIα free

The NMR spectra were acquired on a Varian Inova 600 MHz spectrometer equipped with a HCN Cold Probe. Backbone resonance assignment of PKI in free and bound form to PKA-C was performed using standard triple-resonance 3D NMR experiments [193, 194]. The ^{1}H-^{15}N HSQC [131] experiments were acquired with 16 scans, 2048 (proton) and 100 (nitrogen) complex points, before and after each triple-resonance experiments. The HNCACB [195] and CBCA(CO)NH [195] experiments were collected with 64 scans, 1643 (proton), 108 (nitrogen), and 128 (carbon) complex points. The HNCO [194, 196] experiments was acquired with 32 scans, 2048 (proton), 80 (nitrogen), and 108 (car-

bon) complex points. Standard ^{15}N edited TOCSY-HSQC and NOESY-HSQC [197] experiments were acquired with 64 scans, 2048 (proton) and 240 (nitrogen) complex points. The CC(CO)NH-TOCSY [198] experiment was recorded with 2048 (proton), 60 (nitrogen), and 160 (carbon) complex points, with 32 scans on a Bruker 700 MHz Advance III spectrometer equipped with a 1.7 mm TCI MicroCryoProbe. All data was processed using NMRPipe [42], and visualized using Sparky [43].

6.1.2.3 Assignment of PKIα bound to PKA-C

All experiments for the backbone assignment of the PKI:PKA-C:AMP-PNP complex were performed on a Bruker Advance III 850 MHz spectrometer with a TCI cyro-probe. The spectra assignment for the ternary complex between PKI:PKA-C:AMP-PNP were used the reported experiments. The TROSY-based [199, 200] HNCA and HN(CO)CA [193] experiments were collected with a minimum of 32 scans, 2048 (proton), 64 (nitrogen), and 128 (carbon) complex points. The TROSY-based HNCACB experiment was collected with 32 scans, 2048 (proton), 70 (nitrogen) and 100 (carbon) complex points were performed to measure the ^{13}Cα and ^{13}Cβ correlations. The HNCO experiments was acquired with a minimum of 16 scans, 2048 (proton), 60 (nitrogen), and 80 (carbon) complex points. Before and after each triple resonance experiments a ^{1}H-^{15}N CLEAN-TROSY [201]-HSQC spectrum was acquired with 2048 (proton) and a minimum of 128 (nitrogen) complex points. All data was processed using NMRPipe [133], and visualized using Sparky [134].

6.1.2.4 Chemical shift analysis

The Chemical Shift Index (CSI) for Cα, Cβ, C' and Hα, were calculated with respect to the reference calculated by Schwarzinger *et al.* [202, 203] and plotted using the GraphPad Prism 6 software package (GraphPad Software Inc.). The combined Chemical Shift Perturbation (CSP) plot [204] was calculated using amide ^{1}H (HN) and ^{15}N chemical shifts according the following equation:

$$\Delta\delta = \sqrt{\Delta\delta_{HN}^2 + 0.154 \cdot \Delta\delta_N^2} \qquad [6.1]$$

Where $\Delta\delta$ is the compounded chemical shift perturbation $\Delta\delta_{HN}$ is the chemical shift perturbation of the proton and $\Delta\delta_N$ is the perturbation of the nitrogen chemical shift.

6.1.2.5 NMR relaxation experiments

The heteronuclear [^{1}H-^{15}N] NOE spectra were acquired using standard pulse sequences [205] on a Bruker Advance III spectrometer operating at 900 and 850 MHz equipped with TCI cryoprobes at 27 °C. Experiments on the free form of PKIα was performed using a 0.2 mM sample of uniformly ^{15}N labeled PKA-C and experiments of PKIa in a ternary complex with PKA-C and AMP-PNP were made with 0.25 mM of uniformly $^{2}H/^{15}N$ labeled PKIα and 0.35 mM of uniformly ^{2}H labeled PKA-C. All samples were prepared in aqueous buffer consisting of 20 mM KH_2PO_4, 90 mM KCl, 10 mM $MgCl_2$, 10 mM DTT, 1 mM NaN_3 at pH 6.5. Experiments with PKA-C apo form were carried out in the presence of 12 mM of AMP-PNP. The heteronuclear NOE values were calculated from the ratio of the peak intensities with and without proton saturation.

The errors were estimated by evaluating the standard deviation of the NOE values (σ_{NOE}):

$$\frac{\sigma_{NOE}}{NOE} = \sqrt{\left(\frac{\sigma I_{sat}}{I_{sat}}\right)^2 + \left(\frac{\sigma I_{unsat}}{I_{unsat}}\right)^2} \qquad [6.2]$$

where σI_{sat} and σI_{unsat} is the root mean square noise of the spectra and I_{sat} and I_{unsat} are the intensities of the resonance with and without proton saturation [205].

6.1.2.6 Paramagnetic relaxation enhancement

Approximately 0.60 mg of the uniformly ^{15}N labeled cysteine mutant of PKIα (V3C, S59C, S28C) was initially dissolved in a buffer containing 20 mM KH_2PO_4, 90 mM KCl, 10 mM $MgCl_2$, 1 mM NaN_3 at pH 7.5. A tenfold excess of S-(1-oxyl-2,2,5,5-tetramethyl-2,5-dihydro-1H-pyrrol-3-yl)methyl methanesulfonothioate (MTSL) was added to the solution. The samples were incubated for 1.5 hours and protected from light at 4°C. After the reaction the excess MTSL was then removed by dia-filtration. The extent of labeling was assessed by ESI TOF mass spectrometry (Mass Spectrometry Laboratory, University of Minnesota: Department of Chemistry) and was found to be >99%.

The ^1H PRE-Γ_2 relaxation measurements were carried out using the pulse sequence by Iwahara *et al.*[206] on a Bruker Advance 700 MHz spectrometer at 27°C. All experiments were performed using 160 scans with 2048 (proton) and 128 (nitrogen) complex points. A two time point measurement was performed using a relaxation duration of 4 and 14 ms in an interleaved fashion. The spin

label was subsequently reduced by the addition of 10-fold excess of ascorbic acid, and then the experiment was repeated identically. The ^{1}H PRE-Γ_2 were calculated using the equation[206]:

$$\Gamma_2 = \frac{1}{T_b - T_a} \ln \frac{I_{dia}(T_b) I_{para}(T_a)}{I_{dia}(T_a) I_{pata}(T_b)} \quad [6.3]$$

where Γ_2 is the PRE relaxation rate, the time points are T_a and T_b, I_{para} is the corresponding intensity with a spin label and I_{dia} is the corresponding intensity with a reduced spin label:

$$\sigma(\Gamma_2) = \frac{1}{T_b - T_a} \sqrt{\left\{\frac{\sigma_{dia}(T_a)}{I_{dia}(T_a)}\right\}^2 + \left\{\frac{\sigma_{dia}(T_b)}{I_{dia}(T_b)}\right\}^2 + \left\{\frac{\sigma_{para}(T_a)}{I_{para}(T_a)}\right\}^2 + \left\{\frac{\sigma_{para}(T_b)}{I_{para}(T_b)}\right\}^2} \quad [6.4]$$

where σ_{dia} and σ_{para} are the root mean square noise of the respective spectra.

6.2 Results

6.2.1 Assignment and secondary structure of PKIα

To determine the structure and spectral properties of PKα, we obtained the ^{1}H-^{15}N HSQC spectra of this protein in solution. Each resonance on a ^{1}H-^{15}N HSQC represents the chemical environment of each amino acid in the protein. As a result the ^{1}H-^{15}N HSQC pattern is often called the "fingerprint" of the protein, indicating the structure and dynamic state of the system. Figure 6.2 reports the HSQC spetrum of uniformly $^{2}H/^{13}C/^{15}N$ labeled PKIα alone (**Figure 6.2-A**). As for the majority of IDPs [96, 115, 207], the HSQC spectrum of PKIα does not show a good dispersion of the resonances in the ^{1}H dimension, suggesting that the peptide lacks a tertiary structure in solution. Standard triple resonance experiments were used to assign the backbone amides of PKA-C and a total of 74 out of 75 residues.

The secondary structure propensity of the backbone was performed using the CSI ($^{13}C\alpha$, $^{13}C\beta$, ^{13}CO, and $^{1}H\alpha$). The the CSI calculated for the PKIα alone is reported in **Figure 6.3-A**, showing regions of the peptide with a distinct propensity to form α-helical secondary structures. The first helix is localized at the N-terminus, just prior to the PSS sequence (residue 3-12), while the second helix includes the NES. The existence of these helices is supported by steady-state NOE experiments (**Figure 6.3-B**). The increase in the steady-state NOE values are indicative of the CSI trends, suggesting that other than the two helices, the protein remains unstructured. As reported by the Hauer et al.[173],

it was not possible to identify medium- and long-range NOEs in the NOESY-HSQC spectrum, indicating that the two α-helical secondary structures exist as nascent helices.

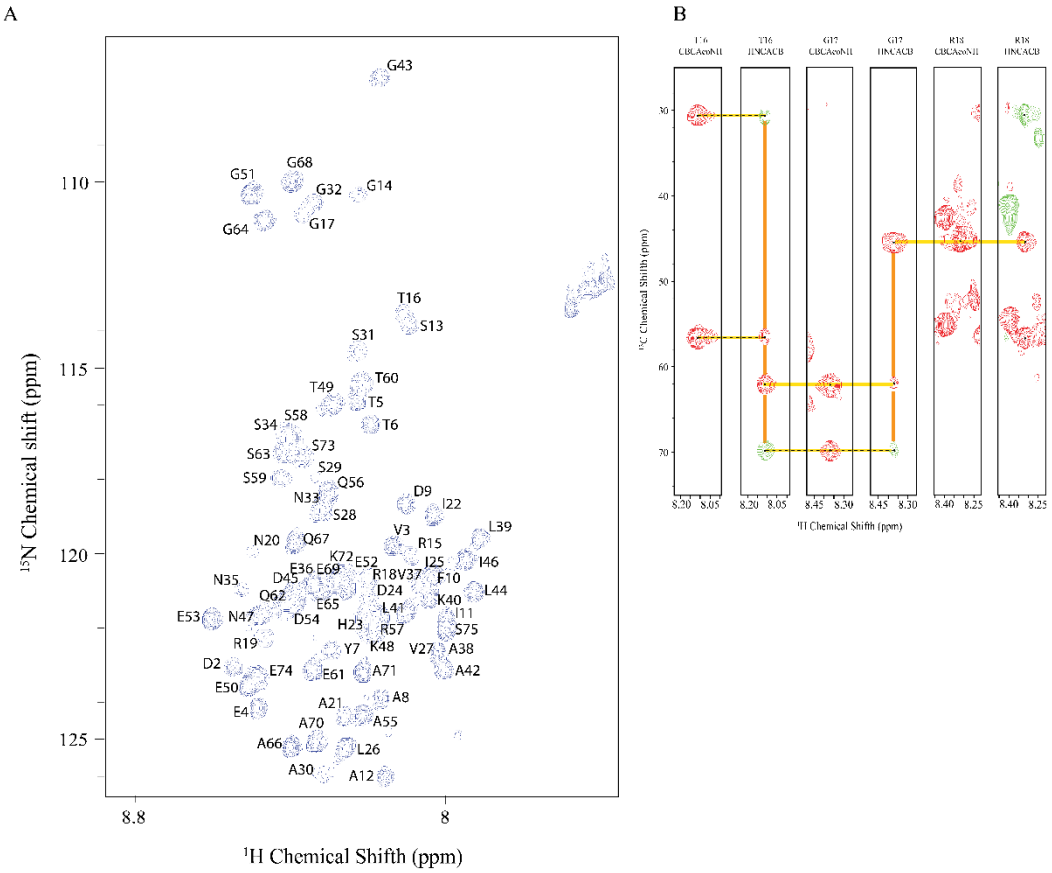

Figure 6.2. ^{1}H-^{15}N HSQC spectrum of of PKIα. (A) ^{1}H-^{15}N HSQC spectrum showing the assigments of the resonance peaks for PKIα in solution. (B) Selected ^{1}H-^{13}C planes from the 3D HNCACB (red and green) and 3D-CBCA(CO)NH (red) spectra taken at different nitrogen frequencies.

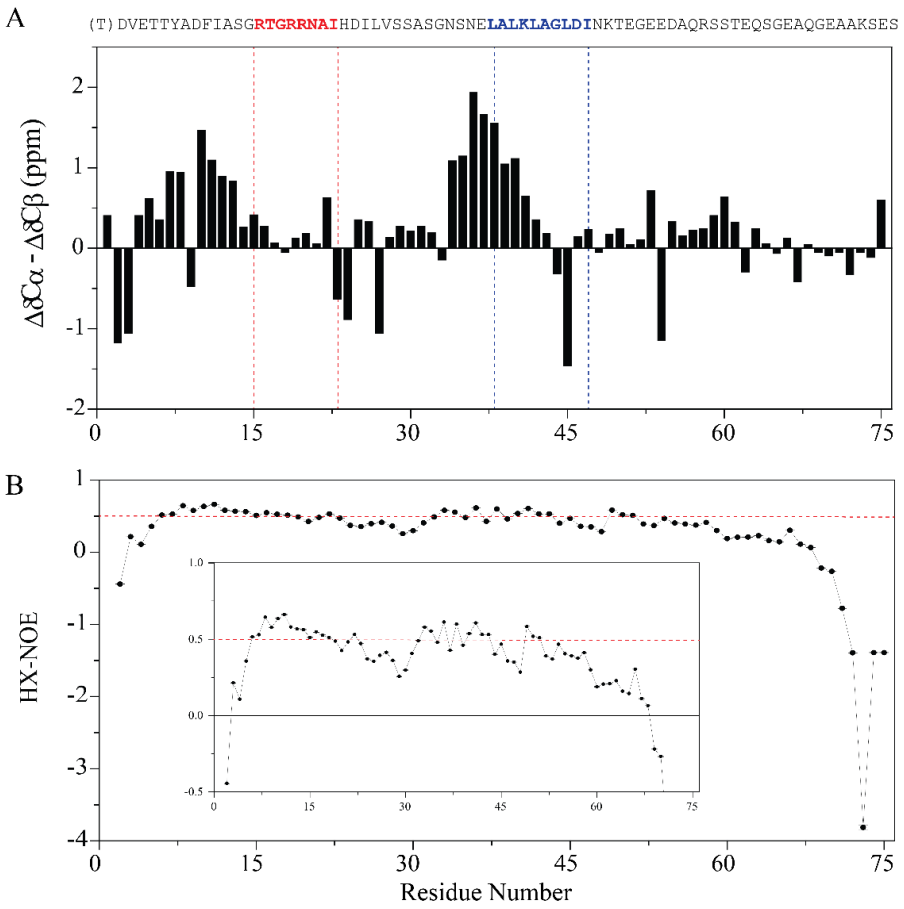

Figure 6.3. Chemical shift and HX-NOE for PKIα. Top: primary sequence of PKIα, where are highlighted in red the PSS residues and in blue the NES residues, respectively. (A) Graph of the ΔδCα-ΔδCβ calculated for each residue of PKIα. Positive values of CSI are indicative of α-helical secondary structure. (B) HX-NOE values obtained from each residues of PKIα sequence. In the box is enlarge the region between -0.5 and 1. Values of HX-NOE lower than 0.6 are indicative of highly dynamic (in the ps-ns time scale) residues.

6.2.2 Assignment and secondary structure of PKIα bound PKA-C

To access the change in structure of PKIα upon binding to PKA-C, we observed the change in the ^{1}H-^{15}N HSQC of PKIα. **Figure 6.4** reports the ^{1}H-^{15}N HSQC spectrum of uniformly $^{2}H/^{13}C/^{15}N$ labeled PKIα bound to the catalytic subunit of PKA (**Figure 6.4-A**). The majority of the resonances in the ^{1}H dimension show poor spectral dispersion. This indicated that even upon binding with PKA-C, PKIα itself does not undergo dramatic structural rearrangements, but remains mostly unfolded. However several resonances did experience large chemical shift changes (**Figure 6.5-A**) from the binding interaction. To identify which residues underwent significant changes, we performed triple resonance experiments on PKIα bound to PKA-C and 74 out of the total 75 amino acids were assigned (**Figure 6.4-B)**.

From the CSP obtained by comparing the free and bound state of PKIα (**Figure 6.6**), we observed that some residues show a higher chemical shift variations. The most perturbed resonances are located in the PSS sequence, which is consistent with structural model of PKI interaction with PKA-C [6]. The large change of the resonance chemical shifts of these residues is probably due to electrostatic interactions with the amino acids of the active site of PKA-C. We also observed that the residues in the NES experience a shift of their resonances, albeit too a lesser degree. To establish possible allosteric change that may propagate to the NES, we analyzed the CSI and steady-state NOE

values of PKIa bound to PKA-C (**Figure 5**). In general the CSI values and the steady-state NOE of the NES were higher when bound to PKA-C, as compared to those in the free form of PKIα. This implies that binding of PKA-C increases the helical propensity of the NES, and possibly primes the complex for export by CRM1.

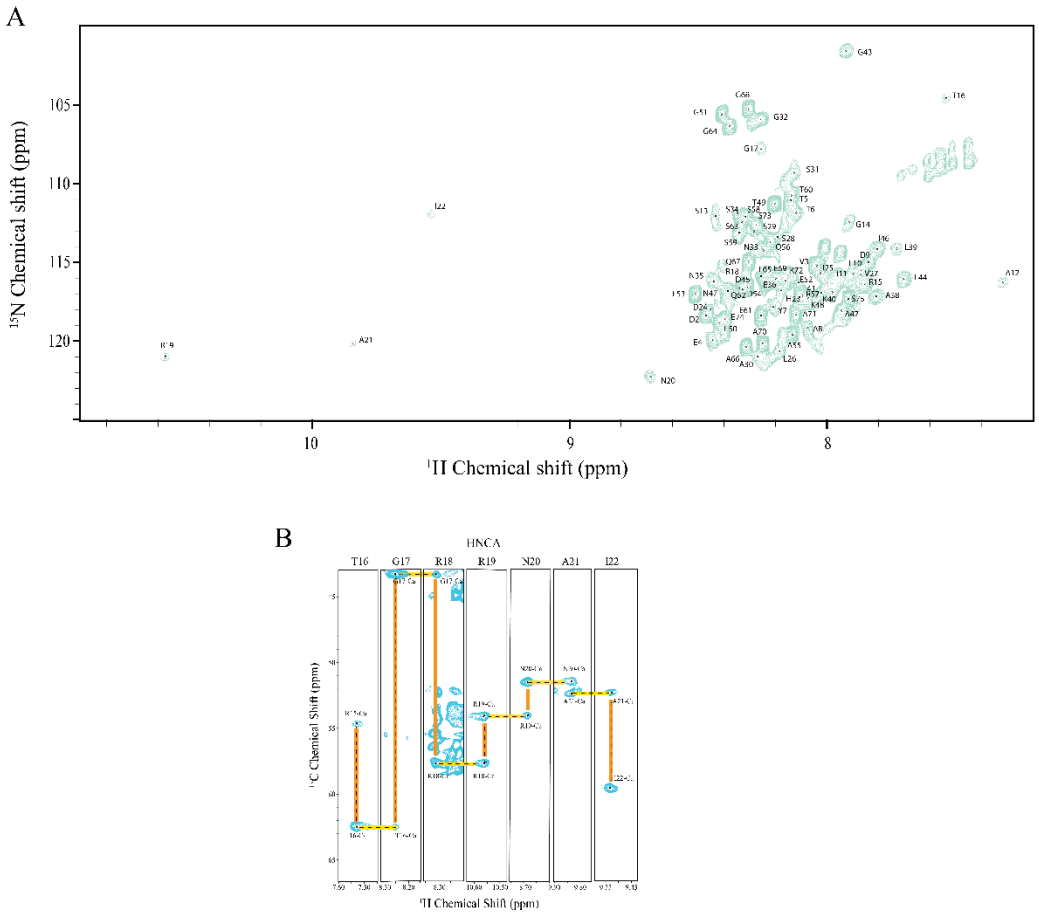

Figure 6.4. Mapping the interactions between PKIα and PKA-C. (A) **^{1}H-^{15}N** HSQC spectrum with reported the assigment of the resonance peaks. (B) Selected ^{1}H-^{13}C planes of overlaid 3D HNCA taken at the nitrogen frequencies of indicate backbone amide resonances, for the PSS residues.

.

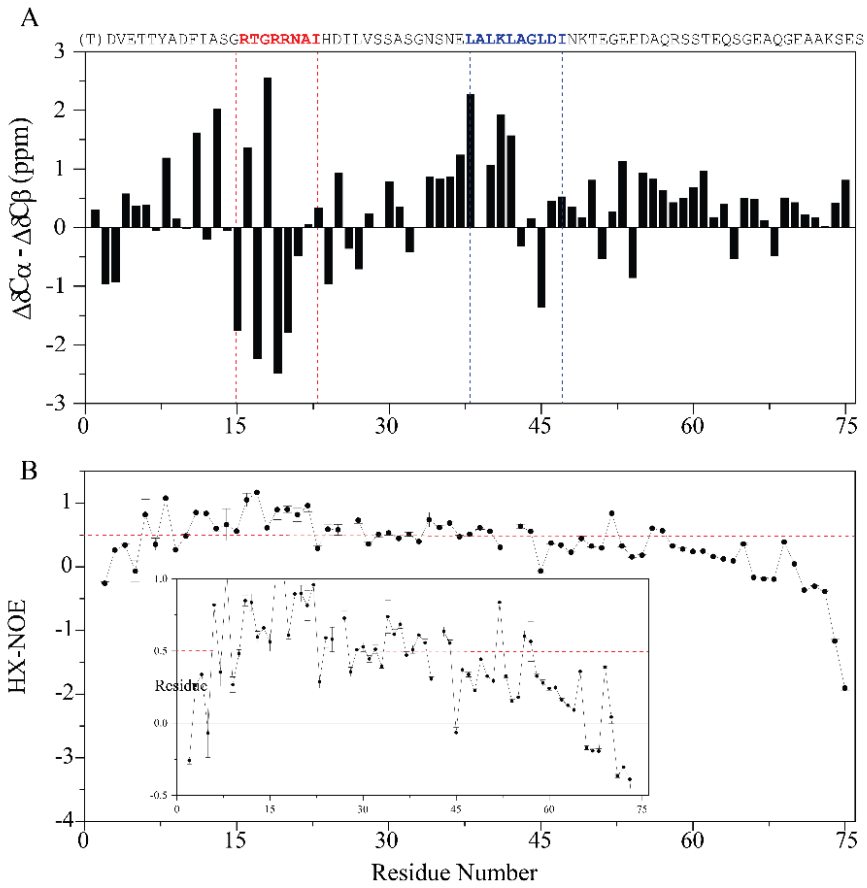

Figure 6.5. Chemical shift and HX-NOE for PKIα. On the top of the graphs is reported the primary sequence of PKIα, where are highlighted in red the PSS residues and in blue the NES residues, respectively. (A) Graph of the ΔδCα-ΔδCβ calculated for each residue of PKIα. Positive values of CSI are indicative of α-helical secondary structure. (B) HX-NOE values obtained from each residues of PKIα sequence. In the box is enlarge the region between -0.5 and 1. Values of HX-NOE lower.

.

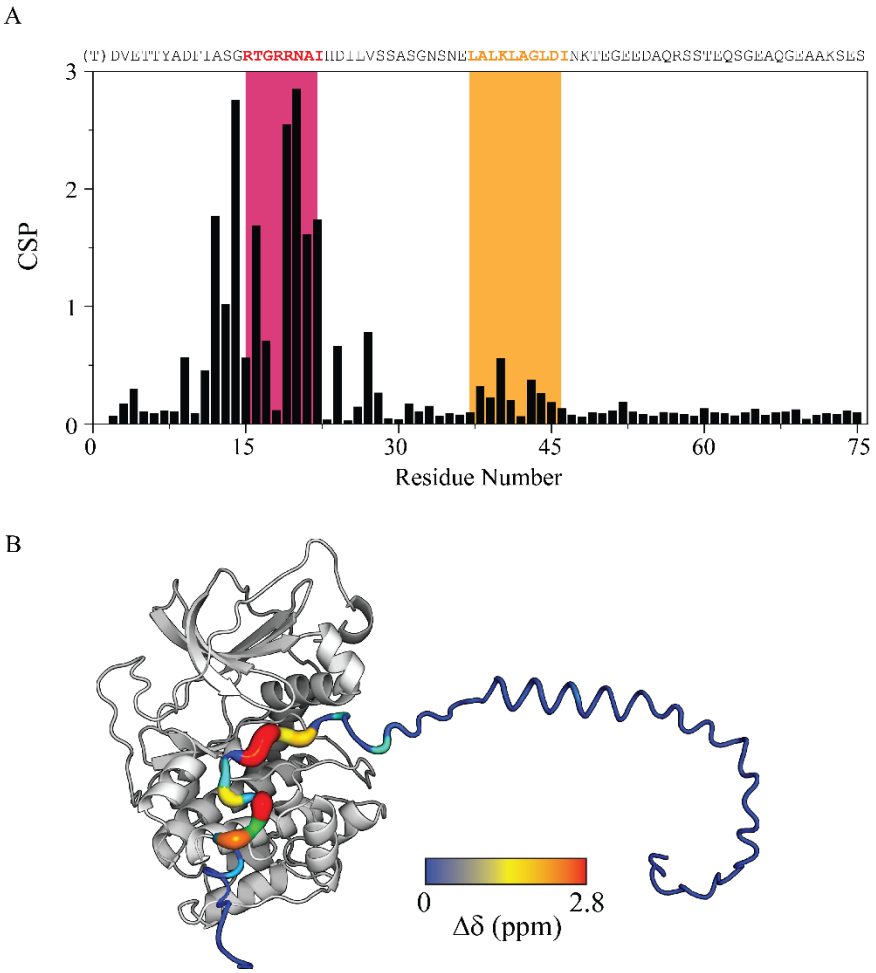

Figure 6.6. Chemical shift perturbation. (a) Chemical shift values obtained for each PKI residues. In pink and orange are highlighted the portion of the graph relative to the PSS and NES sequence, respectively. The residues that show more chemical shift changes from PKIα free to PKIα bound to PKA-C, are localized primarily in the N-terminal patron of the peptide. (B) Model of the structure of the complex between PKA-C and full-length PKI. In the PKI sequence are reported the CSP trends estimated for each amino acids.

6.2.3 Transient tertiary structure of PKIα

^{1}H PRE-Γ_2 experiments were performed by conjugating a nitroxide spin label (i.e., MTSL) using three different PKIα mutants, V3C, S28C and S59C, obtained by site-direct mutagenesis. The location of the mutations was chosen based the success of labeling from previous studies [208], which mapped the conformational changes of the overall PKIα structure using fluorescence probes. The interaction between a paramagnetic probe with an unpaired electron, like MTSL, with nearby protons (less than ~25 Å) causes a broadening of the NMR signals due to the increase of the Γ_2 relaxation (transverse relaxation) rate from dipolar coupling with the unpaired electron [206, 209-211]. Because of the strong interaction from the paramagnetic probe, both in distance and magnitude of relaxation, the presence of lowly populated conformational states can be detected by paramagnetic relaxation enhancement (PRE) at each nuclei. To observe these changes we measured both the peak intensity ratio in the presence of the active (I or I_{para}) and the inactive (I_0 or I_{dia}) spin label and directly measured the Γ_2 relaxation rate [206, 209-211].

Figure 6.7 reports the PRE ^{1}HN-Γ_2 rates calculated for the three PKI mutants, while **figure 6.8** shows the PRE effect as a function I/I_0,the ratio of the signal intensities for the resonances at paramagnetic (I) and diamagnetic (I_0) conditions. [212]. The presence of MTSL has a different effect on PKIα depending on its localization on the sequence. If PKIα was entirely disordered, then the PRE effect would be only localized along the primary sequence. How-

ever, that is not observed. When the spin label is localized at the N-terminus, (V3C) PRE effects are recorded in the linker region between the PSS and NES, but the resonances along the C-terminus are not affected. With S28C, when the probe is positioned in the linker region between the PPS and NES, strong PRE effects are observed both before and after the MTSL position, with some effect on the C-terminal region. When the probe is positioned in the unstructured C-terminus of PKIα, the majority of the residues (~ 75%) are effected by the presence of the spin label, with the exception of a few amino acids at the N-terminus. Our results demonstrate the presence of transient tertiary interaction in the structure of PKIα in absence of PKA-C. Based on the pattern of the PRE relaxation rates, these interactions involve almost the entire peptide. Further measurements and calculations will be used to construct a model of the transient structural interactions and compared to the PKA-C bound state of PKIα.

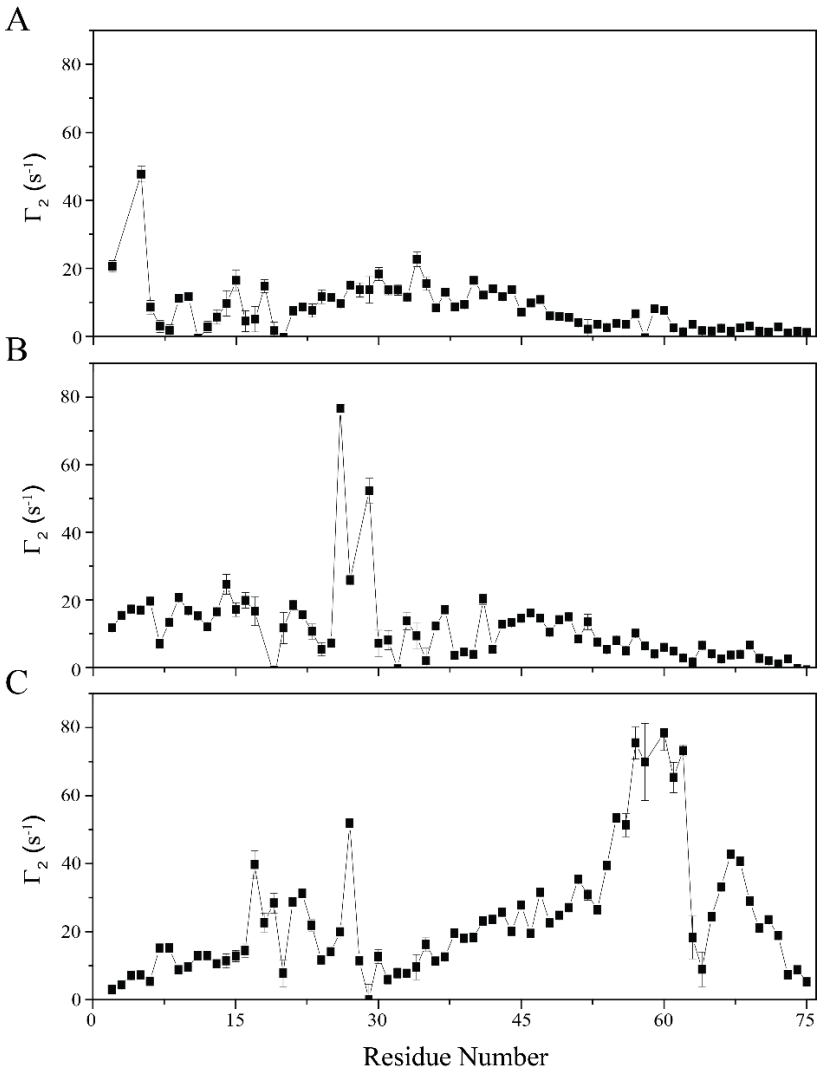

Figure 6.7. ^{1}H-PRE-Γ_2 rates for three different PKIα mutants. Intermolecular PRE profile observed for the three PKI mutants: (A) V3C, (B) S28C and (C) S59C, respectively, labeled with MTCL.

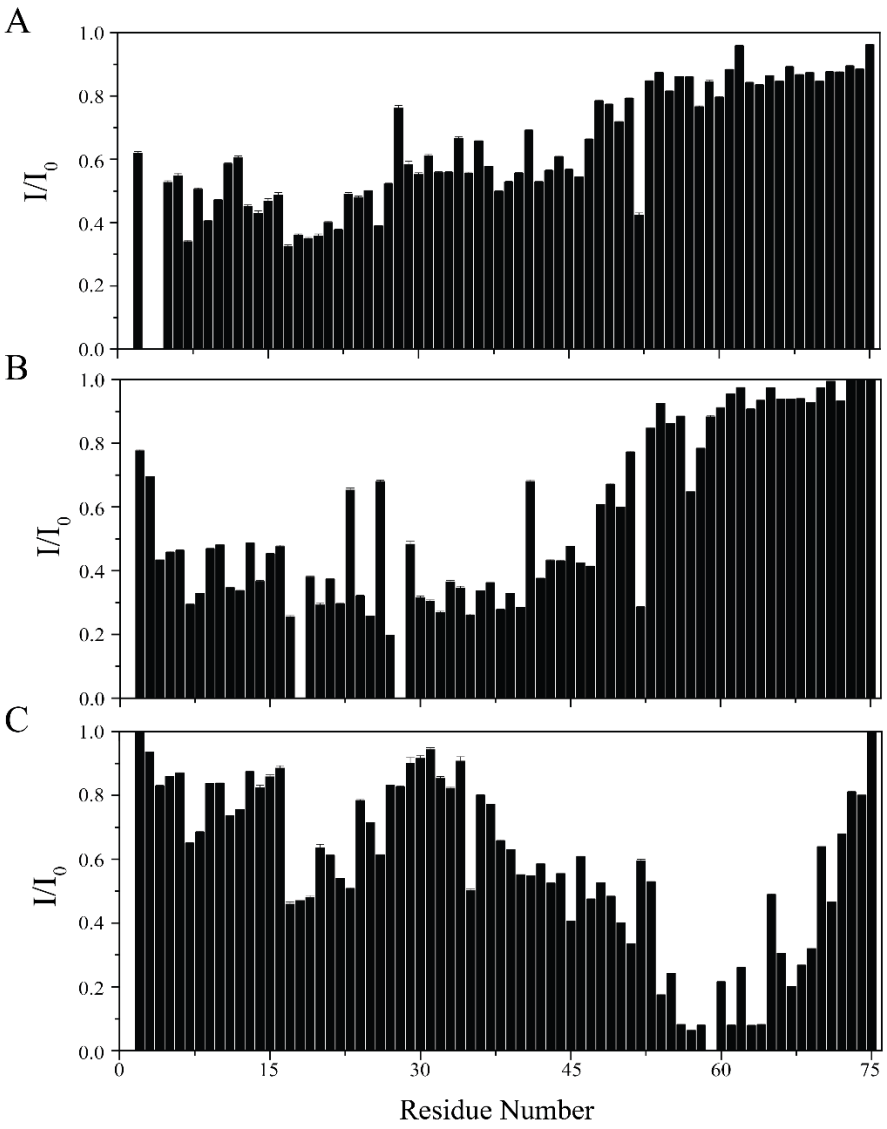

Figure 6.8. Intramolecular paramagnetic relaxation enhancement of PKI mutants, free in solution. Plots of intensity ratios for the observed for (A) V3C, (B) S28C, and (C) S59C PKI mutant spin labeled with MTSL.

6.3 Discussion and conclusion

PKI, together with R subunits, are the endogenous regulator of the activity and localization of the catalytic subunit of PKA [26, 161, 166, 167]. Due to the central role in cellular signaling played by PKA-C [161-165], these two proteins have been widely studied [26, 178]. Although the biological role of PKI is well-known [25, 213-215], the molecular mechanism underlying PKA-C:PKI recognition is still under debate.

In this section, we characterized the change in the conformational landscape that full-length PKIα undergoes upon binding to PKA-C (Apo to PKA-C bound). These studies were carried out by NMR spectroscopy, one of the most powerful techniques in the characterization of IDPs [114-116, 184, 207]. We assigned the NMR spectra of full-length PKIα free in solution and bound to PKA-C, which allowed us to calculate the chemical shift index (CSI) and the chemical shift perturbation (CSP), according to equation 6.1 [204].

We found that PKIα alone has minimal secondary structural elements with only two transient helices, localized in the N-terminus (residue 3-12), just before the PSS sequence, and in the NES region (residues 35-44 respectively). In the ^{1}H-^{15}N-NOESY experiment, it was not possible assign any medium- and long-range NOEs (data not showed), even in the peptide portions where the CSI suggested to be helical. The highly dynamic peptide and combined with the transient state of these portions, can explain the lack of NOEs observed. The ob-

tained results are in agreement with that reported by Hauer *et al.*, who have studied the full-length PKI alone through NMR spectroscopy [173],

When PKI was free in solution, we observed a propensity of the amino acids from residue 3 to residue 12 to be in a transient α-helix conformation. Walsh *et al.* identified this portion of PKI to be extremly important in the binding/anchoring to catalytic subunit and in the corect positioning of PSS inside of the catalytic site cleft of the enzyme [216-218]. Hauer *et al.* identified in the same portion a well-structured α-helix [173], while our data (both CSI values and the absence of medium- and long-range NOEs), indicates the presence of weak secondary stucture interactions. This discepancy is most likely due to the different approches used to analyze the PKIα. In Hauer's studies, the NMR structural characterization of the two ordered regions of PKIα where solved using truncated peptides, while we used the peptide full-length. More importantly, we used a new generation of NMR spectrometers, and higher eletromagnetic fields.

The second helix identified by Hauer *et al.*, (residue 35-44) contains numerous hydrophobic residues that are essential for the binding with CRM1 [171, 174]. Even in this case, our data suggest that the region is not folded, yet still presents a secondary structure propensity.

When PKIα is bound to PKA-C, in presence of AMP-PNP, only the portions that direcltly interact with the kinase undergoe significant structural rearragments, while the majority of the peptide is still unfolded. These portions are localized mainly at the N-terminus, where the transient α-helix present in

PKIα alone, become structurated, and play an importat role in the binding and correct posizione of PSS sequence in the binding site cleft of the kinase [6, 173, 180]. The resonances associated with the amino acid of PPS showed the highest CSP due to the electrostatic interactions made with the amino acids of the active site of PKA-C [207, 219]. Some changes are also observed in the linker region between PSS and NES. This region is still unstructured, but the presence of the kinase forces some degree of local rearrangement.

Interestingly, when PKIα is bound to PKA-C, the NES region undergoes a structural rearrangement, showing a higher secondary structure content. This portion is rich in hydrophobic residues (Leu 37, Leu 41, Leu 44) that have been demonstrated to be essential for high affinity binding to the nuclear export receptor RanGTP-CRM1 [220]. Güttler and coworkers solved the crystal structure of truncated-PKI containing the NES sequence in complex with RanGTP-CRM1 (**Figure 6.1**). They found that the NES-peptide, bond to the receptor, assumes a well-defined α-helical conformation with the Φ side chain of the Leu residues organized in a docking fashion to the binding pocket of CRM1. These authors also highlighted that the CRM1 binding pocket is a relatively rigid domain that is hypothesized to have NES sequences that must possess some plasticity to be able to bind the protein [220]. We observed that the NES portion has a higher propensity to fold in α-helix structure, when PKI is bound to PKA-C, even if it is far away from the portion that directly interacts with the kinase. This portion is still dynamic, due to the fact that it needs to interact with the rigid binding pocket of CRM1 to assume a well-defined secondary structure.

To better characterize the behavior of full-length PKI in absence of PKA-C, we decided to measure the PRE effects of MTSL, when it is positioned in three different points along PKIα sequence. The three mutants were affected in different ways by the spin label. These results demonstrated the presence of transiently tertiary interactions in the structure of PKIα in the absence of PKA-C. These interactions involve almost all of the peptide, but to a lesser extent at the N-terminus region. We characterized the full-length PKIα both free from and bound to PKA-C using NMR spectroscopy. We found that the free form of the peptide is mostly disordered with residual structure at the N-terminus and NES. Upon binding of PKA-C, the portion of PKIα that undergoes significant conformational changes were observed by NMR: the N-terminus, PSS and NES sequences, while the linker regions remains unstructured. We observed that binding to the catalytic subunit induces allosteric rearrangement of PKIα that propagates along the sequence. The binding with the enzyme stabilized by the N-terminus of PKIα [173, 214, 221] not only orients the correct position of PSS inside the active site of PKA-C, but it also induces allosteric changes in the NES as mapped by CSP. The increase in the HX-NOE and the CSI values of the NES, upon binding toward PKA-C, suggests this allosteric change may be due to a higher propensity for α-helical character of the NES. Paramagnetic relaxation enhancement (PRE) experiments showed that PKIα is not fully disordered in solution, but has transient tertiary intramolecular interaction between the C- and N-terminus. More studies need to be done to better understand how the con-

formational change in the structure of PKI are able to regulate the activity of PKA-C inside the cell.

Abstract

Intrinsically disordered proteins (IDPs) are proteins that do not fold into a stable globular structure but are biological active. These proteins are involved in regulation, recognition, and signaling process, where high-specificity/low affinity interactions with multiple partners are fundamental prerequisites. In the last thirty years, a class of small peptides, knowns as antimicrobial peptides (AMPs), similar to IDPs but involved in eukaryotic innate immune response against pathogen infections, have been the subjects of several studies to understand their mechanism of action and to discover and/or develop new antimicrobial substances, that can be used as antibiotic.

In the following PhD thesis we elucidate the structure, mechanism and function of several peptides which are characteristic of AMPs and IDPs. In particular, we determined the structure and function of the AMP *Chionodracine* (CND). We demonstrated that CND can bind to membranes of different lipid compositions with a preference for membranes mimicking those of prokaryotic cells. We also observed that upon the binding with phospholipid vesicles, the peptide remains adsorbed at the lipid surface, only partially exposed to the aqueous environment. In aqueous solution, the peptide is unfolded but undergoes to disorder-to- order transition, upon binding with phospholipid membranes. Based on the promising results obtained for CND, we designed three different CND mutants, with increased net positive charge and hydrophobicity,

and characterized their interaction with synthetic and natural membranes. We characterized the mutant's activity and function in presence of different phospholipid membranes. These studies demonstrated that the mutations have increased antimicrobial properties of CND. The mutants showed a stronger ability to interact, bind and disrupt membranes of different lipid compositions that can be directly correlated to the number of positively charged amino acids present in the sequence.

The heat-stable Protein Kinase Inhibitor (PKI) is a fully disordered 75 amino acid that regulate the activity and the intracellular localization of catalytic subunit of cAMP-dependent protein kinase A (PKA-C). To understand the molecular mechanism underlying recognition of PKA-C by PKI, we characterized the change in the conformational landscape that PKI undergoes upon binding to PKA-C (Apo to PKA-C bound). These studies were carried out using NMR spectroscopy, the only structural technique to provide atomic resolution detail on IDPs. Using chemical shift analysis and nuclear spin relaxation experiments, we demonstrated that PKI alone has minimal secondary structural elements with only two transient helixes. However, paramagnetic relaxation enhancement (PRE) experiments show that PKI is not fully disordered, but has transient tertiary intramolecular interaction between the C- and N-terminus. When PKI is bound to the kinase, in the presence of the non-hydrolysable ATP mimic, β,γ-Imidoadenosine 5′-triphosphate (ATP□N), only the sequence that directly interacts with the PKA-C undergoes significant structural rearrangement while the majority of the peptide is still unfolded.

Appendix

A.1. NMR Spectroscopy

Nuclear magnetic resonance is a phenomenon in which nuclei in a magnetic field absorb and emit electromagnetic radiation in the radio frequency range. The basic phenomenon was discovered independently by Felix Bloch and Edward M Purcell, at 1946 [222, 223]. With the development of Fourier transform NMR spectroscopy and multi-dimensional NMR in the 1970s [224, 225], NMR spectroscopy has been a flagship technique for structural and dynamic characterization of bio-macromolecules. To understand how NMR spectroscopy allows for the characterization of bio-macromolecules, a brief outline of the theory of NMR spectroscopy will be presented here.

Atoms, that are the building blocks of molecules, consist of nuclei with surrounding electrons. The nucleus and the electron have four fundamental properties: mass, charge, electron/magnetic shape and spin angular momentum. The manifestation of angular momentum from nuclear spin is the basis for nuclear magnetism and consequently of NMR spectroscopy [219]. The nuclear spin angular momentum is an intrinsically quantum mechanical property of the atom that does not have classical analogue. It is characterized by the nuclear spin quantum number, **I**. Not all the nuclei can be observed in NMR spectroscopy (**Table A.1**).

TABLE A.1 Properties of nuclei frequently used in NMR

Nucleus	Spin quantum number I	γ^a (T s)$^{-1}$	Sensitivity relative to ^{1}H	Natural abundance (%)
^{1}H	1/2	2.6752×10^8	100.0	99.99
^{2}H	1	4.1067×10^7	0.965	0.012
^{13}C	1/2	6.7265×10^7	1.590	1.07
^{15}N	1/2	-2.7108×10^7	0.104	0.37
^{19}F	1/2	2.6167×10^8	83.30	100.00
^{31}P	1/2	1.0839×10^8	6.630	100.00

The nuclear spin angular momentum, **I**, is a vector quantity with magnitude given by:

$$|\mathbf{I}| = [\mathbf{I} \cdot \mathbf{I}]^{1/2} = \hbar[I(I+1)]^{1/2} \qquad [A.1.1]$$

in which I is the nuclear spin angular moment quantum number and $\hbar$ is Planck's constant. Due to the commutation properties of angular momentum, only the total angular momentum and one of the three Cartesian component of angular momentum, the *z*-component, are observation. The *z*-component is specified by the following equation:

$$I_z = \hbar m, \qquad [A.1.2]$$

in which m is the magnetic momentum number defined by $2I+1$. The orientation of the spin angular momentum vector is quantized. Nuclei that have nonzero spin angular momentum possess a nuclear magnetic moment, $\boldsymbol{\mu}$, and the z-component of the magnetic moment, μ_z, defined by:

$$\boldsymbol{\mu} = \gamma \mathbf{I},$$

$$\mu_z = \gamma I_z = \gamma \hbar m, \qquad [A.1.3]$$

in which γ, is the gyromagnetic ratio (a constant that described the susceptibility of a nuclei with response to a magnetic field). When a nucleus is in presence of a static external magnetic field, **B** (**Figure A.1.1-A**), the spin states of the nucleus have energies given by:

$$E = -\boldsymbol{\mu} \cdot \boldsymbol{B}, \qquad \text{[A.1.4]}$$

In a NMR spectrometer, the static external magnetic field is directed, by convention, along the *z*-axis on the laboratory coordinate system (B_o). Equation A.1.4 can be written as:

$$E_m = \mu_z \cdot B_o = -\gamma I_z B_o = -\gamma m \hbar B_o \qquad \text{[A.1.5]}$$

For spin ½ nuclei, the magnetic quantum number, m can take the value of m=±1/2. In presence of a static magnetic field, the nuclear magnetic momentum of the spin interacts with B_o, leading to a splitting of the energy levels, known as Zeeman splitting (**Figure A.1.1-B**). At equilibrium, the different energy levels are not equally populated. The population of the states is directly correlated to the nuclei and the applied magnetic field. The energy of the transition between two Zeeman levels is:

$$\Delta E = -\hbar \gamma B_o \qquad \text{[A.1.6]}$$

Hence, the energy/frequency of the electromagnetic radiation required to induce the transition from Zeeman levels is derived from A.1.6 and Plank's law:

$$\omega = \frac{\Delta E}{\hbar} = \gamma B_o \qquad \text{[A.1.7.a]}$$

$$\nu = \frac{\omega}{2\pi} = \frac{\gamma B_0}{2\pi} \qquad \text{[A.1.7.b]}$$

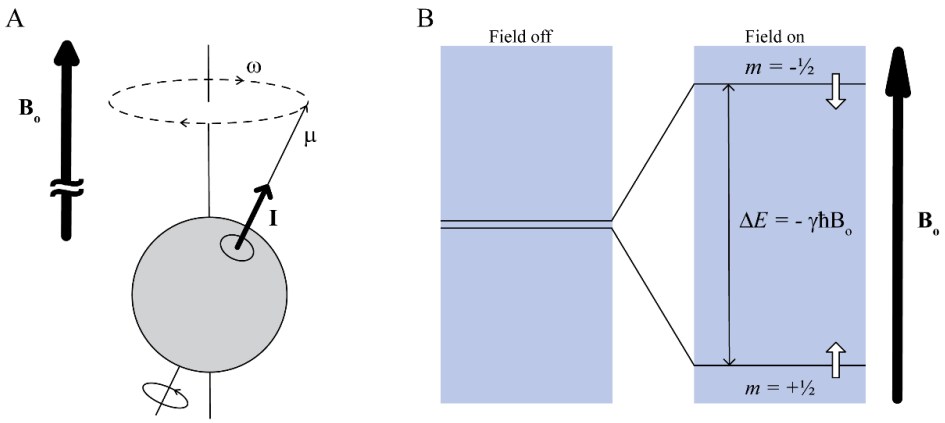

Figure A.1.1. Schematic representation of a spin in presence of an external magnetic field (B_o) (A). Zeeman levels, in absence and in presence of B_o.

For an isolated nuclei, only two nuclear spin states exist in the presence of an external magnetic field two energy levels (separated by $\Delta E=\hbar\gamma B_0$) are obtained. Without an external magnetic field, all the orientations of the nuclear spin angular momentum are possible. In presence of an external magnetic field, the spins will be oriented along the direction of the external magnetic field. The distribution of the spins at thermal equilibrium is described by the Boltzmann distribution, which is given by the following:

$$\frac{N_\beta}{N_\alpha} = e^{-\frac{\Delta E}{kT}}, \qquad \text{[A.1.8]}$$

Where ΔE is the energy difference between lower (E_α) and higher (E_β) energy state, T is the temperature and where *k* is the Boltzmann constant. Since there will be a slight excess of spins in the ground state in the presence of a magnetic field, the bulk spins will exhibit a magnetic moment, **M**(t), that that processes

around B_0 with a frequency $\omega = -\gamma B_0$. This precessional frequency, known as Larmor frequency, is given by the following equation:

$$\omega_0 = -\gamma B_0 \qquad \text{[A.1.9]}$$

When a radiofrequency (rf) electromagnetic radiation is applied, the bulk magnetization is displaced from equilibrium. The rf electromagnetic radiation (pulse) generate a magnetic field that perturbs the bulk **M**(t). Once the bulk magnetization is applied will precess in the static field at Larmor frequency and will generate a signal that can be detected. The NMR signal will be proportional to the magnetization that is also dependent on the spin polarization, P. This one, is given by the population difference between the two Zeeman levels divided by the total number of spin.

The two most important factors that influence the outcome of NMR experiment are sensitivity and resolution. The NMR sensitivity is defined as the signal to noise ratio (S/N) obtained in a fixed amount of time. This value depends on numerous parameters, but it can be summarized in the following equation:

$$S/N \propto N\gamma_e \sqrt{\gamma_d B_0 t} \qquad \text{[A.1.10]}$$

where N is the number of spins, γ_e is the gyromagnetic ratio of the exited spin, γ_d is the gyromagnetic ratio of the detected spin, B_0 is the external magnetic field and t is experiment acquisition time. Other factor involved in the S/N are the related to the spectrometer components. The resolution depends on the chemical shift dispersion and on the signal linewidths. In NRM spectrum, two

peaks can be resolved when their difference in frequency is larger respect to their linewidths.

A.1.1 NMR spectroscopy on the study of AMPs

Over the years, NMR techniques have been used to determine the three-dimensional (3D) structure solution of AMPs in fluorinated organic solvents [226-229], detergent micelles [230, 231] and isotropic bicelles [232-235]. For short AMPs homonuclear correlational spectroscopy is adequate to provide sufficient resolution for structure determination [236-238]. The typical experiments that are used for structure determination are the two-dimensional (2D) correlated spectroscopy (COSY) [236, 238], total correlated spectroscopy (TOCSY) [127, 128] and nuclear Overhauser enhancement spectroscopy (NOESY) experiments [130, 239].

^{1}H-^{1}H COSY and TOCSY experiments provide inter-residue correlations between protons using through-bond (i.e. scalar) coupling. This allows the mapping of the "spin system" of each amino acid, aiding in the identification of the amino acid in the sequence. The COSY experiment also allows for the measurement of three-bond scalar coupling values[219]. Using the Karplus equation [240], these values allow for the determination of the torsion angles. Most importantly, these values allow for the unambiguous determination of secondary structure elements through ^{1}HN to ^{1}Hα scalar coupling values [136, 219].

Contrarily to COSY and TOCSY experiments, the NOESY experiment provides correlations between protons through dipole-dipole cross-relaxation. The NOE-

SY experiment provides correlation through space in space with a distance dependence of r^{-6} and is the basis for structure determination. The maximum distance restraint from NOE cross-peaks between two protons is approximately 5.5 Å [136, 219, 239]. Due to spin diffusion the cross-peaks are not quantified, but rather analyzed semi-quantitatively by separated by their intensities into strong, medium and weak cross-peaks, which are categorized in specific distance restrains that will be used to perform structure calculation.

There are available several programs that use the data from the NOESY, COSY and TOCSY experiments and to converts these into spatial restrains for structure calculation. The TALOS program [137] predicts the φ angle and ψ angles for the peptide backbone using the chemical shift values calculated for $^{1}H\alpha$, ^{15}N, ^{13}CO, $^{13}C\alpha$ and $^{13}C\beta$, (**Figure A.1.2**). To convert the structural restraints into a structural model, Xplor-NIH [138] is a common open-source software used for this purpose. The program uses the structural restraints as harmonic restraints and performs an energy minimization protocol starting from a fully extended structure. The initial high temperature is slowly reduced to allow for the system to slowly approach a possible solution given the chemical and spectral restraints[219].

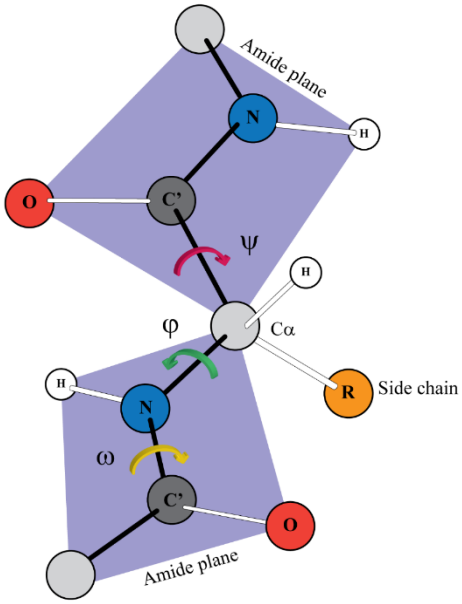

Figure A.1.2. Dihedral angles in proteins. In a polypeptide chain three dihedral angles are defined as ψ (psi) (C'-Ca bound), φ (phi) (Ca-N bound), and σ (N-C', peptide bound). Due the planarity of the peptide bound, the values that ω can assume is 180° (in trans) or 0° (in cis).

Usually the solution-state NMR studies of AMPs are recorded in presence of detergent micelles (dodeylphosphocoline –DPC or sodium dodecylsulphate-SDS) that provide a membrane mimic [2]. Typically micelles are a spherical monolayer of molecules (diameter of ~ 3 nm). This membrane mimicking-system is only an approximation of the membrane bilayer. The high curvature of micelles can induce structural changes of AMPs and incorrect folding along the micelle surface (**Figure A.1.3**) [230, 231]. Alternately, discoidal micelles or isotopic bicelles can be used. Bicelles are model lipid bilayers that are formed spontaneously by mixing long-chain phospholipids (1,2-dimyristoyl-*sn*-glycero-3-phosphocoline -DMPC or 1,2-dimyristoyl-*sn*-glycero-3-phosphocrylglycerol

sodium salt – DMPG) and amphiphilic molecules (like CHAPSO), or short-chain lipid, such as 1,2-diheptanoyl-*sn*-glycero-3-phosphocoline (DHPC) in a specific molar ratio (**Figure A.1.3**)[231-234]. The properties of bicelles are primarily dependent on the composition of the lipids used and the *q*-ratio, the molar ratio between the lipid and the detergent. For bicelles with a *q*-ratio over 1, then these are called anisotropic bicelles where the excess of long change lipids results in a disk like shape [241-243]. However for solution-NMR studies most commonly bicelles with a *q* under 1 are used to create isotropic bicelles which tumble spherically.

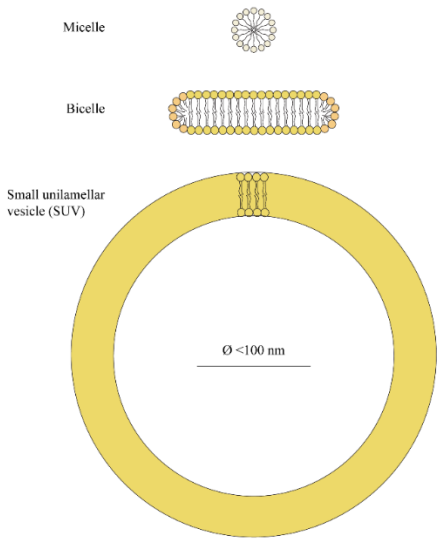

Figure A.1.3. Size, shape and composition of membrane mimicking system used in NMR spectroscopy.

One of the biggest limitation of solution-state NMR studies is that it is not possible to study the interaction of AMPs with their natural phospholipid bilayer [2]. Oriented solid-state NMR (Oss-NMR) is an alternative technique that has

been used to describe AMP/membrane interaction [2, 244]. Typically AMPs are reconstituted with either anisotropic bicelles, which spontaneously align in the magnetic field, or mechanically aligned bilayers supported on glass plates [71, 75, 245]. In Oss-NMR the membrane is always parallel or perpendicular to the magnetic field. As a result the orientation of the interaction of AMPs with respect to the phospholipid bilayer can be directly measured using Oss-NMR techniques because in solid state NMR all spectral observable parameters are dependent on the orientation of the nuclei with respect to the magnetic field [2, 244]. Although many experiments have been devised to measure the orientation of AMPs with respect to the bilayer, the most common and powerful experiment is the polarization inversion spin exchange at the magic angle (PISEMA) experiment [246, 247]. This measures the chemical shift and the dipolar coupling of the backbone amide group. These values are unique for each amino acid in the peptide chain and can be used to back calculate the orientation of the peptide plane with respect to the membrane bilayer.

A.1.2 NMR spectroscopy on the study of IDPs

Interest IDPs has swelled in recent years as a result of the realization that such proteins are common in human and other genomes [84, 248, 249]. Full IDPs and proteins with extended IDR, are associated with a variety of biological functions, many of them intimately related to human diseases [85, 86, 250].The absence of a well-defined 3D-structure and the high dynamic conformation of these proteins mean that IDPs are unamenable with standard structure determination methods. Although many IDPs adopt a more “ordered” structure upon interaction with a target protein [80, 105, 184, 251] and their structure determined by crystallography, most have evaded in this fashion. In the majority of the cases, even the bound state of the IDPs retains substantial mobility [114].

However, many techniques that have been developed to study protein folding are now applied for structural characterization of IDPs. The foundation of the structural theory of IDPs is the conformational ensemble dictates the overall function of the protein [14, 16]. Hence, the main goal of these studies is to obtain experimental constrains that reflect on the properties of the ensemble. These measurements may include the detection of residual secondary structure, transient long-range contacts and regions of altered mobility. NMR spectroscopy is the only technique that provides atomic resolution structural information on an ensemble level and as a result emerged as a premier experimental technique to study IDPs[184].

As discussed earlier, backbone chemical shifts of ^{1}H and ^{13}C nuclei are readily used to provide torsion angles of the backbone for secondary structure

determination. This approach is readily applied for the determination of weak transient secondary structure elements as well. The chemical shift index (CSI) [145, 252] is the difference between the measured chemical shift and a reference chemical shift value measured in a random coil. A value of over zero indicates propensity for α-helical structure, less than zero for a β-sheet and a value of approximately zero indicates complete disorder. Nuclear spin relaxation experiments are a complimentary measurement for the determination of secondary structure. NMR relaxation experiments, T_1, T_2 and steady-state NOE experiments [253, 254].

The detection of long-range transient tertiary structure is usually derived from the analysis of residual dipolar couplings (RDCs) [255, 256] and paramagnetic relaxation enhancement (PRE) experiments [28, 212]. Overall, the PRE experiment has found the most success for the determination of long-range contacts in IDP ensembles [257-260]. Since most proteins are diamagnetic, the PRE effect is typically introduced in the form of a nitroxide electron spin label conjugated to a cysteine residue through its thiol group. Alternately, chelating groups can also be uses to introduce a paramagnetic metal, like ethylene-diaminetetra-acetic acid (EDTA)-Mn^{2+}. NMR active nuclei in the proximity of an electron spin label relax more efficiently leading to a broadened signal. Since the electron has a higher gyromagnetic ratio than proton, the PRE effect has a range up to approximately 25 Å with a distance dependence of $\langle r^{-6} \rangle$ [212].

A.2. Fluorescence spectroscopy

The fluorescence is a luminescent phenomenon that arise from the excited state of a molecule. Fluorescence spectroscopy study the light radiation spontaneously emitted by this excited state. This phenomenon can be explained by Jablonski diagram (**Figure A.2.1**). This diagram illustrates the electronic states of a molecule and the transition between them. The states are arranged vertically by energy and grouped horizontally by spin multiplicity. The vibrational ground states of each electron state are indicate by the number (0, 1, 2, etc). When a molecule is excited, by absorbing a photon of energy $E = h\nu$, the electrons are promoted from the singlet ground state (S_0) to an excited state of singlet (S_1 and S_2). With a few rare exception, the excited molecule rapidly relax to the lowest vibrational level of S_1, through a mechanism called internal conversion that generally occur within 10^{-12} s. The fluoresce process arise from the same vibrational level of S_1, and is a radiative de-stimulating process through which the excited molecule returns to the lowest vibrational levels of the ground state (S_0). The fluorescence occur within 10^{-9}-10^{-8} s, so the internal conversion is complete prior to emission. Consequently the energy of emission is typically less than that of absorption, so fluorescence occurs typically at lower energy (or longer wavelengths) than absorption. Upon excitation into higher electronic and vibrational levels, the excess of energy is quickly dissipated and so the emission spectra is usually independent of the excitation wavelength.

Fluorescence lifetime and quantum yield are the most important characteristics of a fluorophore. The fluorescence quantum yield is the number of emitted photons relative to the number of the absorbed photons, while the lifetime determines the time available for the fluorophore to interact/diffuse in the environment. The quantum yield depends, not only on the number of emitted/absorbed photon, but also is influenced by the non-radiative phenomena occurring that cause the rapidly relaxation of the excited state [140].

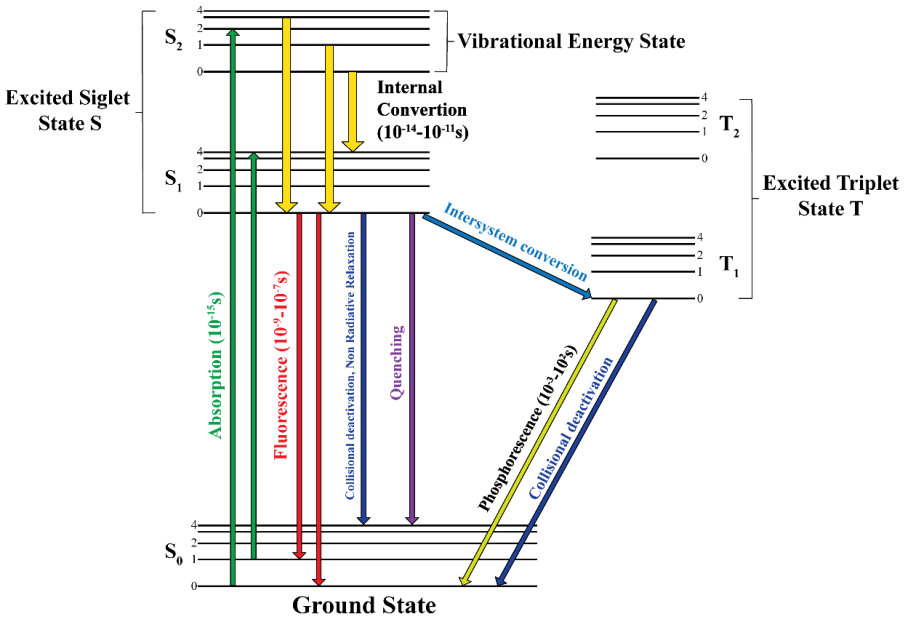

Figure A.2.1. Jablonsky diagram.

A.2.1 Fluorescence quenching

"Fluorescence quenching" indicates the decrease of the fluorescence intensity caused by different processes. There are mainly two different quenching mechanisms: the *collisional/dynamic quenching* and the *static quenching*.

The *collisional quenching* occurs when the excited fluorophore is deactivated upon contact with some molecules (named quencher) in solution, and the deactivation occurs without chemical alteration of neither the quencher nor the fluorophore. Upon the contact, the fluorophore returns to the ground state without the emission of photons. In this case, the quenching occurs without any chemical alteration of the fluorophore. By contrast, in the *static quenching*, the quencher forms a non-fluorescence complex with the fluorophore, through a photochemical reaction that allow the relaxation to the ground state without the emission of photons.

Both collisional and static quenching require molecular contact between the fluorophore and the quencher. There are several collisional quencher that can be used. The best-known is the molecular oxygen that is active against almost all the known fluorophores. Alternatively, heavy metal atoms, such as Cs^+ or anions such as iodide (I^-) and bromide (Br^-) or purines, pyrimidines, acrylamide, can be used. The choice of the appropriate quencher is one of the most important step in the collisional quenching analysis. The quenchers have different size and they can have different accessibility to the fluorophores, performing different kind of quenching.

The collisional quenching is described by the Stern-Volmer equation:

$$\frac{F_0}{F} = 1 + k_q \tau_0 [Q] = 1 + K_D [Q] \qquad \text{[A.2.1.1]}$$

where F_0 and F are the fluorescence intensities in the absence and presence of the quencher, respectively: k_q is the quenching rate constant, τ_0 is the lifetime of the fluorophore, $[Q]$ is the concentration of the quencher, and K_D is the Stern-Volmer (K_{SV}) constant for the collisional quenching, given by $K_D = k_q \tau_0$. Based on this equation, the F_0/F ratio is expected to be linearly dependent to the quencher concertation. Consequently, the K_D^{-1} represent the quencher concentration at which the 50% of the fluorescence intensity is quenched. Deviation of the linearity of the Stern-Volmer plot is indicative of the presence of two or more quenchers in the solution. The k_d value is extremely important because describes the efficiency of the quenching process and is in relation with the accessibility of the fluorophore to the quencher. Smaller values of k_d, referred to a diffusion-controlled value, are associate to a low quenching efficiency.

The collisional quenching is a time-dependent process while the static quenching is due to the formation of a non-fluorescence complex between the quencher and the fluorophore, which promote the return of the latest to the ground state without the emission of photons. The static quenching can is describe by the following equation:

$$\frac{F_0}{F} = 1 + K_S [Q] \qquad \text{[A.2.1.2]}$$

where K_S in the constant for the static quenching and is given by:

$$K_s = \frac{[F-Q]}{[F][Q]} \qquad \text{[A.2.1.3]}$$

where [*F*-*Q*] is the concentration of the complex between the quencher (Q) and the fluorophore (F), [*F*]is the concentration of un-complexed fluorophore, and [*Q*]is the quencher concentration. Even for the static quenching, the correlation between the variation of the fluorescence intensity (F_0/F) and the quencher concentration is linear.

The collisional quenching can be differentiate from the static quenching through (a) measurement of fluorescence lifetime, (b) emission intensities, even if additional information are required, and (c) by the analysis of the excitation spectrum of the fluorophore.

Reference

1. Chan, D.I., E.J. Prenner, and H.J. Vogel, *Tryptophan- and arginine-rich antimicrobial peptides: structures and mechanisms of action.* Biochim Biophys Acta, 2006. **1758**(9): p. 1184-202.
2. Haney, E.F. and H.J. Vogel, *Chapter 1 NMR of Antimicrobial Peptides*, in *Annual Reports on NMR Spectroscopy*. 2009, Academic Press. p. 1-51.
3. van der Lee, R., et al., *Classification of intrinsically disordered regions and proteins.* Chem Rev, 2014. **114**(13): p. 6589-631.
4. Manning, G., et al., *The Protein Kinase Complement of the Human Genome.* Science, 2002. **298**(5600): p. 1912-1934.
5. Zhang, P., et al., *Structure and allostery of the PKA RIIbeta tetrameric holoenzyme.* Science, 2012. **335**(6069): p. 712-6.
6. Knighton, D.R., et al., *Structure of a peptide inhibitor bound to the catalytic subunit of cyclic adenosine monophosphate-dependent protein kinase.* Science, 1991. **253**(5018): p. 414-20.
7. Wright, P.E. and H.J. Dyson, *Intrinsically Disordered Proteins in Cellular Signaling and Regulation.* Nature reviews. Molecular cell biology, 2015. **16**(1): p. 18-29.
8. Olivieri, C., et al., *Structure and membrane interactions of chionodracine, a piscidin-like antimicrobial peptide from the icefish Chionodraco hamatus.* Biochim Biophys Acta, 2015. **1848**(6): p. 1285-93.
9. SELA, M., F.H. WHITE, and C.B. ANFINSEN, *Reductive Cleavage of Disulfide Bridges in Ribonuclease.* Science, 1957. **125**(3250): p. 691-692.
10. Sander, I.M., J.L. Chaney, and P.L. Clark, *Expanding Anfinsen's Principle: Contributions of Synonymous Codon Selection to Rational Protein Design.* Journal of the American Chemical Society, 2014. **136**(3): p. 858-861.
11. Turoverov, K.K., I.M. Kuznetsova, and V.N. Uversky, *The protein kingdom extended: ordered and intrinsically disordered proteins, their folding, supramolecular complex formation, and aggregation.* Prog Biophys Mol Biol, 2010. **102**(2-3): p. 73-84.
12. Dunker, A.K., et al., *Intrinsically disordered proteins and multicellular organisms.* Seminars in Cell & Developmental Biology, 2015. **37**: p. 44-55.

13. Dunker, A.K., et al., *Intrinsic protein disorder in complete genomes.* Genome Inform. Ser. Workshop Genome Inform., 2000. **11**: p. 161-171.
14. Dunker, A.K., *Intrinsically disordered protein.* J. Mol. Graph. Model., 2001. **19**: p. 26-59.
15. Dunker, A.K., et al., *Intrinsic disorder and protein function.* Biochemistry, 2002. **41**: p. 6573-6582.
16. Uversky, V.N., *Intrinsically disordered proteins from A to Z.* The International Journal of Biochemistry & Cell Biology, 2011. **43**(8): p. 1090-1103.
17. Uversky, V.N., *Seven lessons from one IDP structural analysis.* Structure, 2010. **18**(9): p. 1069-71.
18. Uversky, V.N. and A.K. Dunker, *Understanding protein non-folding.* Biochim Biophys Acta, 2010. **1804**(6): p. 1231-64.
19. Dyson, H.J. and P.E. Wright, *Coupling of folding and binding for unstructured proteins.* Curr. Opin. Struct. Biol., 2002. **12**: p. 54-60.
20. Last, N.B., D.E. Schlamadinger, and A.D. Miranker, *A common landscape for membrane-active peptides.* Protein Science, 2013. **22**(7): p. 870-882.
21. Butterfield, S.M. and H.A. Lashuel, *Amyloidogenic protein-membrane interactions: mechanistic insight from model systems.* Angew Chem Int Ed Engl, 2010. **49**(33): p. 5628-54.
22. Milletti, F., *Cell-penetrating peptides: classes, origin, and current landscape.* Drug Discov Today, 2012. **17**(15-16): p. 850-60.
23. Zasloff, M., *Antimicrobial peptides of multicellular organisms.* Nature, 2002. **415**: p. 389-395.
24. Buonocore, F., et al., *A piscidin-like antimicrobial peptide from the icefish Chionodraco hamatus (Perciformes: Channichthyidae): molecular characterization, localization and bactericidal activity.* Fish Shellfish Immunol, 2012. **33**(5): p. 1183-91.
25. Walsh, D.A., et al., *Krebs EG: Purification and characterization of a protein inhibitor of adenosine 3',5'-monophosphate-dependent protein kinases.* J Biol Chem, 1971. **246**(7): p. 1977-85.
26. Johnson, D.A., et al., *Dynamics of cAMP-dependent protein kinase.* Chem Rev, 2001. **101**(8): p. 2243-70.

27. Scott, J.D., et al., *Primary-structure requirements for inhibition by the heat-stable inhibitor of the cAMP-dependent protein kinase.* Proc Natl Acad Sci U S A, 1986. **83**(6): p. 1613-6.
28. Solomon, I., *Relaxation Processes in a System of Two Spins.* Physical Review, 1955. **99**(2): p. 559-565.
29. Zasloff, M., *Antibiotic peptides as mediators of innate immunity.* Curr. Opin. Immunol., 1992. **4**: p. 3-7.
30. Andreu, D. and L. Rivas, *Animal antimicrobial peptides: an overview.* Biopolymers, 1998. **47**(6): p. 415-33.
31. Bulet, P., R. Stocklin, and L. Menin, *Anti-microbial peptides: from invertebrates to vertebrates.* Immunol Rev, 2004. **198**: p. 169-84.
32. Dubos, R.J. and C. Cattaneo, *Studies on a Bactericidal Agent Extracted from a Soil Bacillus : Iii. Preparation and Activity of a Protein-Free Fraction.* J Exp Med, 1939. **70**(3): p. 249-56.
33. Dubos, R.J., *Studies on a Bactericidal Agent Extracted from a Soil Bacillus : Ii. Protective Effect of the Bactericidal Agent against Experimental Pneumococcus Infections in Mice.* J Exp Med, 1939. **70**(1): p. 11-7.
34. Hultmark, D., et al., *Insect immunity. Purification and properties of three inducible bactericidal proteins from hemolymph of immunized pupae of Hyalophora cecropia.* Eur J Biochem, 1980. **106**(1): p. 7-16.
35. Steiner, H., et al., *Sequence and specificity of two antibacterial proteins involved in insect immunity.* Nature, 1981. **292**(5820): p. 246-248.
36. Boman, H.G., A. Boman, and A. Pigon, Insect Biochem., 1981. **11**: p. 33-42.
37. Bahar, A.A. and D. Ren, *Antimicrobial Peptides.* Pharmaceuticals, 2013. **6**(12): p. 1543-1575.
38. Powers, J.P. and R.E.W. Hancock, *The relationship between peptide structure and antibacterial activity.* Peptides, 2003. **24**: p. 1681-1691.
39. Huang, Y., J. Huang, and Y. Chen, *α-helical cationic antimicrobial peptides: relationships of structure and function.* Protein Cell, 2010. **1**: p. 143-152.
40. Rozek, A., C.L. Friedrich, and R.E. Hancock, *Structure of the bovine antimicrobial peptide indolicidin bound to dodecylphosphocholine and sodium dodecyl sulfate micelles.* Biochemistry, 2000. **39**(51): p. 15765-74.

41. Papagianni, M., *Ribosomally synthesized peptides with antimicrobial properties: biosynthesis, structure, function, and applications.* Biotechnol Adv, 2003. **21**(6): p. 465-99.
42. Wang, G., X. Li, and Z. Wang, *APD2: the updated antimicrobial peptide database and its application in peptide design.* Nucleic Acids Res, 2009. **37**(Database issue): p. D933-7.
43. Porcelli, F., et al., *On the role of NMR spectroscopy for characterization of antimicrobial peptides.* Methods Mol Biol, 2013. **1063**: p. 159-80.
44. Yeaman, M.R. and N.Y. Yount, *Mechanisms of antimicrobial peptide action and resistance.* Pharmacol Rev, 2003. **55**(1): p. 27-55.
45. Singer, S.J. and G.L. Nicolson, *The Fluid Mosaic Model of the Structure of Cell Membranes.* Science, 1972. **175**(4023): p. 720-731.
46. Sohlenkamp, C. and O. Geiger, *Bacterial membrane lipids: diversity in structures and pathways.* FEMS Microbiology Reviews, 2016. **40**(1): p. 133-159.
47. Shai, Y., *Mechanism of the binding, insertion and destabilization of phospholipid bilayer membranes by alpha-helical antimicrobial and cell non-selective membrane-lytic peptides.* Biochim Biophys Acta, 1999. **1462**(1-2): p. 55-70.
48. Papo, N. and Y. Shai, *Can we predict biological activity of antimicrobial peptides from their interactions with model phospholipid membranes?* Peptides, 2003. **24**(11): p. 1693-703.
49. Teixeira, V., M.J. Feio, and M. Bastos, *Role of lipids in the interaction of antimicrobial peptides with membranes.* Prog Lipid Res, 2012. **51**(2): p. 149-77.
50. Epand, R.M. and R.F. Epand, *Bacterial membrane lipids in the action of antimicrobial agents.* J. Pept. Sci., 2011. **17**: p. 298-305.
51. Almeida, P.F. and A. Pokorny, *Mechanisms of antimicrobial, cytolytic, and cell-penetrating peptides: from kinetics to thermodynamics.* Biochemistry, 2009. **48**(34): p. 8083-93.
52. Almeida, P.F. and A. Pokorny, *Binding and permeabilization of model membranes by amphipathic peptides.* Methods Mol Biol, 2010. **618**: p. 155-69.
53. Huang, H.W., *Action of antimicrobial peptides: two-state model.* Biochemistry, 2000. **39**(29): p. 8347-52.
54. Bechinger, B., *Membrane association and pore formation by alpha-helical peptides.* Adv Exp Med Biol, 2010. **677**: p. 24-30.

55. White, S.H. and W.C. Wimley, *MEMBRANE PROTEIN FOLDING AND STABILITY: Physical Principles.* Annual Review of Biophysics and Biomolecular Structure, 1999. **28**(1): p. 319-365.
56. Seelig, J., *Thermodynamics of lipid–peptide interactions.* Biochimica et Biophysica Acta (BBA) - Biomembranes, 2004. **1666**(1–2): p. 40-50.
57. Wimley, W.C., *Describing the mechanism of antimicrobial peptide action with the interfacial activity model.* ACS Chem. Biol., 2010. **5**: p. 905-917.
58. Hristova, K. and W.C. Wimley, *A Look at Arginine in Membranes.* The Journal of Membrane Biology, 2011. **239**(1): p. 49-56.
59. Oren, Z. and Y. Shai, *Mode of action of linear amphipathic alpha-helical antimicrobial peptides.* Biopolymers, 1998. **47**(6): p. 451-63.
60. Shai, Y., *Mode of action of membrane active antimicrobial peptides.* Biopolymers, 2002. **66**(4): p. 236-48.
61. Ludtke, S.J., et al., *Membrane pores induced by magainin.* Biochemistry, 1996. **35**(43): p. 13723-8.
62. Brogden, K.A., *Antimicrobial peptides: pore formers or metabolic inhibitors in bacteria?* Nature Rev. Microbiol., 2005. **3**: p. 238-250.
63. Porcelli, F., et al., *NMR structure of the cathelicidin-derived human antimicrobial peptide LL-37 in dodecylphosphocholine micelles.* Biochemistry, 2008. **47**(20): p. 5565-72.
64. Shai, Y. and Z. Oren, *From "carpet" mechanism to de-novo designed diastereomeric cell-selective antimicrobial peptides.* Peptides, 2001. **22**(10): p. 1629-41.
65. Pokorny, A. and P.F. Almeida, *Kinetics of dye efflux and lipid flip-flop induced by delta-lysin in phosphatidylcholine vesicles and the mechanism of graded release by amphipathic, alpha-helical peptides.* Biochemistry, 2004. **43**(27): p. 8846-57.
66. Wieprecht, T., et al., *Membrane binding and pore formation of the antibacterial peptide PGLa: thermodynamic and mechanistic aspects.* Biochemistry, 2000. **39**(2): p. 442-52.
67. Ladokhin, A.S., W.C. Wimley, and S.H. White, *Leakage of membrane vesicle contents: determination of mechanism using fluorescence requenching.* Biophysical Journal, 1995. **69**(5): p. 1964-1971.

68. Ladokhin, A.S., S. Jayasinghe, and S.H. White, *How to measure and analyze tryptophan fluorescence in membranes properly, and why bother?* Anal Biochem, 2000. **285**(2): p. 235-45.
69. Gregory, S.M., A. Pokorny, and P.F. Almeida, *Magainin 2 revisited: a test of the quantitative model for the all-or-none permeabilization of phospholipid vesicles.* Biophys J, 2009. **96**(1): p. 116-31.
70. Gregory, S.M., et al., *A quantitative model for the all-or-none permeabilization of phospholipid vesicles by the antimicrobial peptide cecropin A.* Biophys J, 2008. **94**(5): p. 1667-80.
71. Opella, S.J., C. Ma, and F.M. Marassi, *Nuclear magnetic resonance of membrane-associated peptides and proteins.* Methods Enzymol, 2001. **339**: p. 285-313.
72. De Angelis, A.A., et al., *Amphipathic antimicrobial piscidin in magnetically aligned lipid bilayers.* Biophys J, 2011. **101**(5): p. 1086-94.
73. Verardi, R., et al., *Probing membrane topology of the antimicrobial peptide distinctin by solid-state NMR spectroscopy in zwitterionic and charged lipid bilayers.* Biochim Biophys Acta, 2011. **1808**(1): p. 34-40.
74. Mote, K.R., et al., *Multidimensional oriented solid-state NMR experiments enable the sequential assignment of uniformly 15N labeled integral membrane proteins in magnetically aligned lipid bilayers.* J Biomol NMR, 2011. **51**(3): p. 339-46.
75. Bechinger, B., et al., *Orientations of amphipathic helical peptides in membrane bilayers determined by solid-state NMR spectroscopy.* J Biomol NMR, 1991. **1**(2): p. 167-73.
76. Wimley, W.C. and S.H. White, *Membrane partitioning: distinguishing bilayer effects from the hydrophobic effect.* Biochemistry, 1993. **32**(25): p. 6307-12.
77. Ladokhin, A.S., S. Jayasinghe, and S.H. White, *How to Measure and Analyze Tryptophan Fluorescence in Membranes Properly, and Why Bother?* Analytical Biochemistry, 2000. **285**(2): p. 235-245.
78. Kriwacki, R.W., et al., *Structural studies of p21Waf1/Cip1/Sdi1 in the free and Cdk2-bound state: conformational disorder mediates binding diversity.* Proc Natl Acad Sci U S A, 1996. **93**(21): p. 11504-9.
79. Daughdrill, G.W., et al., *The C-terminal half of the anti-sigma factor, FlgM, becomes structured when bound to its target, sigma 28.* Nat Struct Biol, 1997. **4**(4): p. 285-91.

80. Wright, P.E. and H.J. Dyson, *Intrinsically unstructured proteins: re-assessing the protein structure-function paradigm.* J. Mol. Biol., 1999. **293**: p. 321-331.
81. Uversky, V.N., J.R. Gillespie, and A.L. Fink, *Why are 'natively unfolded' proteins unstructured under physiologic conditions?* Proteins, 2000. **41**: p. 415-427.
82. Tompa, P., *Intrinsically unstructured proteins.* Trends Biochem. Sci., 2002. **27**: p. 527-533.
83. Uversky, V.N., *Natively unfolded proteins: a point where biology waits for physics.* Protein Sci., 2002. **11**: p. 739-756.
84. Ward, J.J., et al., *Prediction and functional analysis of native disorder in proteins from the three kingdoms of life.* J. Mol. Biol., 2004. **337**: p. 635-645.
85. Fink, A.L., *Natively unfolded proteins.* Curr Opin Struct Biol, 2005. **15**(1): p. 35-41.
86. Dyson, H.J. and P.E. Wright, *Intrinsically unstructured proteins and their functions.* Nat Rev Mol Cell Biol, 2005. **6**(3): p. 197-208.
87. Dunker, A.K., et al., *The unfoldomics decade: an update on intrinsically disordered proteins.* BMC Genomics, 2008. **9 Suppl 2**: p. S1.
88. Gsponer, J. and M.M. Babu, *The rules of disorder or why disorder rules.* Prog Biophys Mol Biol, 2009. **99**(2-3): p. 94-103.
89. Tompa, P., *Intrinsically disordered proteins: a 10-year recap.* Trends Biochem Sci, 2012. **37**(12): p. 509-16.
90. Forman-Kay, J.D. and T. Mittag, *From sequence and forces to structure, function, and evolution of intrinsically disordered proteins.* Structure, 2013. **21**(9): p. 1492-9.
91. Romero, P., *Sequence complexity of disordered protein.* Proteins, 2001. **42**: p. 38-48.
92. Tompa, P., C. Szasz, and L. Buday, *Structural disorder throws new light on moonlighting.* Trends Biochem Sci, 2005. **30**(9): p. 484-9.
93. Chen, J.W., et al., *Conservation of intrinsic disorder in protein domains and families: II. functions of conserved disorder.* J Proteome Res, 2006. **5**(4): p. 888-98.
94. Mukhopadhyay, S., et al., *A natively unfolded yeast prion monomer adopts an ensemble of collapsed and rapidly fluctuating structures.* Proc Natl Acad Sci U S A, 2007. **104**(8): p. 2649-54.
95. Wright, P.E., H.J. Dyson, and R.A. Lerner, *Conformation of peptide fragments of proteins in aqueous solution: implications for initiation of protein folding.* Biochemistry, 1988. **27**(19): p. 7167-75.

96. Dyson, H.J. and P.E. Wright, *Equilibrium NMR studies of unfolded and partially folded proteins.* Nat Struct Biol, 1998. **5 Suppl**: p. 499-503.
97. Radhakrishnan, I., et al., *Conformational preferences in the Ser133-phosphorylated and non-phosphorylated forms of the kinase inducible transactivation domain of CREB.* FEBS Lett., 1998. **430**: p. 317-322.
98. Rogers, J.M., A. Steward, and J. Clarke, *Folding and Binding of an Intrinsically Disordered Protein: Fast, but Not 'Diffusion-Limited'.* Journal of the American Chemical Society, 2013. **135**(4): p. 1415-1422.
99. Teufel, D.P., et al., *Backbone-driven collapse in unfolded protein chains.* J Mol Biol, 2011. **409**(2): p. 250-62.
100. Burgen, A.S., G.C. Roberts, and J. Feeney, *Binding of flexible ligands to macromolecules.* Nature, 1975. **253**(5494): p. 753-5.
101. Boehr, D.D., R. Nussinov, and P.E. Wright, *The role of dynamic conformational ensembles in biomolecular recognition.* Nat Chem Biol, 2009. **5**(11): p. 789-96.
102. Ma, B. and R. Nussinov, *Regulating highly dynamic unstructured proteins and their coding mRNAs.* Genome Biol, 2009. **10**(1): p. 204.
103. Fuxreiter, M. and P. Tompa, *Fuzzy complexes: a more stochastic view of protein function.* Adv Exp Med Biol, 2012. **725**: p. 1-14.
104. Mittag, T. and J.D. Forman-Kay, *Atomic-level characterization of disordered protein ensembles.* Curr Opin Struct Biol, 2007. **17**(1): p. 3-14.
105. Wright, P.E. and H.J. Dyson, *Linking folding and binding.* Curr Opin Struct Biol, 2009. **19**(1): p. 31-8.
106. Espinoza-Fonseca, L.M., *Reconciling binding mechanisms of intrinsically disordered proteins.* Biochem Biophys Res Commun, 2009. **382**(3): p. 479-82.
107. Kiefhaber, T., A. Bachmann, and K.S. Jensen, *Dynamics and mechanisms of coupled protein folding and binding reactions.* Curr Opin Struct Biol, 2012. **22**(1): p. 21-9.
108. Tompa, P. and M. Fuxreiter, *Fuzzy complexes: polymorphism and structural disorder in protein-protein interactions.* Trends Biochem Sci, 2008. **33**(1): p. 2-8.
109. Receveur-Brechot, V., et al., *Assessing protein disorder and induced folding.* Proteins, 2006. **62**(1): p. 24-45.
110. Sibille, N. and P. Bernado, *Structural characterization of intrinsically disordered proteins by the combined use of NMR and SAXS.* Biochem Soc Trans, 2012. **40**(5): p. 955-62.

111. Schuler, B. and H. Hofmann, *Single-molecule spectroscopy of protein folding dynamics--expanding scope and timescales.* Curr Opin Struct Biol, 2013. **23**(1): p. 36-47.
112. Banerjee, P.R. and A.A. Deniz, *Shedding light on protein folding landscapes by single-molecule fluorescence.* Chem Soc Rev, 2014. **43**(4): p. 1172-88.
113. Brucale, M., B. Schuler, and B. Samori, *Single-molecule studies of intrinsically disordered proteins.* Chem Rev, 2014. **114**(6): p. 3281-317.
114. Eliezer, D., *Biophysical characterization of intrinsically disordered proteins.* Current opinion in structural biology, 2009. **19**(1): p. 23-30.
115. Dyson, H.J. and P.E. Wright, *Elucidation of the protein folding landscape by NMR.* Methods Enzymol, 2005. **394**: p. 299-321.
116. Dyson, H.J. and P.E. Wright, *Unfolded proteins and protein folding studied by NMR.* Chem. Rev., 2004. **104**: p. 3607-3622.
117. Silphaduang, U. and E.J. Noga, *Peptide antibiotics in mast cells of fish.* Nature, 2001. **414**(6861): p. 268-9.
118. Noga, E.J. and U. Silphaduang, *Piscidins: a novel family of peptide antibiotics from fish.* Drug News Perspect, 2003. **16**(2): p. 87-92.
119. Park, N.G., et al., *Structure-activity relationships of piscidin 4, a piscine antimicrobial peptide.* Biochemistry, 2011. **50**(16): p. 3288-99.
120. Hsu, J.C., et al., *Characteristics of the antitumor activities in tumor cells and modulation of the inflammatory response in RAW264.7 cells of a novel antimicrobial peptide, chrysophsin-1, from the red sea bream (Chrysophrys major).* Peptides, 2011. **32**(5): p. 900-10.
121. Hilchie, A.L., et al., *Pleurocidin-family cationic antimicrobial peptides are cytolytic for breast carcinoma cells and prevent growth of tumor xenografts.* Breast Cancer Research, 2011. **13**(5): p. 1-16.
122. Hancock, R.E.W. and H.-G. Sahl, *New strategies and compounds for anti-infective treatment.* Current Opinion in Microbiology, 2013. **16**(5): p. 519-521.
123. Garg, P., et al., *Transmembrane pore formation by the carboxyl terminus of Bax protein.* Biochim Biophys Acta, 2013. **1828**(2): p. 732-42.
124. Domadia, P.N., et al., *Structure, interactions, and antibacterial activities of MSI-594 derived mutant peptide MSI-594F5A in lipopolysaccharide micelles: role of the helical*

hairpin conformation in outer-membrane permeabilization. J Am Chem Soc, 2010. **132**(51): p. 18417-28.

125. White, S.H., et al., *[4] Protein folding in membranes: Determining energetics of peptide-bilayer interactions*, in *Methods in Enzymology*. 1998, Academic Press. p. 62-87.
126. Rathinakumar, R. and W.C. Wimley, *Biomolecular engineering by combinatorial design and high-throughput screening: small, soluble peptides that permeabilize membranes.* J Am Chem Soc, 2008. **130**(30): p. 9849-58.
127. Bax, A. and D.G. Davis, *MLEV-17-based two-dimensional homonuclear magnetization transfer spectroscopy.* Journal of Magnetic Resonance (1969), 1985. **65**(2): p. 355-360.
128. Braunschweiler, L., G. Bodenhausen, and R.R. Ernst, *Analysis of networks of coupled spins by multiple quantum N.M.R.* Molecular Physics, 1983. **48**(3): p. 535-560.
129. Kumar, A., R.R. Ernst, and K. Wuthrich, *A two-dimensional nuclear Overhauser enhancement (2D NOE) experiment for the elucidation of complete proton-proton cross-relaxation networks in biological macromolecules.* Biochem Biophys Res Commun, 1980. **95**(1): p. 1-6.
130. Kövér, K.E. and G. Batta, *Theoretical and practical aspects of one- and two-dimensional heteronuclear overhauser experiments and selective 13C T1-determinations of heteronuclear distances.* Progress in Nuclear Magnetic Resonance Spectroscopy, 1987. **19**(3): p. 223-266.
131. Bodenhausen, G. and D.J. Ruben, *Natural abundance nitrogen-15 NMR by enhanced heteronuclear spectroscopy.* Chemical Physics Letters, 1980. **69**(1): p. 185-189.
132. Bax, A. and M.F. Summers, *Proton and carbon-13 assignments from sensitivity-enhanced detection of heteronuclear multiple-bond connectivity by 2D multiple quantum NMR.* Journal of the American Chemical Society, 1986. **108**(8): p. 2093-2094.
133. Delaglio, F., et al., *NMRPipe: a multidimensional spectral processing system based on UNIX pipes.* J Biomol NMR, 1995. **6**(3): p. 277-93.
134. Goddard, T.D.a.K., D.G., *Sparky 3.* 14 University of California, San Francisco, 2004. **15**.
135. Neuhaus, D., et al., *Systematic application of high-resolution, phase-sensitive two-dimensional 1H-NMR techniques for the identification of the amino-acid-proton spin systems in proteins. Rabbit metallothionein-2.* Eur J Biochem, 1985. **151**(2): p. 257-73.

136. Wuthrich, K., *NMR of proteins and nucleic acids.* Wiley, 1986.
137. Shen, Y., et al., *TALOS+: a hybrid method for predicting protein backbone torsion angles from NMR chemical shifts.* J Biomol NMR, 2009. **44**(4): p. 213-23.
138. Schwieters, C.D., et al., *The Xplor-NIH NMR molecular structure determination package.* J Magn Reson, 2003. **160**(1): p. 65-73.
139. Andrushchenko, V.V., et al., *Thermodynamics of the interactions of tryptophan-rich cathelicidin antimicrobial peptides with model and natural membranes.* Biochim Biophys Acta, 2008. **1778**(4): p. 1004-14.
140. Lakowicz, J.R., *Principles of Fluorescence Spectroscopy, 3rd edition.* Spinger, 2006.
141. Fu, F.N. and B.R. Singh, *Calcein permeability of liposomes mediated by type A botulinum neurotoxin and its light and heavy chains.* J Protein Chem, 1999. **18**(6): p. 701-7.
142. Porcelli, F., et al., *Structure and orientation of pardaxin determined by NMR experiments in model membranes.* J Biol Chem, 2004. **279**(44): p. 45815-23.
143. Porcelli, F., et al., *Structures of the dimeric and monomeric variants of magainin antimicrobial peptides (MSI-78 and MSI-594) in micelles and bilayers, determined by NMR spectroscopy.* Biochemistry, 2006. **45**(18): p. 5793-9.
144. Mascioni, A., et al., *Conformational preferences of the amylin nucleation site in SDS micelles: an NMR study.* Biopolymers, 2003. **69**(1): p. 29-41.
145. Wishart, D.S., B.D. Sykes, and F.M. Richards, *The chemical shift index: a fast and simple method for the assignment of protein secondary structure through NMR spectroscopy.* Biochemistry, 1992. **31**(6): p. 1647-51.
146. Berjanskii, M.V. and D.S. Wishart, *Application of the random coil index to studying protein flexibility.* J Biomol NMR, 2008. **40**(1): p. 31-48.
147. Roscia, G., et al., *The development of antimicrobial peptides as new antibacterial drugs.* Curr Protein Pept Sci, 2013. **14**(8): p. 641-9.
148. Perrin, B.S., Jr., et al., *High-resolution structures and orientations of antimicrobial peptides piscidin 1 and piscidin 3 in fluid bilayers reveal tilting, kinking, and bilayer immersion.* J Am Chem Soc, 2014. **136**(9): p. 3491-504.
149. Lee, S.A., et al., *Solution structure and cell selectivity of piscidin 1 and its analogues.* Biochemistry, 2007. **46**(12): p. 3653-63.
150. Tossi, A., L. Sandri, and A. Giangaspero, *Amphipathic, alpha-helical antimicrobial peptides.* Biopolymers, 2000. **55**(1): p. 4-30.

151. Giangaspero, A., L. Sandri, and A. Tossi, *Amphipathic alpha helical antimicrobial peptides.* Eur J Biochem, 2001. **268**(21): p. 5589-600.
152. Franco, O.L., *Peptide promiscuity: an evolutionary concept for plant defense.* FEBS Lett., 2011. **585**: p. 995-1000.
153. Eftink, M.R. and C.A. Ghiron, *Exposure of tryptophanyl residues in proteins. Quantitative determination by fluorescence quenching studies.* Biochemistry, 1976. **15**(3): p. 672-80.
154. Eftink, M.R., *Fluorescence techniques for studying protein structure.* Methods Biochem Anal, 1991. **35**: p. 127-205.
155. Garg, P., et al., *Transmembrane pore formation by the carboxyl terminus of Bax protein.* Biochim. Biophys. Acta, 2013. **1828**(2): p. 732-742.
156. Fjell, C.D., et al., *Designing antimicrobial peptides: form follows function.* Nat Rev Drug Discov, 2012. **11**(1): p. 37-51.
157. Ganz, T., *Macrophages and systemic iron homeostasis.* J Innate Immun, 2012. **4**(5-6): p. 446-53.
158. Franco, O.L., *Peptide promiscuity: an evolutionary concept for plant defense.* FEBS Lett, 2011. **585**(7): p. 995-1000.
159. Lehrer, R.I. and T. Ganz, *Defensins of vertebrate animals.* Current Opinion in Immunology, 2002. **14**(1): p. 96-102.
160. Ganz, T., *Defensins: antimicrobial peptides of vertebrates.* C R Biol, 2004. **327**(6): p. 539-49.
161. Taylor, S.S., et al., *PKA: a portrait of protein kinase dynamics.* Biochim Biophys Acta, 2004. **1697**(1-2): p. 259-69.
162. Taylor, S.S., et al., *PKA: lessons learned after twenty years.* Biochim Biophys Acta, 2013. **1834**(7): p. 1271-8.
163. Niedner, R.H., et al., *Protein kinase resource: an integrated environment for phosphorylation research.* Proteins, 2006. **63**(1): p. 78-86.
164. Taylor, S.S. and A.P. Kornev, *Protein kinases: evolution of dynamic regulatory proteins.* Trends Biochem Sci, 2011. **36**(2): p. 65-77.
165. Johnson, L.N. and R.J. Lewis, *Structural Basis for Control by Phosphorylation.* Chemical Reviews, 2001. **101**(8): p. 2209-2242.
166. Taylor, S.S., et al., *Dynamics of signaling by PKA.* Biochim Biophys Acta, 2005. **1754**(1-2): p. 25-37.

167. McClendon, C.L., et al., *Dynamic architecture of a protein kinase.* Proceedings of the National Academy of Sciences, 2014. **111**(43): p. E4623-E4631.
168. Dell'Acqua, M.L. and J.D. Scott, *Protein kinase A anchoring.* J Biol Chem, 1997. **272**(20): p. 12881-4.
169. Fantozzi, D.A., et al., *Thermostable inhibitor of cAMP-dependent protein kinase enhances the rate of export of the kinase catalytic subunit from the nucleus.* J Biol Chem, 1994. **269**(4): p. 2676-86.
170. Wen, W., et al., *Identification of a signal for rapid export of proteins from the nucleus.* Cell, 1995. **82**(3): p. 463-73.
171. Wen, W., et al., *Heat-stable inhibitors of cAMP-dependent protein kinase carry a nuclear export signal.* J Biol Chem, 1994. **269**(51): p. 32214-20.
172. Wiley, J.C., et al., *Role of regulatory subunits and protein kinase inhibitor (PKI) in determining nuclear localization and activity of the catalytic subunit of protein kinase A.* J Biol Chem, 1999. **274**(10): p. 6381-7.
173. Hauer, J.A., et al., *Two well-defined motifs in the cAMP-dependent protein kinase inhibitor (PKIalpha) correlate with inhibitory and nuclear export function.* Protein Sci, 1999. **8**(3): p. 545-53.
174. Wen, W., S.S. Taylor, and J.L. Meinkoth, *The expression and intracellular distribution of the heat-stable protein kinase inhibitor is cell cycle regulated.* J Biol Chem, 1995. **270**(5): p. 2041-6.
175. Bruystens, J.G., et al., *PKA RIalpha homodimer structure reveals an intermolecular interface with implications for cooperative cAMP binding and Carney complex disease.* Structure, 2014. **22**(1): p. 59-69.
176. Wu, J., et al., *PKA type IIalpha holoenzyme reveals a combinatorial strategy for isoform diversity.* Science, 2007. **318**(5848): p. 274-9.
177. Kim, C., et al., *PKA-I holoenzyme structure reveals a mechanism for cAMP-dependent activation.* Cell, 2007. **130**(6): p. 1032-43.
178. Dalton, G.D. and W.L. Dewey, *Protein kinase inhibitor peptide (PKI): A family of endogenous neuropeptides that modulate neuronal cAMP-dependent protein kinase function.* Neuropeptides, 2006. **40**(1): p. 23-34.
179. Zheng, J.H., et al., *Crystallization of catalytic subunit of adenosine cyclic monophosphate-dependent protein kinase.* Methods Enzymol, 1991. **200**: p. 508-21.

180. Knighton, D.R., et al., *Crystal structure of the catalytic subunit of cyclic adenosine monophosphate-dependent protein kinase.* Science, 1991. **253**(5018): p. 407-14.
181. Walsh, D.A. and C.D. Ashby, *Protein kinases: aspects of their regulation and diversity.* Recent Prog Horm Res, 1973. **29**: p. 329-59.
182. Whitehouse, S., et al., *Studies on the kinetic mechanism of the catalytic subunit of the cAMP-dependent protein kinase.* Journal of Biological Chemistry, 1983. **258**(6): p. 3693-3701.
183. Whitehouse, S. and D.A. Walsh, *Purification of a physiological form of the inhibitor protein of the cAMP-dependent protein kinase.* J Biol Chem, 1982. **257**(11): p. 6028-32.
184. Eliezer, D., *Characterizing residual structure in disordered protein States using nuclear magnetic resonance.* Methods Mol Biol, 2007. **350**: p. 49-67.
185. Gonzalez, C.G., *Activation characteristics of phosphorylase kinase.* MS thesis, University of Washington, Seattle, WA, 1962.
186. Posner, J.B., et al., *The Assay of Adenosine-3',5'-phosphate in Skeletal Muscle*.* Biochemistry, 1964. **3**(8): p. 1040-1044.
187. Posner, J.B., R. Stern, and E.G. Krebs, *Effects of Electrical Stimulation and Epinephrine on Muscle Phosphorylase, Phosphorylase B Kinase, and Adenosine 3',5'-Phosphate.* J Biol Chem, 1965. **240**: p. 982-5.
188. Masterson, L.R., et al., *Allosteric cooperativity in protein kinase A.* Proc Natl Acad Sci U S A, 2008. **105**(2): p. 506-11.
189. Studier, F.W., *Protein production by auto-induction in high density shaking cultures.* Protein Expr Purif, 2005. **41**(1): p. 207-34.
190. Hemmer, W., M. McGlone, and S.S. Taylor, *Recombinant strategies for rapid purification of catalytic subunits of cAMP-dependent protein kinase.* Anal Biochem, 1997. **245**(2): p. 115-22.
191. Yonemoto, W., et al., *Identification of phosphorylation sites in the recombinant catalytic subunit of cAMP-dependent protein kinase.* J Biol Chem, 1993. **268**(25): p. 18626-32.
192. Thomas, J., et al., *Expression in Escherichia coli and characterization of the heat-stable inhibitor of the cAMP-dependent protein kinase.* J Biol Chem, 1991. **266**(17): p. 10906-11.

193. Ikura, M., L.E. Kay, and A. Bax, *A novel approach for sequential assignment of 1H, 13C, and 15N spectra of proteins: heteronuclear triple-resonance three-dimensional NMR spectroscopy. Application to calmodulin.* Biochemistry, 1990. **29**(19): p. 4659-67.

194. Kay, L.E., et al., *Three-dimensional triple-resonance NMR Spectroscopy of isotopically enriched proteins. 1990.* J Magn Reson, 2011. **213**(2): p. 423-41.

195. Grzesiek, S. and A. Bax, *An efficient experiment for sequential backbone assignment of medium-sized isotopically enriched proteins.* Journal of Magnetic Resonance (1969), 1992. **99**(1): p. 201-207.

196. Yang, D. and L.E. Kay, *Improved 1HN-detected triple resonance TROSY-based experiments.* J Biomol NMR, 1999. **13**(1): p. 3-10.

197. Marion, D., et al., *Overcoming the overlap problem in the assignment of 1H NMR spectra of larger proteins by use of three-dimensional heteronuclear 1H-15N Hartmann-Hahn-multiple quantum coherence and nuclear Overhauser-multiple quantum coherence spectroscopy: application to interleukin 1 beta.* Biochemistry, 1989. **28**(15): p. 6150-6.

198. Cavanagh, J.P., et al., *Incidence of parathyroid tissue in level VI neck dissection.* J Otolaryngol Head Neck Surg, 2011. **40**(1): p. 27-33.

199. Salzmann, M., et al., *TROSY in triple-resonance experiments: New perspectives for sequential NMR assignment of large proteins.* Proceedings of the National Academy of Sciences, 1998. **95**(23): p. 13585-13590.

200. Salzmann, M., et al., *TROSY-type Triple-Resonance Experiments for Sequential NMR Assignments of Large Proteins.* Journal of the American Chemical Society, 1999. **121**(4): p. 844-848.

201. Schulte-Herbrüggen, T. and O.W. Sørensen, *Clean TROSY: Compensation for Relaxation-Induced Artifacts.* Journal of Magnetic Resonance, 2000. **144**(1): p. 123-128.

202. Schwarzinger, S., et al., *Random coil chemical shifts in acidic 8 M urea: implementation of random coil shift data in NMRView.* J Biomol NMR, 2000. **18**(1): p. 43-8.

203. Schwarzinger, S., et al., *Sequence-dependent correction of random coil NMR chemical shifts.* J Am Chem Soc, 2001. **123**(13): p. 2970-8.

204. Williamson, M.P., *Using chemical shift perturbation to characterise ligand binding.* Progress in Nuclear Magnetic Resonance Spectroscopy, 2013. **73**: p. 1-16.

205. Farrow, N.A., et al., *Backbone dynamics of a free and phosphopeptide-complexed Src homology 2 domain studied by 15N NMR relaxation.* Biochemistry, 1994. **33**(19): p. 5984-6003.

206. Iwahara, J., C. Tang, and G. Marius Clore, *Practical aspects of (1)H transverse paramagnetic relaxation enhancement measurements on macromolecules.* J Magn Reson, 2007. **184**(2): p. 185-95.

207. Dyson, H.J. and P.E. Wright, *Nuclear magnetic resonance methods for elucidation of structure and dynamics of disordered states.* Methods Enzymol., 2001. **339**: p. 258-270.

208. Hauer, J.A., S.S. Taylor, and D.A. Johnson, *Binding-dependent disorder-order transition in PKI alpha: a fluorescence anisotropy study.* Biochemistry, 1999. **38**(21): p. 6774-80.

209. Clore, G.M., C. Tang, and J. Iwahara, *Elucidating transient macromolecular interactions using paramagnetic relaxation enhancement.* Curr Opin Struct Biol, 2007. **17**(5): p. 603-16.

210. Iwahara, J., Y.S. Jung, and G.M. Clore, *Heteronuclear NMR spectroscopy for lysine NH(3) groups in proteins: unique effect of water exchange on (15)N transverse relaxation.* J Am Chem Soc, 2007. **129**(10): p. 2971-80.

211. Iwahara, J., C.D. Schwieters, and G.M. Clore, *Ensemble approach for NMR structure refinement against (1)H paramagnetic relaxation enhancement data arising from a flexible paramagnetic group attached to a macromolecule.* J Am Chem Soc, 2004. **126**(18): p. 5879-96.

212. Clore, G.M. and J. Iwahara, *Theory, practice, and applications of paramagnetic relaxation enhancement for the characterization of transient low-population states of biological macromolecules and their complexes.* Chem Rev, 2009. **109**(9): p. 4108-39.

213. Demaille, J.G., K.A. Peters, and E.H. Fischer, *Isolation and properties of the rabbit skeletal muscle protein inhibitor of adenosine 3',5'-monophosphate dependent protein kinases.* Biochemistry, 1977. **16**(14): p. 3080-6.

214. Walsh, D.A., et al., *Peptides and protein phosphorylation.* CRC Press, 1990.

215. Walsh, D.A., et al., *Catlysis of the phosphrylaseinase actition reaction.* J Biol Chem, 1971. **246**(7): p. 1968-76.

216. Ashby, C.D. and D.A. Walsh, *Characterization of the interaction of a protein inhibitor with adenosine 3',5'-monophosphate-dependent protein kinases. I. Interaction with the catalytic subunit of the protein kinase.* J Biol Chem, 1972. **247**(20): p. 6637-42.

217. Cheng, H.C., et al., *A potent synthetic peptide inhibitor of the cAMP-dependent protein kinase.* J Biol Chem, 1986. **261**(3): p. 989-92.

218. Cheng, H.C., et al., *An active twenty-amino-acid-residue peptide derived from the inhibitor protein of the cyclic AMP-dependent protein kinase.* Biochem J, 1985. **231**(3): p. 655-61.

219. Cavanagh, J., et al., *Protein NRM Spectroscopy.* Academic Press, 2007. **Second Edition**.

220. Guttler, T., et al., *NES consensus redefined by structures of PKI-type and Rev-type nuclear export signals bound to CRM1.* Nat Struct Mol Biol, 2010. **17**(11): p. 1367-1376.

221. Knighton, D.R., *Structure of a peptide inhibitor bound to the catalytic subunit of cyclic adenosine monophosphate-dependent protein kinase.* Science, 1991. **253**: p. 414-420.

222. Bloch, F., *Nuclear Induction.* Physical Review, 1946. **70**(7-8): p. 460-474.

223. Purcell, E.M., H.C. Torrey, and R.V. Pound, *Resonance Absorption by Nuclear Magnetic Moments in a Solid.* Physical Review, 1946. **69**(1-2): p. 37-38.

224. Bartholdi, E. and R.R. Ernst, *Fourier spectroscopy and the causality principle.* Journal of Magnetic Resonance (1969), 1973. **11**(1): p. 9-19.

225. Ernst, R.R. and W.A. Anderson, *Application of Fourier Transform Spectroscopy to Magnetic Resonance.* Review of Scientific Instruments, 1966. **37**(1): p. 93-102.

226. Marion, D., M. Zasloff, and A. Bax, *A two-dimensional NMR study of the antimicrobial peptide magainin 2.* FEBS Lett, 1988. **227**(1): p. 21-6.

227. Hauge, H.H., et al., *Membrane-mimicking entities induce structuring of the two-peptide bacteriocins plantaricin E/F and plantaricin J/K.* J Bacteriol, 1999. **181**(3): p. 740-7.

228. Verly, R.M., et al., *Structure and Membrane Interactions of the Antibiotic Peptide Dermadistinctin K by Multidimensional Solution and Oriented (15)N and (31)P Solid-State NMR Spectroscopy.* Biophysical Journal, 2009. **96**(6): p. 2194-2203.

229. Luo, P. and R.L. Baldwin, *Mechanism of helix induction by trifluoroethanol: a framework for extrapolating the helix-forming properties of peptides from trifluoroethanol/water mixtures back to water.* Biochemistry, 1997. **36**(27): p. 8413-21.

230. Prosser, R.S., et al., *Current applications of bicelles in NMR studies of membrane-associated amphiphiles and proteins.* Biochemistry, 2006. **45**(28): p. 8453-65.
231. Warschawski, D.E., et al., *Choosing membrane mimetics for NMR structural studies of transmembrane proteins.* Biochim Biophys Acta, 2011. **1808**(8): p. 1957-74.
232. Poget, S.F., S.M. Cahill, and M.E. Girvin, *Isotropic bicelles stabilize the functional form of a small multidrug-resistance pump for NMR structural studies.* J Am Chem Soc, 2007. **129**(9): p. 2432-3.
233. Sanders, C.R., 2nd and G.C. Landis, *Reconstitution of membrane proteins into lipid-rich bilayered mixed micelles for NMR studies.* Biochemistry, 1995. **34**(12): p. 4030-40.
234. Sanders, C.R. and R.S. Prosser, *Bicelles: a model membrane system for all seasons?* Structure, 1998. **6**(10): p. 1227-34.
235. Dittmer, J., et al., *Incorporation of antimicrobial peptides into membranes: a combined liquid-state NMR and molecular dynamics study of alamethicin in DMPC/DHPC bicelles.* J Phys Chem B, 2009. **113**(19): p. 6928-37.
236. Aue, W.P., E. Bartholdi, and R.R. Ernst, *Two-dimensional spectroscopy. Application to nuclear magnetic resonance.* The Journal of Chemical Physics, 1976. **64**(5): p. 2229-2246.
237. Aue, W.P., E. Bartholdi, and R.R. Ernst, *2-Dimensional Spectroscopy - Application to Nuclear Magnetic-Resonance.* Journal of Chemical Physics, 1976. **64**(5): p. 2229-2246.
238. Jeener, J., *Ampere Summer School, Basko Polje, Yugoslavia*. 1971.
239. Kumar, A., et al., *Studies of J-connectives and selective 1H-1H Overhauser effects in H2O solutions of biological macromolecules by two-dimensional NMR experiments.* Biochem Biophys Res Commun, 1980. **96**(3): p. 1156-63.
240. Karplus, M., *Contact Electron-Spin Coupling of Nuclear Magnetic Moments.* The Journal of Chemical Physics, 1959. **30**(1): p. 11-15.
241. Jiang, Y., H. Wang, and J.T. Kindt, *Atomistic Simulations of Bicelle Mixtures.* Biophysical Journal, 2010. **98**(12): p. 2895-2903.
242. van Dam, L., G. Karlsson, and K. Edwards, *Morphology of magnetically aligning DMPC/DHPC aggregates-perforated sheets, not disks.* Langmuir, 2006. **22**(7): p. 3280-5.
243. Bechinger, B., *Detergent-like properties of magainin antibiotic peptides: a 31P solid-state NMR spectroscopy study.* Biochim Biophys Acta, 2005. **1712**(1): p. 101-8.

244. Porcelli, F., et al., *On the Role of NMR Spectroscopy for Characterization of Antimicrobial Peptides*, in *Membrane Proteins: Folding, Association, and Design*, G. Ghirlanda and A. Senes, Editors. 2013, Humana Press: Totowa, NJ. p. 159-180.
245. Valentine, K.G., et al., *Structure and topology of a peptide segment of the 6th transmembrane domain of the Saccharomyces cerevisae alpha-factor receptor in phospholipid bilayers.* Biopolymers, 2001. **59**(4): p. 243-56.
246. Gopinath, T., K.R. Mote, and G. Veglia, *Sensitivity and resolution enhancement of oriented solid-state NMR: Application to membrane proteins.* Progress in Nuclear Magnetic Resonance Spectroscopy, 2013. **75**: p. 50-68.
247. Wu, C.H., A. Ramamoorthy, and S.J. Opella, *High-Resolution Heteronuclear Dipolar Solid-State NMR Spectroscopy.* Journal of Magnetic Resonance, Series A, 1994. **109**(2): p. 270-272.
248. Oldfield, C.J., et al., *Comparing and combining predictors of mostly disordered proteins.* Biochemistry, 2005. **44**(6): p. 1989-2000.
249. Tompa, P., Z. Dosztanyi, and I. Simon, *Prevalent structural disorder in E. coli and S. cerevisiae proteomes.* J Proteome Res, 2006. **5**(8): p. 1996-2000.
250. Dunker, A.K., et al., *Function and structure of inherently disordered proteins.* Curr Opin Struct Biol, 2008. **18**(6): p. 756-64.
251. Sugase, K., H.J. Dyson, and P.E. Wright, *Mechanism of coupled folding and binding of an intrinsically disordered protein.* Nature, 2007. **447**(7147): p. 1021-5.
252. Wishart, D.S. and B.D. Sykes, *The 13C Chemical-Shift Index: A simple method for the identification of protein secondary structure using 13C chemical-shift data.* Journal of Biomolecular NMR, 1994. **4**(2): p. 171-180.
253. Neudecker, P., P. Lundstrom, and L.E. Kay, *Relaxation dispersion NMR spectroscopy as a tool for detailed studies of protein folding.* Biophys J, 2009. **96**(6): p. 2045-54.
254. Kay, L.E., *NMR studies of protein structure and dynamics. 2005.* J Magn Reson, 2011. **213**(2): p. 477-91.
255. Saupe, A. and G. Englert, *High-Resolution Nuclear Magnetic Resonance Spectra of Orientated Molecules.* Physical Review Letters, 1963. **11**(10): p. 462-464.
256. Brunner, E., *Residual dipolar couplings in protein NMR.* Concepts in Magnetic Resonance, 2001. **13**(4): p. 238-259.

257. Dedmon, M.M., et al., *Heat shock protein 70 inhibits alpha-synuclein fibril formation via preferential binding to prefibrillar species.* J Biol Chem, 2005. **280**(15): p. 14733-40.

258. Bertoncini, C.W., et al., *Release of long-range tertiary interactions potentiates aggregation of natively unstructured alpha-synuclein.* Proc Natl Acad Sci U S A, 2005. **102**(5): p. 1430-5.

259. Vise, P., et al., *Identifying long-range structure in the intrinsically unstructured transactivation domain of p53.* Proteins, 2007. **67**(3): p. 526-30.

260. Salmon, L., et al., *NMR Characterization of Long-Range Order in Intrinsically Disordered Proteins.* Journal of the American Chemical Society, 2010. **132**(24): p. 8407-8418.